Coronin 1C Restricts Endosomal Branched Actin to Organize ER Contact and Endosome Fission

by

Jonathan. F. Striepen

B.S., Georgia Institute of Technology, 2016

A thesis submitted to the

Faculty of the Graduate School of the

University of Colorado in partial fulfillment

of the requirements for the degree of

Doctor of Philosophy

Department of Molecular Cellular and Developmental Biology

2022

Committee Members:

Gia Voeltz, Chair

Prof. Greg Odorizzi

Prof. Min Han

Prof. Amy Palmer

Prof. Michael Stowell

Striepen, Jonathan. F. (Ph.D., Molecular Cellular and Developmental Biology)

Coronin 1C Restricts Endosomal Branched Actin to Organize ER Contact and Endosome Fission

Thesis directed by Prof. Gia Voeltz

ER contact sites define the position of endosome bud fission during actin-dependent cargo sorting. Disrupting endosomal actin structures prevents retrograde cargo movement; however, how actin affects ER contact site formation and endosome fission is not known. Here I show that in contrast with the WASH complex, actin, its nucleator ARP2/3, and COR1C form a contained structure at the bud neck that defines the site of bud fission. I find that actin confinement is facilitated by Type I coronins. Depletion of Type I coronins, allows actin to extend along the length of the bud in an ARP2/3 dependent manner. I demonstrate that extension of branched actin prevents ER recruitment and stalls buds prior to fission. Finally, my structure-function studies show that the COR1C's coiled-coil domain is sufficient to restore actin confinement, ER recruitment, and endosome fission. Together my data reveal how the dynamics of endosomal actin and activity of actin regulators organize ER-associated bud fission.

Dedication

To everyone that helped me believe when I wasn't sure, your faith in my capabilities taught me to have trust in myself. Know that the confidence you helped me find was likely worth more than all of the technical knowledge that I worked so hard to gain. I will always be grateful.

Acknowledgements

I want to thank Gia for her all of support and guidance. She gave me the freedom to pursue my own scientific vision. The experiences I had in her lab helped me build confidence in my own abilities as a scientist. She always had the ability to cut through to the heart of scientific questions and I hope to emulate that in my career. I would like to thank my committee; Greg, Min, Amy, and Michael. Your scientific guidance was key for my success. I want to thank my lab mates in particular Tricia, Eric, Sofia, and Emi for your scientific insight and emotional support. Woking with such brilliant and hard working scientists was a daily inspiration and I count myself lucky to have done research along side you. During the times when I wasn't sure I belonged having the support of such clever and thoughtful people gave me the confidence to continue. I also want to thank Val my steadfast undergraduate student. You were a hardworking smart understudy and I know you will find success in grad school. Finally, I want to thank all of the support staff and building maintenance people of the department. Your work is so integral to the departments function that we forget to acknowledge it because we couldn't imagine our lives with out it.

Contents

Chapter

Tables

Table

Figures

Figure

Chapter 1

Introduction

1.1 The endocytic system and its interplay with the ER and cytoskeleton

Defining an intracellular space that is distinct from the extracellular environment is a fundamental characteristic of all life. Maintaining a discrete intracellular space relies on the selective import of extracellular material such as nutrients and signaling molecules, enabling cellular growth and adjustment to changing extracellular conditions. A principle component of cellular import is endocytosis, a process where the plasma membrane (PM) is invaginated and pinched off capturing material bound to the cellular surface via receptors in intracellular endocytic vesicles. Endocytosis is the beginning of endocytic pathway which ends in proteolytic compartments called lysosomes where cargos are broken down into essential building blocks which the cell can repurpose.

The endocytic system consists of many independently trafficking vesicles called endosomes which facilitate cargo flow from PM to lysosomes. Endosomes are formed when endocytic vesicles undergo homotypic fusion to form early endosomes (EE), funneling cargo into the endocytic system. As EEs traffic further inward along microtubules they mature to form late endosomes (LE), growing larger by more homotypic fusion, acidifying their lumens via proton pumps, and adjusting their lipid compositions to facilitate recruitment of new maturation factors. This means that when LEs ultimately fuse with lysosomes, delivering their cargos, they already have many lysosomal characteristics, maintaining the integrity of these proteolytic compartments.

Along this maturation pathway the endocytic system periodically rescues cargo from degradation via recycling. This is a process where endosomes sort and concentrate proteins selected to avoid lysosomal degradation into elongated bud structures and then undergo fission. This allows for return of cargos to origin membranes. This a EEs recycling primarily to the plasma membrane while LEs recycle primarily to the Golgi Simonetti et al. [2017], Gallon and Cullen [2015], Cullen and Steinberg [2018]. These recycling pathways are essential to preserve the entrance (endocytosis) and exit (degradation) of the endocytic pathway. Without efficient return of cargo receptors and membrane the cell would be unable to support the substantial amount of endocytosis required for homeostasis Hao and Maxfield [2000]. In a similar vein, without rescue of cargo receptors from late endosomes the cell would be unable to maintain the proteolytic capacity of lysosomes Riederer et al. [1994].

A classic example of the utility of this process is the retrograde recycling of the cation independent mannose six phosphate receptor (CI-M6PR) Sandoval and Bakke [1994], Cullen and Korswagen [2012], Simonetti et al. [2017], Gallon and Cullen [2015]. The CI-M6PR binds cargos such as acid hydrolases produced in the Golgi and destined for the lysosome. Upon fusion with the target late endosome the relatively low pH causes the CI-M6PR to disengage with its cargo. The late endosome then returns the CI-M6PR to the Golgi via this budding and fission process avoiding degradation in the lysosome and allowing the CI-M6PR to engage another round of cargo.

Endosomal function and maturation is facilitated by a family of small GTPases called Rabs. When Rabs are in their active GTP bound state they extend a small amphipathic helix allowing them to bind to the endosomal membrane Langemeyer et al. [2018]. Rab binding defines the maturation state of the compartment by recruiting all the machineries responsible for the unique characteristics and functions of each stage. Rabs facilitate a unidirectional flow of cargo towards the lysosome by exchanging with one another in a predefined order driven by the activating guanine nucleotide exchange factors (GEFs) and deactivating GTPase activating proteins (GAPs). Each Rab is recruited to the endosomal

membrane by its GEF and then removed at the appropriate maturation state by its GAP Langemeyer et al. [2018]. For example the machineries that Rab4 (an early endosome Rab) recruits drive changes which recruit the GEF for Rab5 and the GAP for Rab4. This means that intrinsic to the phenotypic changes that each Rab drives is the recruitment of the next Rab allowing for a timely procession along the maturation pathway towards the lysosome.

These fundamental endosomal processes of trafficking, maturation, recycling, and degradation are reliant on the cytoskeleton most notably microtubules and actin to function Neefjes et al. [2017]. Endosomal interaction with these cytoskeletal constituents is regulated by membrane contact sites (MCSs) with the endoplasmic reticulum (ER). Here I will highlight the interplay of the endocytic system, the ER, and the cytoskeleton 1.1. Although we have decoded enough of this tripartite crosstalk to appreciate its importance, we do not fully comprehend many of the intricacies of the communications happening and there are large gaps in our understanding that remain unaddressed.

1.2 Microtubule motor loading at late endosome ER membrane contact sites.

The principle role of the endocytic system is transport. As such, endosomal movement is paramount. Each endosomes make up varies from the next depending on maturation state and endocytosed cargos. This means that in order for cargos to be delivered to the appropriate destination in a timely fashion each endosome most move depending on its unique contents and make up. To accommodate this there are ER and endosomal machineries which collaborate at MCSs to sense the endosomal composition, integrate that with broader cell signaling cues, and load the appropriate motor onto the endosome to facilitate either plus or minus end transport on microtubules. Increasingly these machineries have been couched with in broader cellular functions and signaling pathways linking them with disease. Additionally, their significance has been highlighted in cell types other than standard tissue culture models driving home the importance of ER regulated endosomal trafficking on microtubules.

The interplay of the three contingents is understood more completely in the LE/lysosomal compartment. Integral to maturation is the relative position of the endosome in the cell and ER MCSs Wu and Voeltz [2021], Friedman et al. [2013]. As endosomes mature they form more and more persistent MCSs with the ER to the point that LEs are almost always found associated with the ER Friedman et al. [2013]. Movement into the perinuclear cloud (PNC) is driven by dynein motors which bind p150 glued and RILP on LEs Johansson et al. [2007], Zajac et al. [2013]. These adaptors are recruited to the LE via the small GTPase Rab7. This interaction is regulated by a MCS formed between the ER localized vesicle associated protein A (VAPA) and the endosome localized cholesterol sensing protein ORP1L Rocha et al. [2009]. When LEs and lysosomes are high in cholesterol ORP1L adopts a closed confirmation leaving the endosome to traffic via dynein motors and accumulate in the PNC. However, if endosomal cholesterol levels fall ORP1L binds VAPA disrupting RILP p150 glued association with dynein biasing the endosome to move away from the PNC Rocha et al. [2009]. The interplay here is further complicated by Annexin A1 an ER resident protein which uses the MCS formed by ORP1L and VAPA to move cholesterol into the LE/lysosomal membrane from the ER Eden et al. [2016]. The net result is that there is a rough gradient of endosomal characteristics moving outward from the PNC. Endosomes in periphery are less mature, low in cholesterol, and do not associate as frequently with the ER, while endosomes in the PNC are more mature, cholesterol replete, and almost always in contact with the ER Johansson et al. [2007], Eden et al. [2016], Rocha et al. [2009], Friedman et al. [2013]. While these data demonstrate the interrelatedness of endosomal composition, position, ER contact, and microtubule trafficking it is still unclear which of these is upstream of the others. It is possible that rather than a specific order of recruitment these processes represent a series of levers by which the cell can regulate flow of lipids and cargos through the endocytic system.

Retention of LEs/lysosomes in the PNC is not only driven by microtubule trafficking. The ER localized ubiquitylation complex UBE2J1/RNF26 acts to confine maturing endosomes to the PNC at MCSs Jongsma et al. [2016], Cremer et al. [2021]. This complex

ubiquitylates SQSTM1 which binds an unknown endosomal adaptor preventing trafficking away from the PNC. Maintaining the PNC is critical for efficient termination of activated signaling factors such as EGFR Cremer et al. [2021]. Interestingly, UBE2J1/RNF26 ubiquitylate a different residue on SQSTM1 (K435) then the one previously demonstrated to be important for LC3 interaction (K420) and autophagic cargo sequestration. This work highlights the importance of endosomal position as regulated by the ER. It also demonstrates another way that endosomal position is integrated into broader cell signaling pathways.

Although we have just extensively discussed how important maintaining the LE/lysosome PNC is for the cells proteolytic capacity, + end directed trafficking of LEs towards the PM is necessary for specialized cellular functions such as the formation of cellular protrusions. In this case the ER resident protein Protrudin interacts with Rab7 and phosphatidylinositol 3-phosphate (PI3P) in the late endosomal/lysosomal membrane forming a MCS Raiborg et al. [2015b]. This contact site aids in the loading of kinesin-I motors onto the motor adaptor FYCO1 driving endosomes towards the PM Raiborg et al. [2015b]. Movement of LEs into the periphery and their eventual fusion with the PM is critical for neurite outgrowth where the LEs provide additional lipids for the formation of these protrusions Raiborg et al. [2015b], Gao et al. [2021]. Protrudin was originally identified in this context when it was linked with hereditary spastic paraplegia (HSP) a disease characterized by axonal degeneration Shirane and Nakayama [2006]. More recently Protrudin driven movement has also been linked to a different protrusion, the invadopodium of metastatic cancers Pedersen et al. [2020]. In this case Protrudin driven LE movement towards the PM provides not only lipids for formation of the invadopodium but also delivers the matrix metalloproteinase MT1-MMP to the cell surface where it helps break down collagen based tissue barriers hypothetically increasing a cancer cell's metastatic potential Pedersen et al. [2020]. This makes pathways involved in Protrudin activation of interest for therapeutic manipulation.

1.3 Microtubule motor loading at early endosome ER membrane contact sites.

EE MCSs with the ER as well as their movement on microtubules are understood with much less granularity. In part this may be due to their small size and increased activity relative to LEs making them more difficult to study by microscopy. EEs also form less frequent MCSs with the ER implying that they are less reliant on MCSs for movement along microtubules Friedman et al. [2013]. However, EE MCSs with the ER are still frequent and given that they are more motile and represent the entry into the endocytic system it seems unlikely that the ER is not regulating at least a subpopulation of EE trafficking. The first step in characterizing EE ER MCS would be identifying the factors tethering the two membranes together. However, filling this gap is made harder due to the comparably poor characterization of the EE dynein adaptors, which is surprising given that a majority of EE motion is – end directed and thus dynein dependent Zajac et al. [2013]. Recent work implicates the Rab5 effector Fused Toes (FTS)–Hook–FTS and Hook-interacting protein (FHIP) (FHF) complex in recruiting dynein motors to the EE membrane but the precise constituents and order of recruitment remain uncharacterized Guo et al. [2016], Christensen et al. [2021]. Following up this work will be an important step in identifying tethering proteins which form the EE ER MCS.

1.4 ER facilitated maturation occurs at microtubule crossings with ER and endosome membrane contact sites.

Although our understanding of EE MCSs with the ER is still lacking we are starting to elucidate how the ER regulates the transition from a mature EE to LE. Recent work identified reticulon 3 (RTN3) a non-membrane shaping member of the reticulon family of proteins which interacts with Rab9 to form a MCS Wu and Voeltz [2021]. This MCS is critical for the appropriate exchange of Rabs on the endosomal membrane during maturation.

Removing either side of the tether results in endosomes positive for both EE (Rab5) and LE (Rab7) markers, leading to not only reduced cargo recycling from the late endosome, but also a reduced proteolytic capacity of the lysosomal compartment Wu and Voeltz [2021]. These results are made all the more interesting by the observation that the RTN3 Rab9 contacts occur concomitantly with microtubules again highlighting the importance of the tripartite interaction between ER, endosome, and cytoskeleton. The precise mechanism of ER driven maturation and the relevance of microtubules for the MCS formation remain unclear.

1.5 Actin polymerization at endosome ER membrane contact sites.

The other major cytoskeletal element which has been concretely connected to endosomal function and ER regulation at MCSs is actin. Endosomal actin structures are predominantly found at points of cargo sorting and recycling as branched structures Duleh and Welch [2010], Gomez and Billadeau [2009], Derivery et al. [2009]. These structures are polymerized via activation of ARP2/3 complex by the WASH complex which in turn is recruited by interacting with sorting/recycling complexes such as retromer and retriever Duleh and Welch [2010], Derivery et al. [2009], Gomez and Billadeau [2009], McNally et al. [2017], Simonetti and Cullen [2019]. These branched actin structures are thought to stabilize the elongated membrane bud structures used to sequester recycling cargo Puthenveedu et al. [2010]. It has also been proposed that these actin structures are capable of providing a pushing/pinching force which aids in the fission of endosome buds as actin does at clathrin mediated endocytosis, however, this has never been demonstrated directly Derivery et al. [2009].

The ER forms MCSs with the endosome bud structures and regulates the fission process marking the points where the buds undergo fission Rowland et al. [2014]. The ER resident protein transmembrane containing coiled-coil protein 1 (TMCC1) is important for contact site formation and subsequent LE bud fission Hoyer et al. [2018]. Although, TMCC1's binding partner on the endosome remains elusive Coronin 1C (COR1C), an actin regulatory

factor, is an endosome localized player in MCS formation and function. In COR1C's absence the ER is not recruited as efficiently leading to a reduction in fission and therefore compromised retrograde cargo sorting of the CI-M6PR Hoyer et al. [2018]. My work detailed here demonstrates that COR1C and its Type I Coronin family members act to confine these branched actin structures to the LE bud neck defining the available membrane for ER recruitment and the subsequent fission event. In their absence actin polymerizes along the entire length of the LE bud preventing ER recruitment. This work represents an interesting new paradigm where actin polymerization directs the position of ER contact by preventing MCSs from forming in some areas. Surprisingly, these branched actin structures are stable throughout the fission process raising the interesting possibility that they mark a recycling domain on the endosome from which multiple rounds of cargo sorting and fission can occur.

The cross talk happening between endosome, ER, and actin if further complicated by another MCS at the endosome bud formed by interactions between ER residents VAPA/B and sorting nexin 2 Dong et al. [2016]. This contact site provides a platform for oxysterol-binding protein 1 to transfer PI4P From the endosomal membrane to the ER. Preventing this MCS formation by knocking out VAPA/B results in accumulation of PI4P in the endosomal membranes. This in turn leads to a dramatic, WASH dependent accumulation of actin on endosomal membranes preventing effective recycling from late endosomal compartments. Taken together with my work this suggests that ER recruitment both regulates and is regulated by actin polymerization. Perhaps upon recruitment to a forming endosome bud the ER actively alters the bud lipid composition to prevent an over accumulation of actin and maintain MCS integrity for fission regulation.

1.6 Myosin driven endosome trafficking on actin filaments, a potential novel ER membrane contact site.

Parts of the endocytic system require not only microtubule based movement but also actin based movement driven by myosin to traffic efficiently. This seems to be most common

for parts of the endocytic system that traffic in close proximity to the PM and therefore must navigate the dense cortical actin structures that exist there Hales et al. [2002], Wang et al. [2008]. The best characterized example is the trafficking of recycling endosomes (RE) on actin filaments driven by myosin Vb (MyoVb). In this case binding protein Rab11-family interacting protein 2 (Rab11-FIP2) is recruited to REs by its interaction with Rab11 and in turn recruits MyoVb Lapierre et al. [2001]. In the absence of this interaction Rab11 positive structures accumulate in the PNC and recycling of membrane receptors, such as immunoglobulin A receptor, to the PM are compromised Hales et al. [2002]. Interestingly, MyoVb has Ca2+ sensitive activity and Rab11-FIPs has a C2 domain which could infer Ca2+ sensitive binding Li et al. [2004], Giordano et al. [2013], Lees et al. [2017], Orci et al. [2009]. This fits nicely with later papers demonstrating the importance of MyoVb and recycling endosomes in long term potentiation (LTP) at the dendritic spines of neurons. Signal induction prompts Ca2+ influx leading to the recycling of AMPA receptors by REs. Recycling is driven by the Ca2+ sensitive MyoVb, thus promoting LTP Wang et al. [2008]. Given the dense actin structures present in dendritic spines a MyoVb dependent form of trafficking seems intuitive Basu and Lamprecht [2018]. The ER is the Ca2+ storage organelle of the cell and there are several Ca2+ sensitive MCS which form most notably at the PM Wu et al. [2018], Orci et al. [2009], Giordano et al. [2013], Lees et al. [2017]. Coupled with the prevalence of ER MCS at other motor loading events the formation of ER MCS with RE to drive MyoVb loading an intriguing possibility.

1.7 Overlap between actin polymerization and microtubule loading at endosome buds, a potential unexplored aspect of ER membrane contact sites.

Recent work uncovered a surprising overlap in the machinery required for dynein recruitment and actin polymerization. The Arp1/11 minifilament is a key constituent of the dynactin complex which is required for dynein recruitment. In this context the minifilament is capped with actin capping protein Schroer [2004]. Interestingly, FAM21 a component of

the WASH complex has cap binding domain which allows it to uncap the Arp1/11 minifilament enabling it to act as a primer for ARP2/3 actin nucleation Fokin et al. [2021]. Given that previous work has implicated dynein in providing a pulling force necessary for fission of the bud coordinating of these two cytoskeletal elements at endosomal sorting domains makes sense Wassmer et al. [2009], Soppina et al. [2009]. The ER forms MCS at endosome buds and regulates both dynein loading and actin polymerization making it plausible that ER could be involved as a fulcrum for the ARP1/11 minifilament allowing it to uncap polymerizing actin on the proximal side of the bud or remain capped recruiting dynein on the distal side thus promoting fission Dong et al. [2016], Rocha et al. [2009].

1.8 Endosome fusion a potential novel ER membrane contact site function.

Endosome fusion is essential for movement of cargos along the endocytic pathway into the lysosome. Endosomal fusion events are directed by the tethering complexes class C core vacuole/endosome tethering (CORVET) and homotypic fusion and vacuole protein sorting (HOPS). These complexes provide specificity and proximity for SNAP receptor (SNARE) protein assembly and subsequent fusion of EE (CORVET) and LE (HOPS) Van Der Kant et al. [2015], van der Beek et al. [2019], Balderhaar and Ungermann [2013]. Given that the endosome trafficking and fission are regulated by ER MCS it seems plausible that fusion might be similarly regulated. Recently, it was observed that mitochondrial fusion occurs at ER MCSs supporting the idea that MCS might provide a platform to support the fusion process Abrisch et al. [2020]. Additionally, assembly of the HOPS complex on LE membranes is dependent both on Rab7 and RILP both of which have been characterized at ER MCS used for microtubule motor loading Rocha et al. [2009], Lin et al. [2014]. This fits well with microscopy which shows that VPS41 a component of the HOPS complex overlaps strikingly with the ER. Visualization of endosome fusion in live cells has been a difficult technical hurdle to overcome but with the advent of photoconvertible fluorescent tags and advances in live cell light microscopy exploring this potentially novel MCS function is possible McEvoy

et al. [2012].

1.9 Actin at endosomal fission events, plenty of data but little clarity

The endosome fission process begins with cargo adaptor complexes such as the retromer and retriever. These complexes recognize different recycling cargos, concentrate the cargo, and recruit downstream factors essential for bud formation and fission McNally et al. [2017], Seaman et al. [1998], Harbour et al. [2012], Kvainickas et al. [2017a]. Cargo adaptors then bind the Wiskott Aldrich Syndrome protein and scar homologue (WASH) complex which subsequently binds and activates the branched actin nucleator actin related protein 2/3 (ARP2/3) Harbour et al. [2012], Simonetti and Cullen [2019]. In turn, ARP2/3 recruits branched F-actin to generate a branched actin structure on the endosome bud Gomez and Billadeau [2009], Kvainickas et al. [2017b]. This actin structure is proposed to use its membrane remodeling activities to facilitate bud formation and stabilization, cargo binding, and fission Derivery et al. [2009], Hong et al. [2015], Puthenveedu et al. [2010], Duleh and Welch [2010], Dong et al. [2016].

Although many and sometimes contradictory membrane remodeling functions are ascribed to actin at the endosome bud, actin dynamics during fission have not been measured directly. Instead, actin's function at the endosome bud has been studied by disruption of actin assembly and downstream measurements of either retrograde cargo flow or general endosome shape Duleh and Welch [2010], Rottner et al. [2010], Simonetti and Cullen [2019], Puthenveedu et al. [2010]. Current models of actin function at endosome fission rely on these endpoint assays and actin membrane remodeling activities characterized at other intracellular membranes Mayor and Köster [2016]. Without basic measurements of actin dynamics and regulation during fission its function during this essential step in cargo recycling remains obscure.

The endoplasmic reticulum (ER) has emerged as a principal regulator of the endocytic system through the formation of membrane contact sites (MCSs). Via MCSs, the ER is

able to regulate a variety of basic endosome functions and characteristics, including trafficking on microtubules, lipid composition, maturation, and fission Wu et al. [2018], Wu and Voeltz [2021], Rocha et al. [2009], Raiborg et al. [2015a], Wilhelm et al. [2017], Allison et al. [2017], Dong et al. [2016]. We previously identified two factors important for MCS formation and subsequent fission of late endosome buds marked by the WASH complex: the ER-localized protein transmembrane containing coiled-coil protein 1 (TMCC1) and the endosome-localized actin regulatory protein coronin 1C (COR1C) Hoyer et al. [2018].

COR1C and its homologs in the Type I coronin family, coronin 1A (COR1A) and coronin 1B (COR1B), are regulatory hubs of branched actin dynamics Chan et al. [2011]. COR1B and COR1C coimmunoprecipitate with ARP2/3 and the branched actin cleavage protein Cofilin Cai et al. [2005], Rosentreter et al. [2006]. In particular, COR1B ARP2/3 interaction was demonstrated to inhibit ARP2/3 activity Cai et al. [2007]. This regulatory axis between Type I coronins and ARP2/3 could be relevant to endosome cargo sorting and fission. ARP2/3 stabilization by Cortactin stabilizes endosome buds to allow slow diffusing cargos to accumulate in the bud Puthenveedu et al. [2010]. Although fission was not directly examined, these data suggest that bud-localized actin structures might slow or prevent fission and must be disassembled from the endosome bud for fission to occur. If actin clearance is required, it is unknown by what mechanism and to what extent actin would be rearranged. COR1C is a particularly attractive candidate for this function because it co-localizes with actin on endosome buds and, as mentioned before, is required for efficient fission of WASH complex-associated buds Hoyer et al. [2018], Puthenveedu et al. [2010].

Here I set out to capture a more complete view of branched F-actin dynamics at endosome budding domains and understand the function of COR1C on these structures during the entire endosome bud fission process. I demonstrate that actin is contained to the endosome bud neck by COR1C. Without COR1C and its homologs, actin begins to proliferate along the length of the endosome bud, disrupting ER MCSs and fission. I show this regulation is likely achieved by inhibition of ARP2/3 via COR1C's CC.

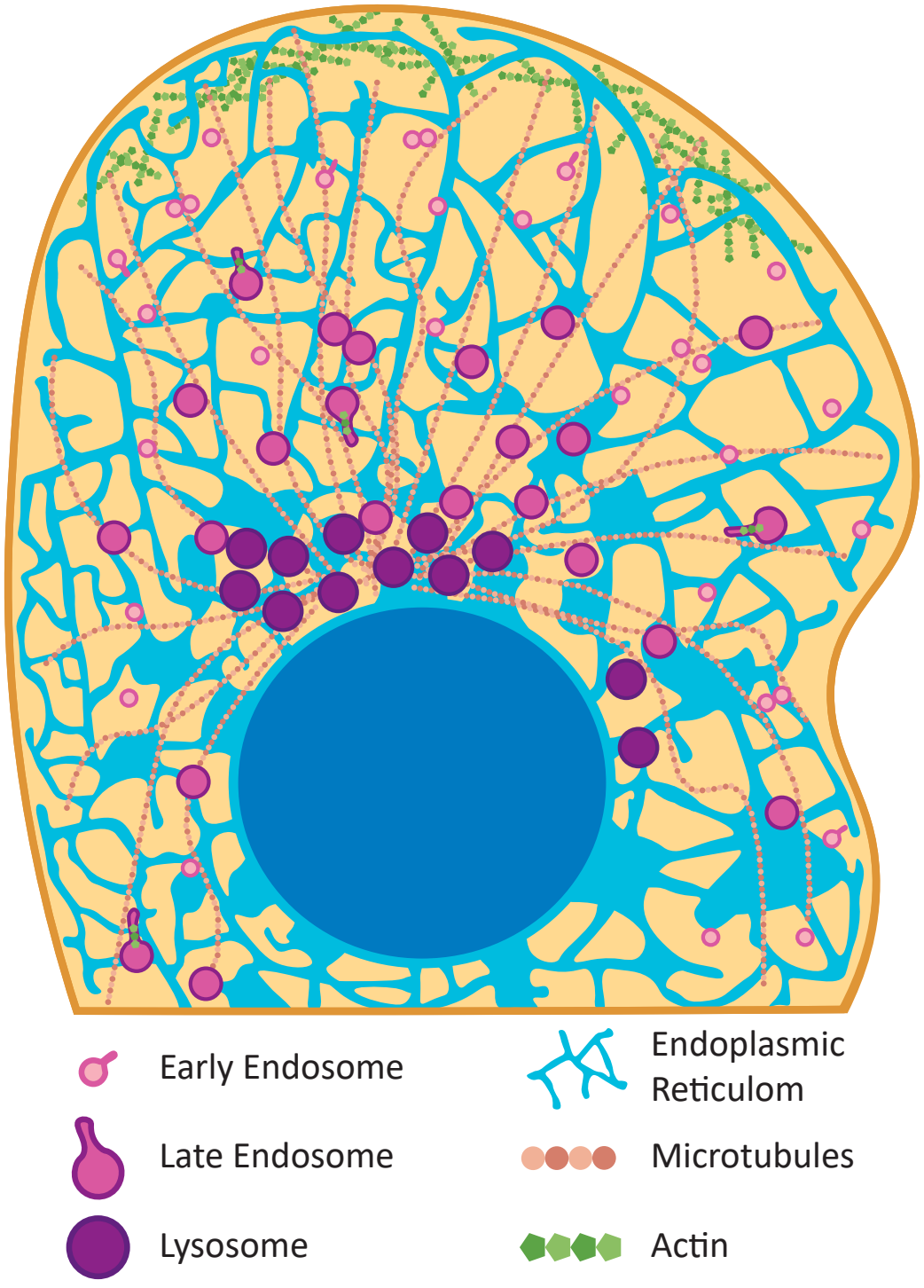

Figure 1.1: A schematic of the endocytic system and its interactions with ER and cytoskeleton.

Chapter 2

Dynamics of actin and actin regulatory factors during endosome fission.

2.1 Introduction

As a first step towards understanding the function of COR1C during bud fission, I characterized the dynamics and distribution of actin and actin regulatory components before, during and after endosome bud fission. I hypothesized that if the branched actin structures present at the endosome bud act to stall fission that they would need to be cleared in order for fission to occur. To do this thoroughly I examined the dynamics of multiple upstream regulators of endosomal actin including FAM21 a component of the WASH complex, ARP3 a component of the ARP2/3 complex, actin, and COR1C. Although, these complexes are well characterized with respect to their general function that function was not yet contextualized during the endosomal fission process.

2.2 Results

I co-transfected COS-7 cells with GFP-Rab7 (or mCh-Rab7, to label late endosomes (LEs)) and either mCh-FAM21 (a component of the WASH complex), ARP3-mEm (ARP2/3 Complex), COR1C-Halo, or α-actin-mNG (fluorescently tagged nanobody against actin). I visualized endosome bud fission by live time-lapse confocal fluorescence microscopy (two-minute movies, two sec intervals). Marker distribution was analyzed along the bud at three key reference points: in the pre-fission frame, the fission frame, and the post-fission frame 2.1, 2.2, 2.3, 2.4.

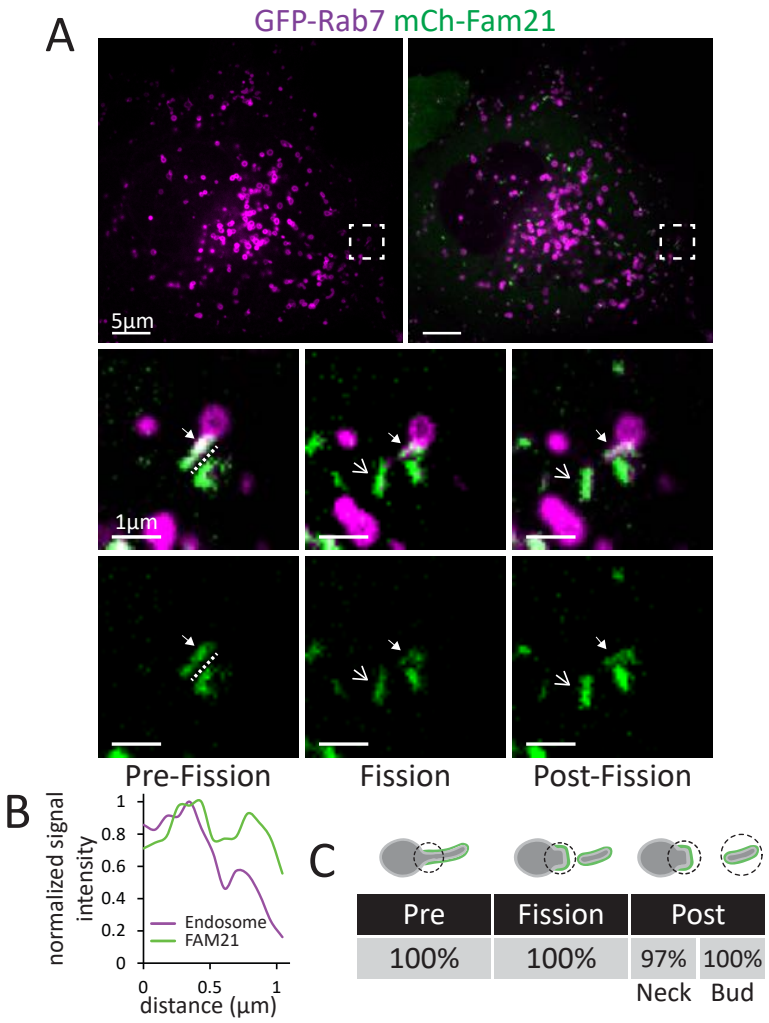

Figure 2.1: (A) Representative images of COS-7 cells transfected with GFP-Rab7 (LE, magenta) and mCh-FAM21 (WASH complex, green). Magnified inset (5 x 5 μm) below shows time lapse of a representative fission event. Note: FAM21 signal localizes along entire length of bud and signal is present on the post fission bud. Block arrowhead indicates the bud neck and line arrowhead indicates departing bud.
(B) Line scan analysis along the length of endosome bud in pre-fission frame from (A) shows FAM21 signal labels the length of the bud. Lines are shown in (A) adjacent to actual area measured so as not to obscure region of interest.
(C) Fission events as in (A) were scored for FAM21 enrichment at the bud neck in the pre-fission, fission, and post-fission frames. For post fission frames, both the bud neck and departed bud were scored for positive FAM21 signal. Table shows data as percentage of fission events with enrichment at each stage (n = 37 fission events in 16 cells, performed in triplicate). Model indicates where enrichment was assessed at each stage of fission. Scale bars for whole cell = 5 μm; insets = 1 μm.

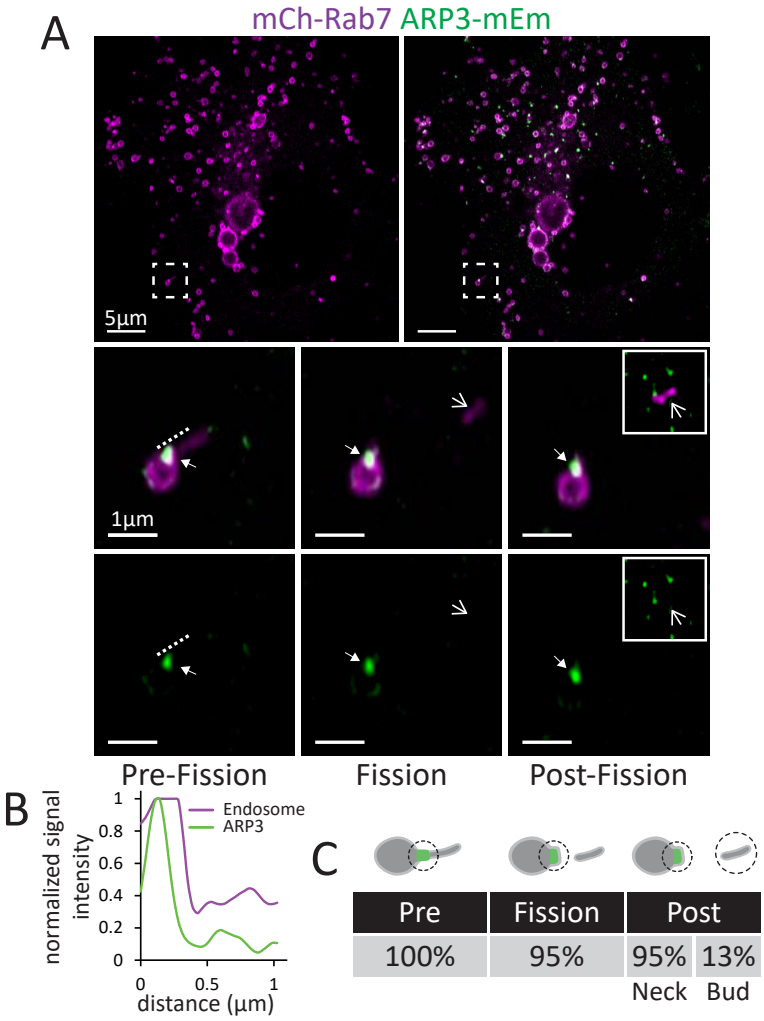

Figure 2.2: (A) Representative images of COS-7 cells transfected with mCh-Rab7 (LE, magenta) and ARP3-mEm (ARP2/3 Complex, green). Magnified inset (5 x 5 μm) below shows time lapse of a representative fission event. Secondary inset shows departed bud which moved out of primary inset. Block arrowhead indicates the bud neck and line arrowhead indicates departing bud.
(B) Line scan analysis along the length of endosome bud in pre-fission frame from (A) shows ARP3 signal labels the base of the bud. Lines are shown in (A) adjacent to actual area measured so as not to obscure region of interest.
(C) Fission events as in (A) were scored for ARP3 enrichment at the bud neck in the pre-fission, fission, and post-fission frames. For post fission frames, both the bud neck and departed bud were scored for positive ARP3 signal. Table shows data as percentage of fission events with enrichment at each stage. In F, n = 24 fission events in 11 cells, performed in triplicate. Scale bars for whole cell = 5 μm; insets = 1 μm.

These data revealed the relative distributions of these actin regulators and their general dynamics during bud fission. FAM21 (WASH) localized along the entire length of the bud in the pre-fission frame and was split between the endosome vacuole and the bud upon fission (Fig. 2.1 A and B). In stark contrast, the branched actin nucleator ARP3 (ARP2/3) and actin itself segregated to a small punctum at the base of the endosome bud before and during fission. Neither ARP3 nor actin signal left with the bud post fission (Fig. 2.2 2.3). This localization is demonstrated by comparing the line scan analyses along the vacuole and bud of the pre-fission frames; only the FAM21 signal enriches along the entire length of the line scan (compare Fig. 2.1 2.2 2.3 2.4). COR1C had the same distribution as ARP3 and actin before and after bud fission (Fig. 2.4). The data collected were tabulated as the percent of fission events that had signal at the base of the bud before, during, and after fission. Additionally, for events that had stable signal enrichment at the bud neck in the post fission, I measured the percent of events with signal enrichment leaving with the bud (Fig. 2.1 2.2 2.3 2.4). This revealed that FAM21 was the only signal consistently departing with the bud. Taken together, my results show that actin structures are maintained at the bud neck throughout the fission process and do not need to be cleared entirely for fission to occur. These data suggest that fission occurs distal to actin and in an actin-free zone because the signal for actin, ARP2/3, and COR1C segregate on the vacuolar side of the fission site and are rarely found in association with the leaving bud (see summary diagram in Fig. 2.5).

2.3 Discussion

My examination of the dynamics of actin and actin regulatory factors revealed that the actin structure is stable during the fission process. This was surprising given that previous works suggested that endosomal actin slows the fission process in order for cargo to be sorted effectively Puthenveedu et al. [2010]. I can not rule out that there are actin rearrangements occurring at scale or speed that I am not able to measure due to current limitations of light microscopy however, my data due demonstrate that a large portion of the structure remains

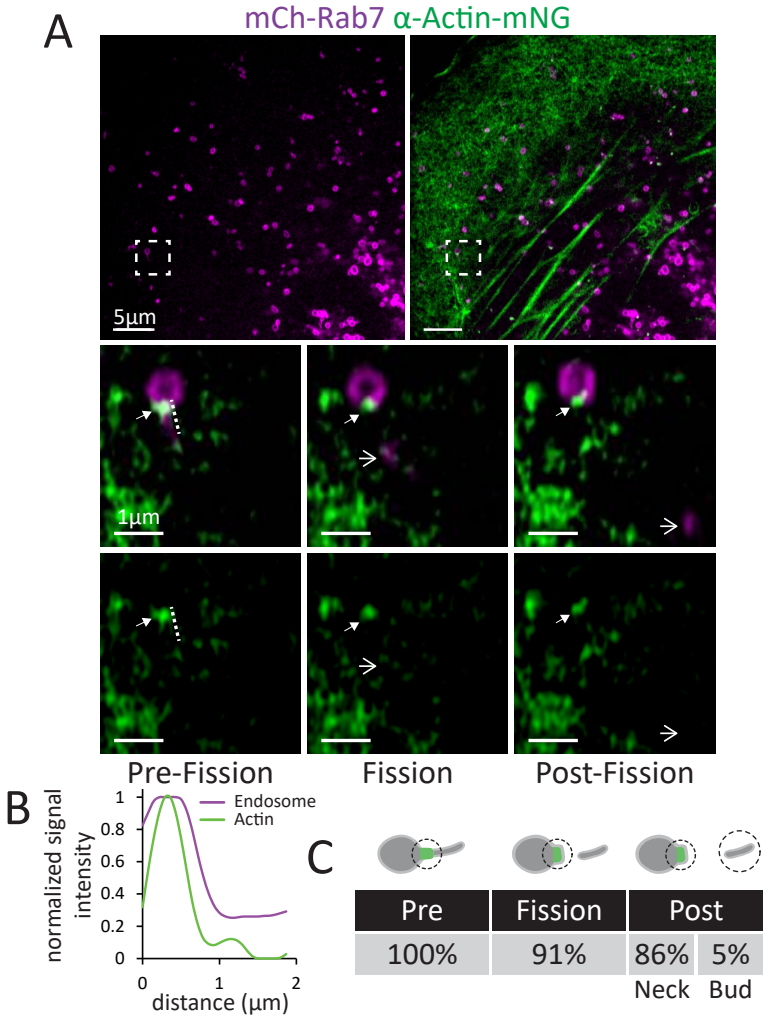

Figure 2.3: (A) Representative images of COS-7 cells transfected with mCh-Rab7 (LE, magenta) and α actin-mNG (actin structure, green). Magnified inset (5 x 5 μm) below shows time lapse of a representative fission event. Block arrowhead indicates the bud neck and line arrowhead indicates departing bud.
(B) Line scan analysis along the length of endosome bud in pre-fission frame from (A) shows α actin-mNG signal labels the base of the bud. Lines are shown in (A) adjacent to actual area measured so as not to obscure region of interest.
(C) Fission events as in (A) were scored for actin enrichment at the bud neck in the pre-fission, fission, and post-fission frames. For post fission frames, both the bud neck and departed bud were scored for positive actin signal. Table shows data as percentage of fission events with enrichment at each stage. For I, n = 19 fission events in 14 cells, performed in triplicate Scale bars for whole cell = 5 μm; insets = 1 μm.

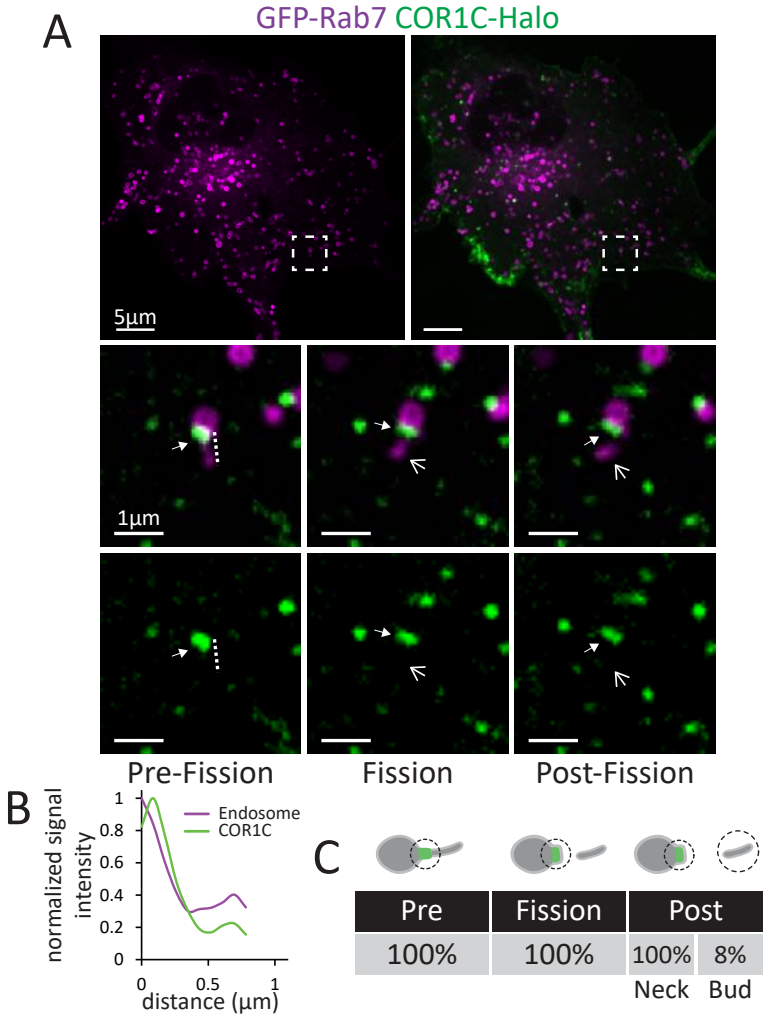

Figure 2.4: (A) Representative images of COS-7 cells transfected with GFP-Rab7 (LE, magenta) and COR1C-Halo (actin structure, green). Magnified inset (5 x 5 μm) below shows time lapse of a representative fission event. Block arrowhead indicates the bud neck and line arrowhead indicates departing bud.
(B) Line scan analysis along the length of endosome bud in pre-fission frame from (A) shows COR1C-Halo signal labels the base of the bud. Lines are shown in (A) adjacent to actual area measured so as not to obscure region of interest.
(C) Fission events as in (A) were scored for COR1C enrichment at the bud neck in the pre-fission, fission, and post-fission frames. For post fission frames, both the bud neck and departed bud were scored for positive actin signal. Table shows data as percentage of fission events with enrichment at each stage. For L, n = 36 fission events in 21 cells, performed in triplicate. Scale bars for whole cell = 5 μm; insets = 1 μm.

in tact. This suggests that endosomes maintain a stable cargo sorting/recycling domain during their maturation process. This would mean that rather than having to reassemble all the sorting and bud shaping factors cargos would instead concentrate at predefined sorting domain and this domain would undergo multiple rounds of sorting and fission. Although, the data is not included here I have observed this over the course of quantifying fission events. This particularly interesting in light of work from my lab and others suggesting that ER exit sites are actually stable assemblies on the ER membrane and facilitate multiple rounds of cargo sorting and exit to the Golgi Westrate et al. [2020], Mccaughey et al. [2019]. These data imply that perhaps this is a conserved feature of membrane proteins sorting.

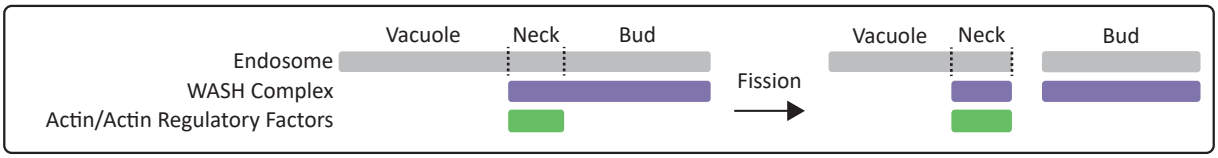

Figure 2.5: Summary diagram of how actin recruitment and regulatory factors divide during fission.

The other interesting observation I made was the difference in localization of the WASH complex and its downstream factors before and during fission. While actin, COR1C, and ARP3 were all confined to the bud neck and did not leave with the departing bud upon fission FAM21 was localized along the entire length of the bud and was enriched on the post fission bud in all fission events observed. This suggests that the boundary between actin occupied and unoccupied bud membrane marks the point where fission occurs because if all membrane were equally fission component I would expect to see actin and its related factors departing with the bud at a higher frequency. Additionally, these data suggest that there are factors which prevent the WASH complex from activating the ARP2/3 complex and nucleating actin along the length of the bud and factors which prevent actin at the base of the bud from polymerizing along its length. Although, I do not have any data indicating which proteins might prevent WASH from activating ARP2/3 complex distally along the bud, COR1C is a good candidate for limiting proximal actin from polymerizing along the length of the bud.

2.4 Methods

2.4.1 Plasmids and Reagents

GFP-Rab7 and mCh-Rab7 were gifts from P. Chitwood and were described previously (Rowland et al., 2014). Human Rab7 was PCR amplified from human cDNA and cloned into AcGFP/mCherry-C1 with XhoI/HindIII sites. Halo-Rab7 was generated by first PCR amplifying the Halo tag and cloning into AcGFP-C1 via AgeI/SacI sites to generate AcHalo-C1. Primers were JS75 and JS76 (Table S1). Rab7 was PCR amplified from mCh-Rab7 and cloned into AcHalo-C1 via HindIII/KpnI sites. Primers used were JS73 and JS74 (Table S1). COR1C-GFP was gift from Dr. Manojkumar Puthenveedu and Dr. Mark von Zastrow (Puthenveedu et al., 2010). mEmerald-ARP3-N-12 was a gift from Michael Davidson (Addgene plasmid 53995). mCh-FAM21 was described previously (Rowland et al., 2014).

Briefly, it was subcloned from shFAM21/HA-YFP-FAM21 which came as a gift from Dr. Daniel Billadeau. α-actin-mNG and α-actin-Halo were generated by PCR amplification from actin Chromobody TagGFP (Chromotek, acg) and cloning into mNG-N1 or Halo-N1 via XhoI/KpnI sites. Primers used JS69 and JS70 (Table S1).

2.4.2 Transfection

For imaging, COS-7 cells (ATCC tested for mycoplasma before delivery and freezing) were seeded on 35mm glass bottom dishes (Cellvis, D35-20-1.5-N) in DMEM (GIBCO, 12430-054) containing 10% FBS and 50 units/mL Penicillin, 50 μg/mL Streptomycin (Invitrogen, 15070063) for 16 h, then transfected with plasmids using Lipofectamine 3000 following manufacturer's protocol. Briefly, two separate 250 μL mixes were prepared with Opti-MEM (Invitrogen, 31985-088). One mix received plasmids intended for transfection and 2 μL P3000 reagent per μg of plasmid. The second mix received 5 μL Lipofectamine 3000. These mixes were combined after a 5 min room temperature incubation. This is followed by a 20 min room temperature incubation where upon the combined mix was added to the imaging dish dropwise. Prior to transfection mix addition, cells were rinsed once with 1x PBS and then placed in 1.5 ml Opti-MEM. Cells were incubated with transfection mix for 5 h and then rinsed once with 1x PBS and then placed in 2 ml DMEM. Cells were then imaged 16 h later in 1.5 ml FluoroBrite DMEM (GIBCO, Cat. A18967-01) containing 10% FBS, 25 mM HEPES, and 1x GlutaMAX (GIBCO, 35050061). Cells transfected with halo tag had 100nM Janelia Fluor 646 halo ligand, provided by Luke Lavis, added to the imaging media and were incubated with ligand for 30 min prior to imaging.

The following concentrations were used for each plasmid: 25 ng/ml mCh-Rab7; 25 ng/ml GFP-Rab7 (imaging and TurboID); 25 ng/ml Halo-Rab7; 25 ng/ml COR1C-Halo; 75 ng/ml ARP3-mEm; 250 ng/ml mCh-FAM21; 150 ng/ml GFP VPS35; 50 ng/ml α-actin-mNG; 50 ng/ml α-actin-Halo; 225 ng/ml BFP Sec61β.

2.4.3 Microscopy

Cells were imaged via a spinning disk confocal microscope or confocal line scanning microscope. The spinning disk confocal microscope consists of Nikon eclipse Ti2 inverted microscope body equipped with; PSF unit, Yokagowa CSU-X1 spinning disk confocal scanner; an Andor iXon 897 electron-multiplying charge-coupled device 512x512 camera; and OBIS 405, 488, 561, 640 nm lasers. Images were acquired with 100× 1.45-NA Plan Apo objective using Micro-Manager software and ImageJ (National Institutes of Health). For Fig. 1 D-I Airyscan LSM 880 was used all other images were acquired on spinning disk detailed above. The line scanning confocal consists of Zeiss Axio Observer inverted fluorescence microscope body equipped with LSM 880, and Airyscan detector. Images were acquired with 63× 1.4-NA Plan Apo objective Zeiss Zen Software.

2.4.4 Statistics

All data described are from at least three biological replicates. All data were graphed as box and whisker plots with median (indicated by line) and mean (indicated by X) shown. When comparing two samples, two-tailed Student's t tests were used. For comparisons across multiple samples significance testing was done by first establishing significant differences exist between conditions by one way ANOVA. If variation between conditions was significantly greater then with in conditions this was followed by post hoc significance testing with Tukey's Test. ns = not significant, *$p < 0.05$, **$p < 0.01$, ***$p < 0.001$. Analyses were all performed using GraphPad Prism 8. Details of significance calculations as well as n values for each quantification are reported in the relevant figure legends.

2.5 Acknowledgements

I thank V. Olsen for assistance generating plasmids. I thank E. Sawyer, T. Nguyen, H. Wu, E. Zamponi, and V. Olsen for insight and helpful discussion. J.F. Striepen was supported

by a graduate training grant in signaling and cellular regulation (NIH T32 GM008759). This work was also supported by a grant from the NIH to G.K. Voeltz. (GM120998). G.K. Voeltz. is an investigator of the Howard Hughes Medical Institute.

Chapter 3

Type I coronins confine actin to the bud neck.

3.1 Introduction

My data demonstrate that a component of the WASH complex localizes along the entire length of the bud, whereas actin, ARP2/3, and COR1C are contained to the base of the bud neck (Fig. 2.5). Coronins are actin and ARP2/3 binding proteins which in other circumstances (at the cell cortex) have been shown to influence actin turnover by debranching F-actin Cai et al. [2008], Chan et al. [2011], Cai et al. [2007]. I hypothesized that COR1C might function to similarly destabilize ARP2/3 and to prevent actin polymerization onto the distal part of the endosome bud. My previous results indicate that fission does not occur on actin occupied membrane instead occurring at the edge of these structures. The loss of COR1C might mean that all endosomal bud membrane becomes sheathed in actin resulting in blocking of fission. This would explain why in a COR1C knockdown fission rate is impaired Hoyer et al. [2018].

3.2 Results

To test whether COR1C confines actin at the bud neck, I depleted COR1C from cells and asked if there was an increase in actin signal along the bud. I co-transfected COS-7 cells with mCh-Rab7 (LEs), α-actin-mNG, and either control (CNTRL) or COR1C siRNA and imaged the cells live. COR1C depletion alone was not sufficient to alter actin localization on the bud compared to control (Fig. 3.2 column 1 and 2). There are, however, three Type

I coronin homologs (COR1A, COR1B, and COR1C). These homologs have a well conserved domain structure and there is evidence indicating they can interact with one another Huttlin et al. [2021], Chan et al. [2011] (Fig. 3.1).

I reasoned that in the absence of COR1C, COR1A and COR1B might function redundantly to contain actin to LE bud necks. To deplete combinations of Type I coronin proteins, I co-transfected COS-7 cells with mCh-Rab7 (LEs), α-actin-mNG, and either a control siRNA, COR1C siRNA, COR1C/1A siRNA, COR1C/1B siRNA, or COR1A/1B/1C siRNA. All Type I coronins were efficiently depleted under these conditions (Fig. 3.5). I imaged live cells and collected time-lapse movies to visualize actin patches relative to the endosome buds. When the Type I coronins were depleted in pairs I began to observe actin structures extending along the length of the endosome bud (Fig. 3.2 columns 1 and 2 vs. 3 and 4). When all three Type I coronins were depleted from cells, I scored a marked increase in the number of endosomes with these extended actin buds (Fig. 3.2 column 5). This synergistic effect is shown clearly in the line scans along the bud where actin signal increasingly mirrors bud signal as more Type I coronins are depleted (Fig. 3.2). This contrasts the sharp drop off in actin signal seen in control or COR1C siRNA treatments (Fig. 3.2). I quantified the percent of actin-labeled buds with extended actin per cell and calculated a mean percent under each condition (Fig. 3.3). These data revealed a significant increase in actin localization to the distal bud upon depletion of two or more COR1 homologs and demonstrate that Type I coronins can function redundantly to clear actin from the distal part of the endosome bud.

Notably, the actin extension on the bud caused by Cor1A/1B/1C depletion did not disrupt the recruitment of upstream components required for bud formation/cargo sorting or the sorting of a model membrane cargo the beta-2 adrenergic receptor (ADRB2) into the bud. I co-transfected COS-7 cells with COR1A/1B/1C siRNA to deplete all three coronins, α-actin-Halo to score actin extension, mCh-Rab7 (or GFP-Rab7) to label LEs, and either ARP3-mNG, mCh-FAM21 (WASH complex), GFP-VPS35 (retromer complex),

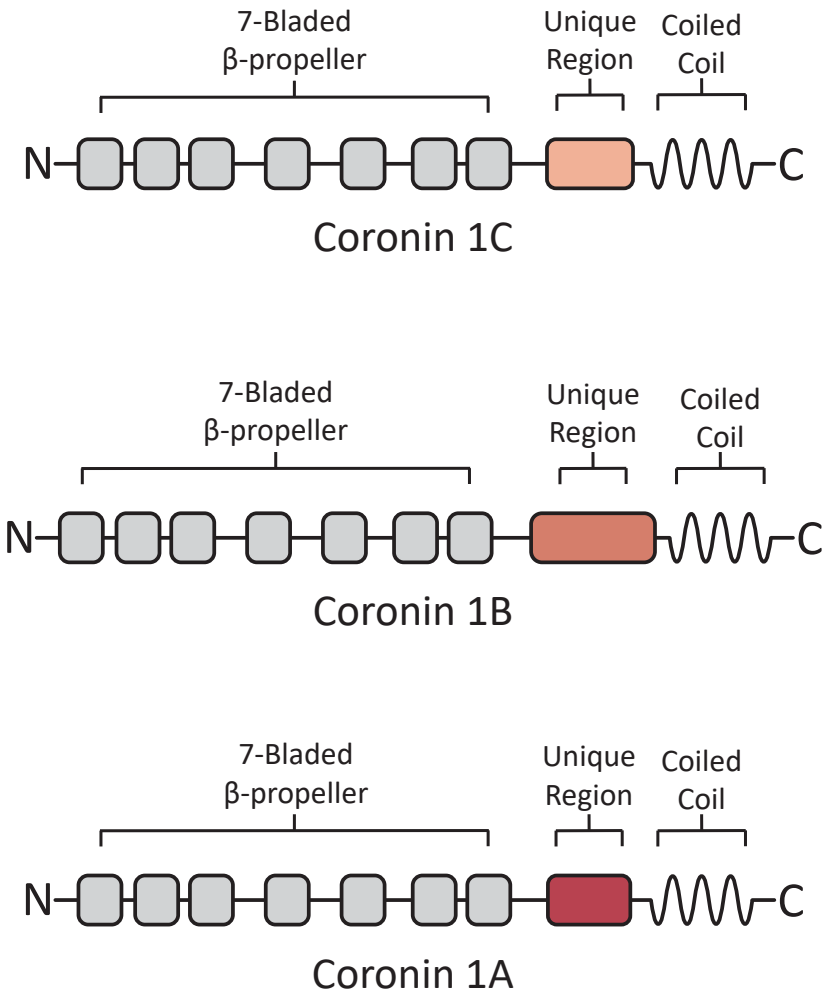

Figure 3.1: Domain diagrams of Type I coronins showing clear conservation of domain structure indicating the possibility of redundant function.

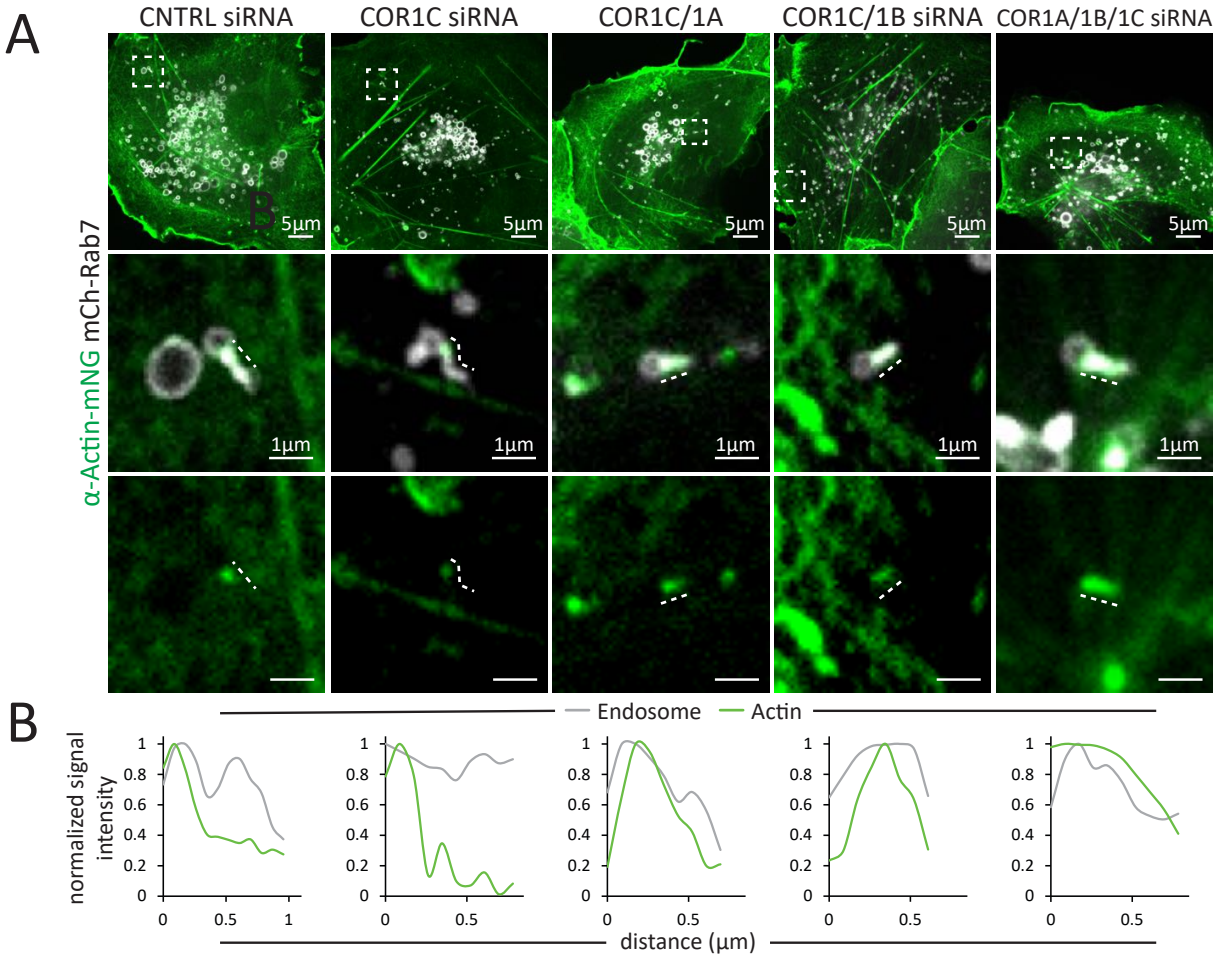

Figure 3.2: (A) Representative images of COS-7 cells transfected with mCh-Rab7 (LE, gray), α actin-mNG (green), and either CNTRL siRNA, COR1C siRNA, COR1C/1A siRNA, COR1C/1B siRNA, or COR1A/1B/1C siRNA. Magnified inset (5 x 5 μm) below shows actin distribution on LE buds. Lines are shown adjacent to actual area measured in B so as not to obscure region of interest. Note: the extension of actin structures along the distal bud with the simultaneous depletion of two or more Type I coronins. Scale bars for whole cell = 5 μm; insets = 1 μm.
(B) Line scan analysis of signal distribution along the bud length for magnified inset examples shown in (B). Lines are shown adjacent to actual area measured to not obscure area of interest. Note, Actin fluorescent signal spreads into the bud matching bud signal as more Type I coronins are depleted.

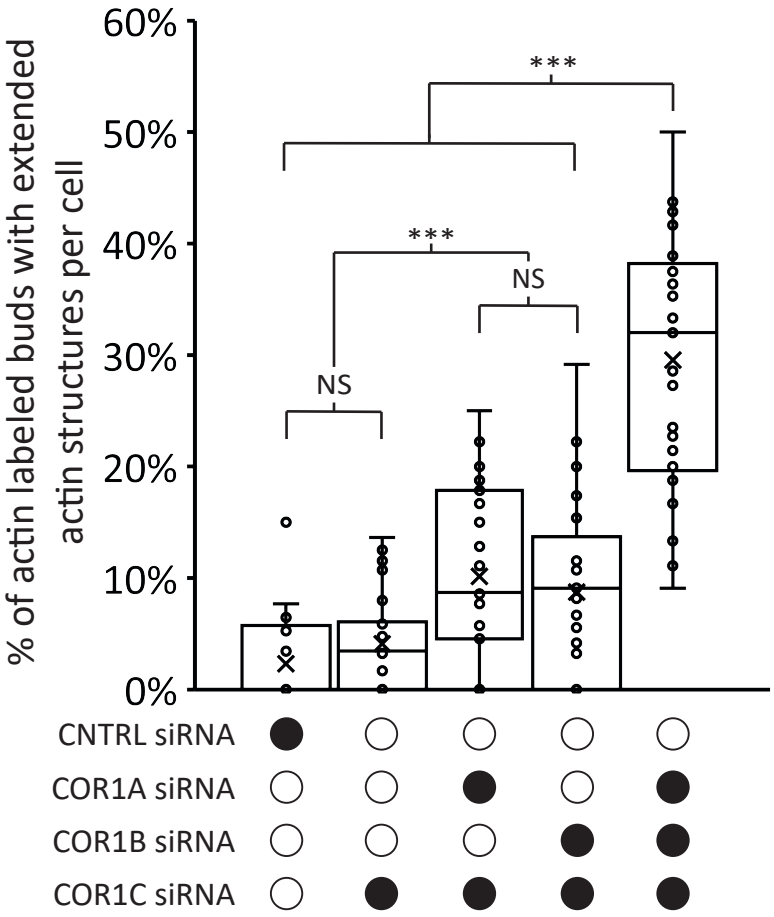

Figure 3.3: Quantification of data in 3.2. Graph of percentage of actin labeled buds with extended actin structures in CNTRL siRNA (for 550 endosomes in n = 32 cells), COR1C siRNA (for 598 endosomes in n = 23 cells), COR1C/1A siRNA (for 668 endosomes in n = 31 cells), COR1C/1B siRNA (for 721 endosomes in n = 29 cells), or COR1A/1B/1C siRNA (for 578 endosomes in n = 29 cells) treated cells, performed in triplicate. X indicates mean and line indicates median. Statistical analyses were performed with one-way ANOVA, p value from Tukey's test: ns = not significant, ***$p < 0.001$.

or FLAG-ADRB2-mNG (membrane cargo). I imaged all markers in live cells and observed efficient enrichment to endosome buds despite the presence of extended actin structures. This supports the idea that these buds are still capable of sorting cargo (Fig. 3.4).

3.3 Discussion

In this chapter I demonstrate that Type I coronins are able to function redundantly at endosome buds to confine actin to the base of the bud. With out the Type I coronins actin localizes along the entire length of the bud mirroring WASH complex localization. The prevalence of this extended actin structure correlates well with the number of Type I coronins depleted from the cell. Interestingly, the proportion of these structures when all three Type I coronins are depleted, while significantly different from the CNTRL siRNA and the dual depletions, is still only 34%. This suggests that there are other mechanisms which work with the Type I coronins to confine actin to the base of the bud. It seems probable that something in the distal portion of the bud prevents ARP2/3 complex activation by the WASH complex.

The redundancy of the Type I coronins is intriguing particularly in light of previous work which shows that COR1A does not enrich at endosome buds normally Hoyer et al. [2018]. It suggests that the different Type I coronins might have developed a selectivity for the type of actin that they regulate and that ones presence excludes the others. Imaging COR1A and endosome buds in the context of a COR1B/1C depletion would be a good way to test this model. If it is true, you would expect to see COR1A enrich more clearly at the endosome bud. Additionally, swapping the different domains of the Type I coronins to see if you can infer preference for one pool of actin over another would be very illuminating for how these proteins are able to enrich. It would also be worth testing other Type I coronins regulated actin pools to understand whether they also function redundantly there. Given the diverse set of cellular functions that Type I coronins have been implicated in having redundancy makes sense.

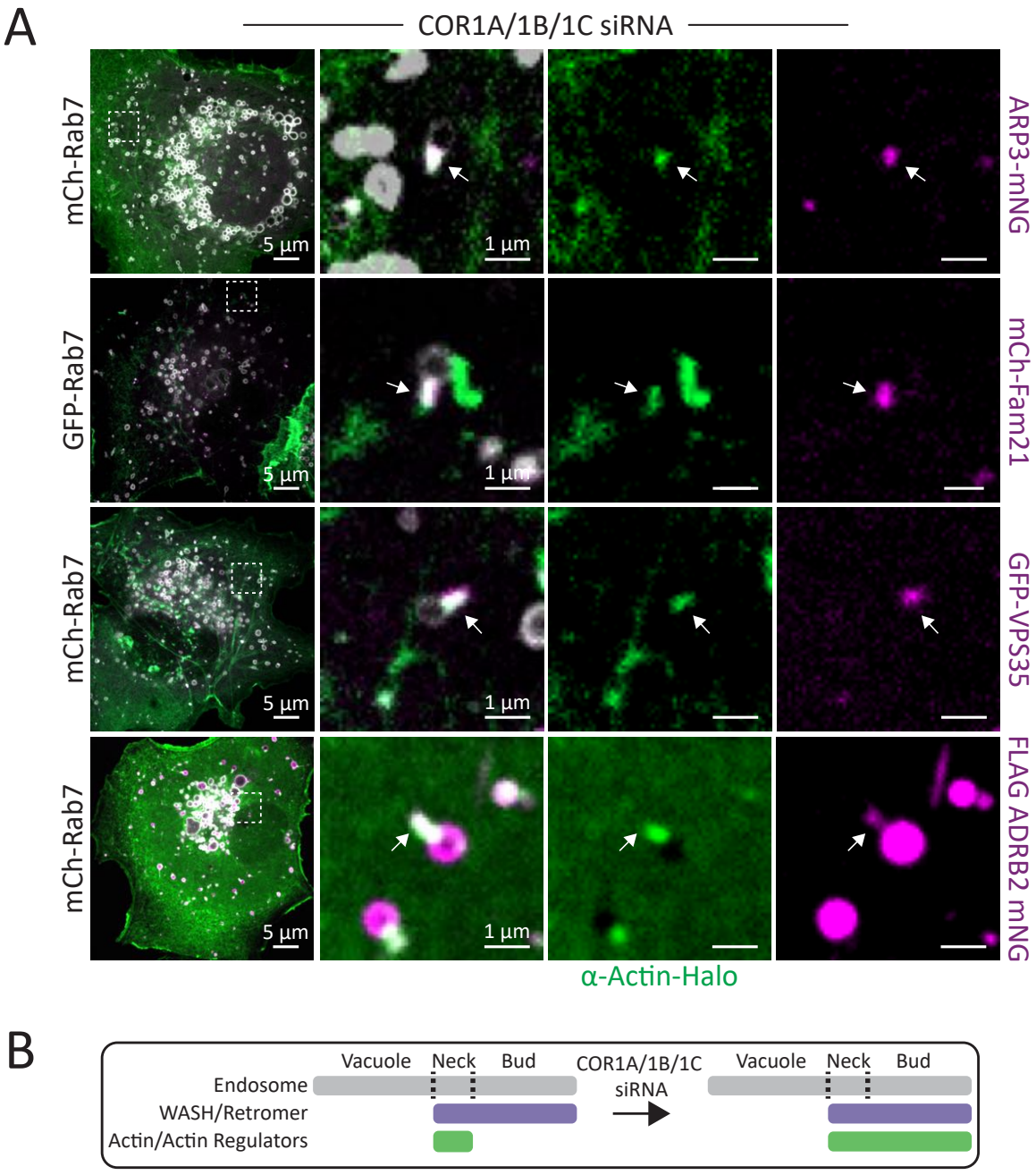

Figure 3.4: A) Representative images of COS-7 cells transfected with mCh-Rab7 or GFP Rab7 (LE, gray), α actin-Halo (green), COR1A/1B/1C siRNA, and with either ARP3-mNG (ARP2/3 complex, magenta), mCh-FAM21 (WASH complex, magenta), GFP-VPS35 (retromer complex, magenta), or FLAG-ARDRB2-mNG (membrane cargo, magenta) reveals that the extended actin structures do not disrupt the recruitment of upstream cargo sorting complexes or sorting of cargo into bud. Arrows indicate endosome bud. Scale bars for whole cell = 5 μm; insets = 1 μm.
(B) Summary figure showing changes in relative localization of actin and cargo sorting components along the endosome.

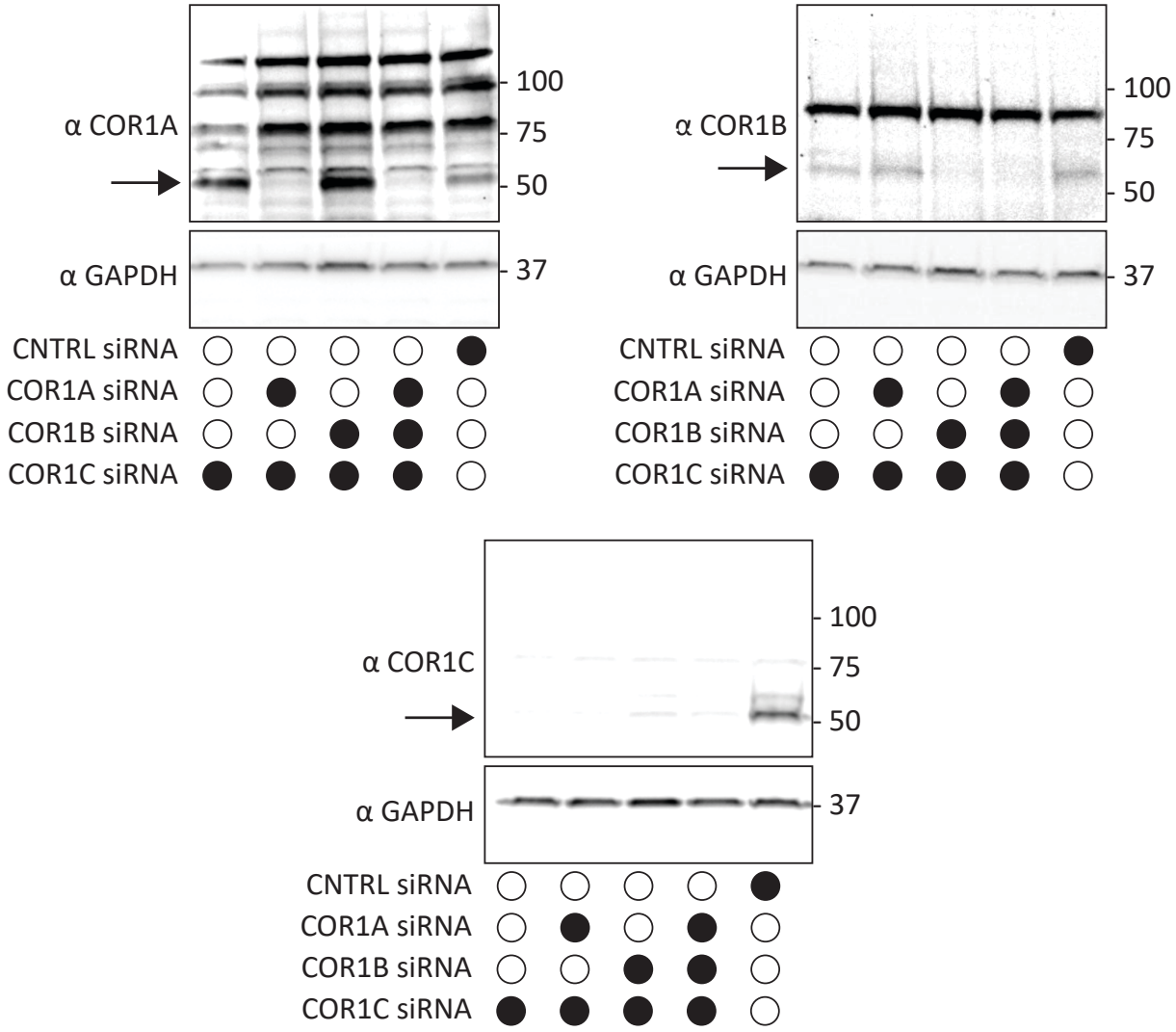

Figure 3.5: Immunoblots for combination depletions tested in Fig. 3.1. Blots show the same samples run three separate times to blot for COR1A, COR1B, and COR1C. Data shows that Type I coronins can be depleted efficiently individually or in combinations.

3.4 Methods

3.4.1 Plasmids and Reagents

GFP-Rab7 and mCh-Rab7 were gifts from P. Chitwood and were described previously (Rowland et al., 2014). Human Rab7 was PCR amplified from human cDNA and cloned into AcGFP/mCherry-C1 with XhoI/HindIII sites. Halo-Rab7 was generated by first PCR amplifying the Halo tag and cloning into AcGFP-C1 via AgeI/SacI sites to generate AcHalo-C1. Primers were JS75 and JS76 (Table S1). Rab7 was PCR amplified from mCh-Rab7 and cloned into AcHalo-C1 via HindIII/KpnI sites. Primers used were JS73 and JS74 (Table S1). COR1C-GFP was gift from Dr. Manojkumar Puthenveedu and Dr. Mark von Zastrow (Puthenveedu et al., 2010). mEmerald-ARP3-N-12 was a gift from Michael Davidson (Addgene plasmid 53995). mCh-FAM21 was described previously (Rowland et al., 2014). Briefly, it was subcloned from shFAM21/HA-YFP-FAM21 which came as a gift from Dr. Daniel Billadeau. α-actin-mNG and α-actin-Halo were generated by PCR amplification from actin Chromobody TagGFP (Chromotek, acg) and cloning into mNG-N1 or Halo-N1 via XhoI/KpnI sites. Primers used JS69 and JS70 (Table S1).FLAG-ADRB2-mNG was generated by PCR amplification from pcDNA3 Flag beta-2-adrenergic-receptor which was a gift from Robert Lefkowitz (Addgene plasmid 14697) and cloning into mNG-N1 via HindIII/PstI sites

Rabbit COR1C polyclonal antibody (Proteintech, 14749-1-AP) was used at 1:2000 for immunoblotting. Rabbit COR1B polyclonal antibody (Abcam, ab119714) 1:2000 for immunoblotting. Rabbit COR1A polyclonal antibody (Abcam, ab123574) 1:2000 for immunoblotting. Rabbit GAPDH antibody (MilliporeSigma, G9545) was used at 1: 100000 for immunoblotting. Anti-Rabbit IgG (whole molecule)-Peroxidase antibody produced in goat (Sigma, A6154) was used at 1:6000 for immunoblotting. Anti-Mouse IgG (whole molecule)-Peroxidase antibody produced in goat (Sigma, A4416) was used at 1:3000 for immunoblotting.

3.4.2 Transfection

For imaging, COS-7 cells (ATCC tested for mycoplasma before delivery and freezing) were seeded on 35mm glass bottom dishes (Cellvis, D35-20-1.5-N) in DMEM (GIBCO, 12430-054) containing 10% FBS and 50 units/mL Penicillin, 50 μg/mL Streptomycin (Invitrogen, 15070063) for 16 h, then transfected with plasmids using Lipofectamine 3000 following manufacturer's protocol. Briefly, two separate 250 μL mixes were prepared with Opti-MEM (Invitrogen, 31985-088). One mix received plasmids intended for transfection and 2 μL P3000 reagent per μg of plasmid. The second mix received 5 μL Lipofectamine 3000. These mixes were combined after a 5 min room temperature incubation. This is followed by a 20 min room temperature incubation where upon the combined mix was added to the imaging dish dropwise. Prior to transfection mix addition, cells were rinsed once with 1x PBS and then placed in 1.5 ml Opti-MEM. Cells were incubated with transfection mix for 5 h and then rinsed once with 1x PBS and then placed in 2 ml DMEM. Cells were then imaged 16 h later in 1.5 ml FluoroBrite DMEM (GIBCO, Cat. A18967-01) containing 10% FBS, 25 mM HEPES, and 1x GlutaMAX (GIBCO, 35050061). Cells transfected with halo tag had 100nM Janelia Fluor 646 halo ligand, provided by Luke Lavis, added to the imaging media and were incubated with ligand for 30 min prior to imaging.

The following concentrations were used for each plasmid: 25 ng/ml mCh-Rab7; 25 ng/ml GFP-Rab7 (imaging and TurboID); 25 ng/ml Halo-Rab7; 25 ng/ml COR1C-Halo; 75 ng/ml ARP3-mEm; 250 ng/ml mCh-FAM21; 150 ng/ml GFP VPS35; 50 ng/ml α-actin-mNG; 200 ng/ml FLAG-ADRB2-mNG; 50 ng/ml α-actin-Halo; 225 ng/ml BFP Sec61β.

3.4.3 Knockdown with siRNA

Cells were seeded in 2ml wells, as described previously, for 16 h. Cells were then transfected with siRNA at concentrations listed below with DharmaFECT 1 transfection reagent in DMEM containing 10% FBS for 6 h. Cells were allowed to recover for 40 h before

transfecting with same amount of siRNA and plasmids marking structures of interest as described previously. After transfection cells were split into imaging dish and 2ml for KD confirmation via western.

Cells were transfected with 25nM negative control siRNA (single KD) or 75nM negative control siRNA (Type I coronin KD) (Ambion AM4635) or 25nM siRNA against COR1C (Dharmacon ON-TARGETplus SMARTPool L-017331-00-0010), 25nM siRNA against COR1A (Dharmacon ON-TARGETplus SMARTPool L-012771-00-0010), 25nM siRNA against COR1B (Dharmacon ON-TARGETplus SMARTPool L-010493-01-0010).

3.4.4 Microscopy

Cells were imaged via a spinning disk confocal microscope or confocal line scanning microscope. The spinning disk confocal microscope consists of Nikon eclipse Ti2 inverted microscope body equipped with; PSF unit, Yokagowa CSU-X1 spinning disk confocal scanner; an Andor iXon 897 electron-multiplying charge-coupled device 512x512 camera; and OBIS 405, 488, 561, 640 nm lasers. Images were acquired with 100× 1.45-NA Plan Apo objective using Micro-Manager software and ImageJ (National Institutes of Health). For Fig. 1 D-I Airyscan LSM 880 was used all other images were acquired on spinning disk detailed above. The line scanning confocal consists of Zeiss Axio Observer inverted fluorescence microscope body equipped with LSM 880, and Airyscan detector. Images were acquired with 63× 1.4-NA Plan Apo objective Zeiss Zen Software.

3.4.5 Statistics

All data described are from at least three biological replicates. All data were graphed as box and whisker plots with median (indicated by line) and mean (indicated by X) shown. When comparing two samples, two-tailed Student's t tests were used. For comparisons across multiple samples significance testing was done by first establishing significant differences exist between conditions by one way ANOVA. If variation between conditions was significantly

greater then with in conditions this was followed by post hoc significance testing with Tukey's Test. ns = not significant, *p < 0.05, **p < 0.01, ***p < 0.001. Analyses were all performed using GraphPad Prism 8. Details of significance calculations as well as n values for each quantification are reported in the relevant figure legends.

3.4.6 Extended Actin Structures Quantification

To count the number of extended actin structures on endosomes COS-7 cells in different knockdowns or knockdown rescues treatments were transfected with either GFP-Rab7 mCh-Rab7 (LE) and α-actin-mNG (actin). Cells were imaged for 1 min at 2 sec intervals. The number of actin labeled buds in each cell over the time lapse was counted. The number of those buds which qualified as extended actin buds was also counted. Extended actin buds were defined as buds longer then 250 nm with actin enrichment which covered more than half the bud for more than 3 consecutive frames. The ratio of actin labeled buds to extended actin buds was calculated per cell.

3.5 Acknowledgements

I thank V. Olsen for assistance generating plasmids. I thank E. Sawyer, T. Nguyen, H. Wu, E. Zamponi, and V. Olsen for insight and helpful discussion. J.F. Striepen was supported by a graduate training grant in signaling and cellular regulation (NIH T32 GM008759). This work was also supported by a grant from the NIH to G.K. Voeltz. (GM120998). G.K. Voeltz. is an investigator of the Howard Hughes Medical Institute.

Chapter 4

COR1C's CC is necessary and sufficient to drive enrichment at the endosome bud and confine actin.

4.1 Introduction

Having established the importance of type I coronins for confining actin to the endosome bud base we wanted to understand more about the function of COR1C specifically. Of the Type I coronins COR1C localizes most prominently to the endosome bud and its depletion was previously shown to reduce endosome fission rate Hoyer et al. [2018]. To do this we needed to establish first that COR1C alone would be sufficient to restore actin confinement. Then it would be possible to do generate domain deletions and use these to establish which portions of COR1C were important for rescue. Given the high degree of conservation between the Type I coronins this could also give insight into what allows COR1C to uniquely enrich at endosome buds.

4.2 Results

4.2.1 Type I coronin depletion can be rescued by COR1C.

Although COR1C depletion was not sufficient to cause actin extension along the LE bud, we know that COR1C enriches at the bud neck of LEs (Fig. 2.4) and to a greater degree than COR1A, suggesting COR1C might function specifically at the LE Hoyer et al. [2018]. We asked whether the re-introduction of COR1C would be sufficient to restrict actin to the base of the LE bud in Type I coronin depleted cells. COS-7 cells were co-transfected

with COR1A/1B/1C siRNA (to deplete all three Type I coronins), GFP-Rab7 (LEs), mCh-FAM21 (WASH buds) and an siRNA resistant Halo-tagged COR1C re-expression construct (siRES COR1C-Halo). Immuno-blot analysis confirmed that COR1A/1B/1C were efficiently depleted and that the rescue construct was expressed at similar levels to endogenous COR1C (Fig. 4.6). We imaged live cells and calculated the mean percent of actin labeled buds with extended actin per cell (Fig. 4.2 4.3). The COR1C re-expression construct localizes to the base of the bud and reduces actin extension down to levels not significantly different from control siRNA treatment (in 2.3% CNTRL Fig. 3.3 vs. 9.7% in WT Fig. 4.3).

Next, we generated several Halo tagged siRNA resistant deletion mutants of COR1C to test which of its structural domains are required for actin disassembly and/or bud localization. Type I coronins contain several characteristic structural domains; a seven bladed beta propeller region formed from WD40 repeat domains, a unique domain, and a carboxy terminal (C-term) coiled-coil (CC) (see cartoon of domain structure in Fig. 3.1, 4.1). The beta propeller contains a single actin binding domain, which is conserved among Type-1 coronins. COR1C also has a non-conserved secondary actin binding site in its unique domain Chan et al. [2012]. The CC was shown to be uniquely essential for COR1C's association with actin filaments Spoerl et al. [2002]. This CC was of particular interest because the single yeast coronin (Crn1) which also has two actin binding domains uses the CC to bind and regulate ARP2/3 Humphries et al. [2002]. Mutants generated were as follows: an actin binding deficient mutant (COR1C ACT-; R28D, K418E/K419E, K427E/K428E these mutations are sufficient to abrogate actin binding in vitro Chan et al. [2012]), a C-term CC deletion mutant (COR1C ΔCC; residues 1-444 predicted to abrogate ARP2/3 binding based on homology to Crn1), a combination of the two (COR1C ACT- ΔCC), and a truncation containing only C-term CC (COR1C-CC; residues 414-474) (Fig. 4.1). We co-transfected COS-7 cells with COR1A/1B/1C siRNA to deplete all Type I coronins, α-actin-mNG, mCh-Rab7 (LE), and compared phenotypes upon re-expression of either siRES full length COR1C-Halo, siRES COR1C ACT–Halo, siRES COR1C ΔCC-Halo, siRES COR1C ACT- ΔCC-Halo, or siRES

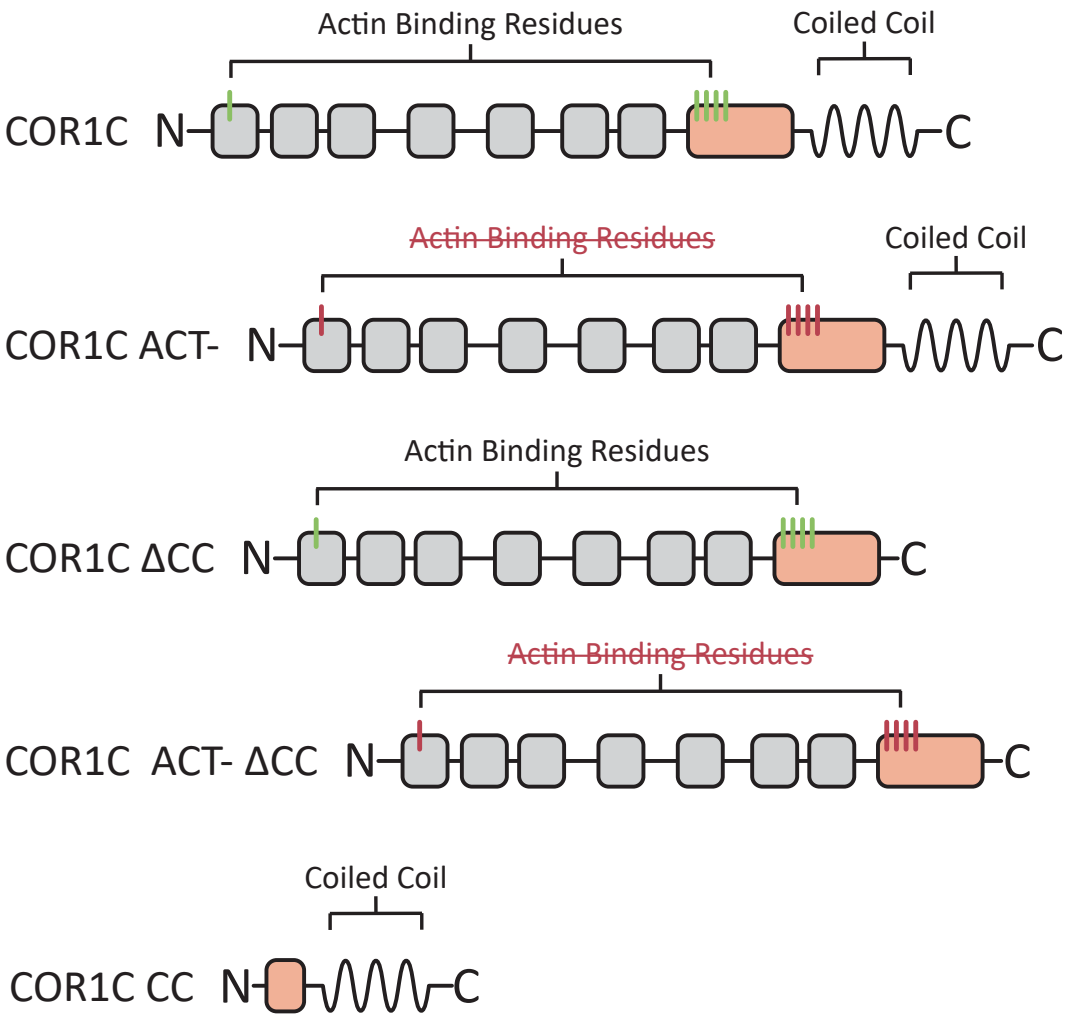

Figure 4.1: ACT- indicates point mutations in actin binding residues (R28D, K418E/K419E, K427E/K428E). ΔCC indicates a truncation removing the CC (COR1C residues 1-444). CC indicates predicted CC along with 30 upstream AA (COR1C residues 414-474)

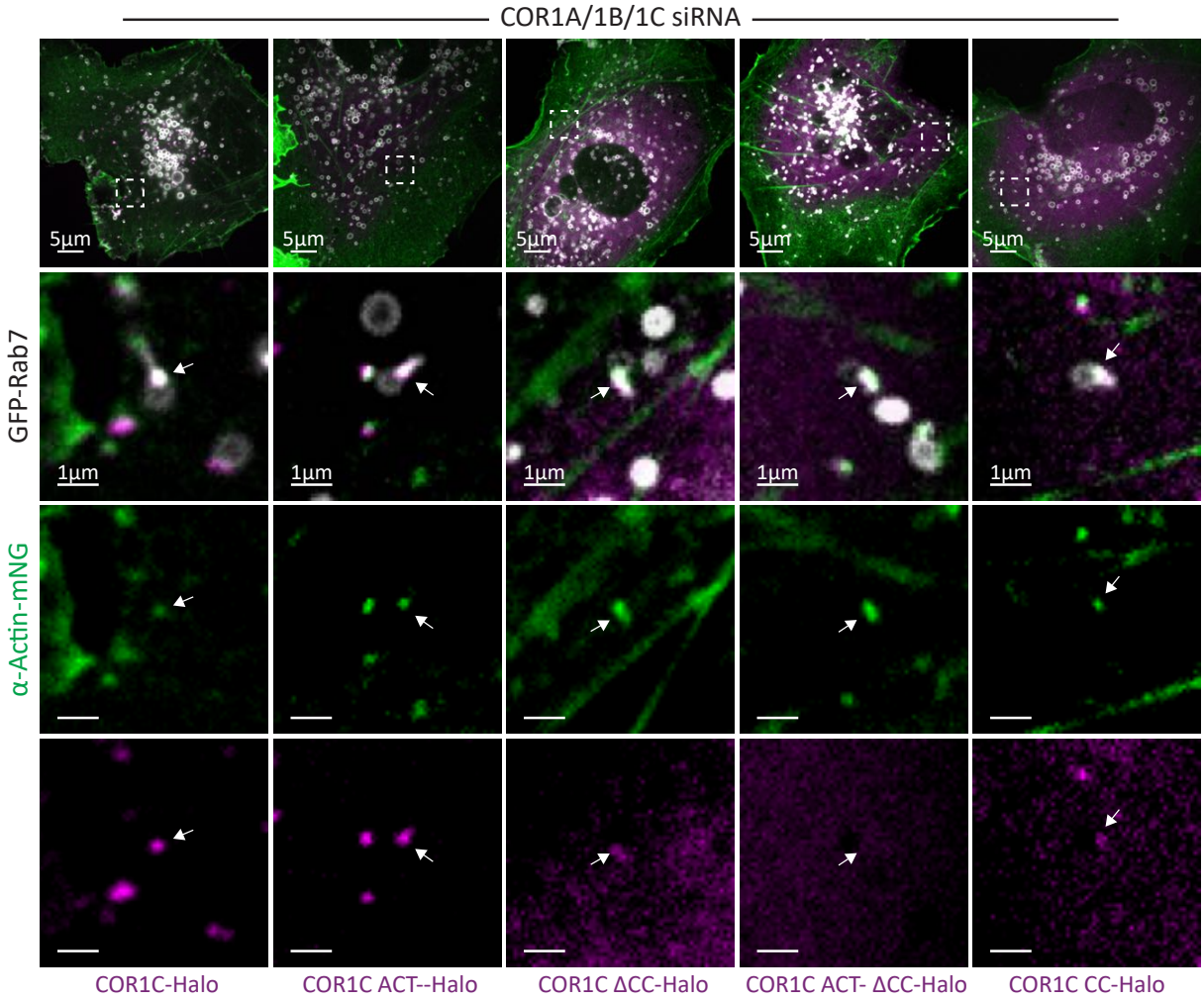

Figure 4.2: Representative images of COS-7 cells co-transfected with COR1A/1B/1C siRNA to deplete all Type I coronins and with mCh-Rab7 (LE, gray), α-actin-mNG (green), and either siRES COR1C-Halo, siRES COR1C ACT–Halo, siRES COR1C ΔCC-Halo, siRES COR1C ACT- ΔCC-Halo, or siRES COR1C CC-Halo (magenta) to identify which domains are required to clear the extended actin structure from the bud. Magnified inset (5 x 5 μm) show representative examples of actin positive endosome buds (at arrow). Scale bars for whole cell = 5 μm; insets = 1 μm.

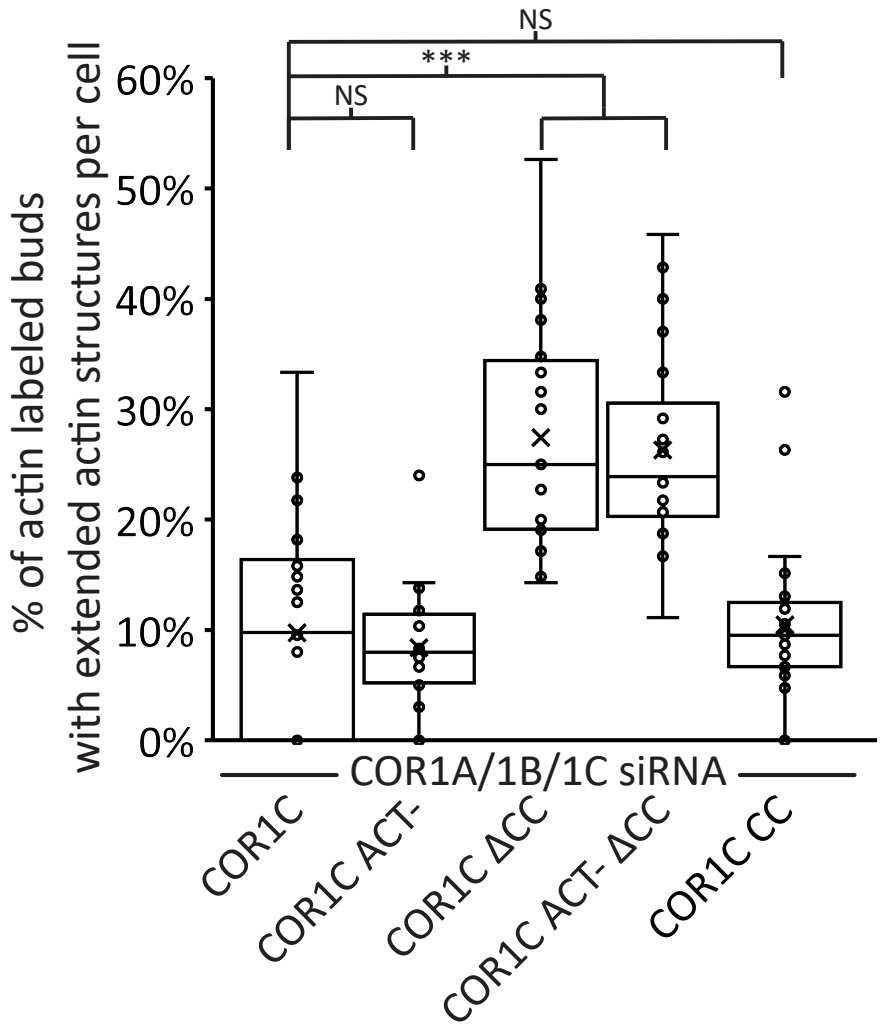

Figure 4.3: Quantification of data in 4.2. Graph shows percent of actin labeled buds with extended actin structures per cell from: siRES COR1C-Halo: 480 endosomes in n = 22 cells; siRES COR1C ACT–Halo: 578 endosomes in n = 21 cells; siRES COR1C ΔCC-Halo: 575 endosomes in n = 24 cells; siRES COR1C ACT- ΔCC-Halo: 549 endosomes in n = 22 cell; and siRES COR1C CC-Halo: 616 endosomes in n = 23 cells, performed in triplicate. Statistical analyses were performed with one-way ANOVA, p value from Tukey's test: ns = not significant, *$p < 0.05$, **$p < 0.01$, ***$p < 0.001$.

COR1C CC-Halo (Fig. 4.6, 4.7, 4.1, 4.2, 4.3). Immunoblot analysis confirmed that endogenous COR1A/1B/1C were efficiently depleted and that the rescue constructs were expressed at similar levels to each other and to endogenous COR1C (Fig. 4.7, 4.1). Cells were imaged live and the mean percent of actin labeled buds with extended actin per cell was scored for each rescue condition (Fig. 4.3). Interestingly, mutants lacking the CC did not ΔCC-Halo, 26% COR1C ACT- ΔCC-Halo). Strikingly, the CC alone was sufficient to reduce the extended actin to the same degree as WT (Fig. 4.3, 10%, 9.7% respectively).

4.2.2 The COR1C CC is necessary and sufficient for COR1C enrichment at LE buds.

We measured to what extent COR1C mutants that rescue actin clearance from the distal bud are also able to enrich to the LE bud in the absence of extended actin structures. This analysis was performed in COR1C depleted cells to avoid any chance of homo-dimerization with endogenous COR1C Chan et al. [2012]. COS-7 cells were co-transfected with COR1C siRNA, GFP-Rab7 (LEs), mCh-FAM21 (WASH complex), and either siRES COR1C-Halo, siRES COR1C ACT–Halo, siRES COR1C ΔCC-Halo, siRES COR1C ACT- ΔCC-Halo, or siRES COR1C CC-Halo. Cells were imaged live to visualize recruitment of the COR1C constructs to FAM21-labelled budding domains (Fig. 4.4). To score the enrichment of each mutant at FAM21 domains, we traced a region of interest (ROI) around the FAM21 signal on the bud and the fluorescence intensity of COR1C signal within the ROI was measured (Fig. 4.5). We calculated the fold enrichment of COR1C signal at the ROI compared to its signal in the cytoplasm. On average siRES-full length COR1C-Halo enriches threefold over background cytoplasmic signal, while deleting the CC domain completely disrupted recruitment of COR1C to the endosome bud (Fig. 4.5, 4.4). By comparison, constructs with the actin binding domain mutated were still recruited but at a reduced level (1.5-fold over cytoplasmic background). Interestingly, the COR1C CC domain alone was still significantly recruited to the endosome bud, albeit at reduced levels compared to wild type (Fig. 4.5,

4.4). These data demonstrate that while the actin binding residues aid in recruitment to the FAM21-labelled endosome bud, they are not required. The C-terminal CC however, is clearly both necessary and sufficient for COR1C enrichment on the late endosome bud. This corresponds well with its ability to rescue actin clearance, suggesting these mutants are acting directly on endosomal actin (Fig. 3.2).

4.3 Discussion

In this chapter we demonstrated that the COR1C CC is necessary sufficient to rescue actin confinement at the bud neck and to enrich the protein at the endosome bud. This is surprising given that the domain makes up a relatively small portion of the protein. These results highlight how important interaction with the ARP2/3 complex likely is for the localization and function of COR1C. Although interaction between COR1C and ARP2/3 complex via the CC has not been demonstrated yet previous work with other Type I coronins supports this idea Humphries et al. [2002].

The CC is necessary and sufficient to restore actin confinement but it seems unlikely that the rest of the protein has no role to play at the fission site. It is possible that in the absence of signaling cues the steady state cellular function only requires the CC. Perhaps manipulating the cell in ways where recycling from the LE is changed would reveal an incomplete rescue. It is also possible that although the size of the actin structure is rescued some other characteristics of bud actin are not. For example actin turn over and branch number are not quantified here and could be altered in a CC alone rescue.

4.4 Methods

4.4.1 Plasmids and Reagents

GFP-Rab7 and mCh-Rab7 were gifts from P. Chitwood and were described previously (Rowland et al., 2014). Human Rab7 was PCR amplified from human cDNA and cloned

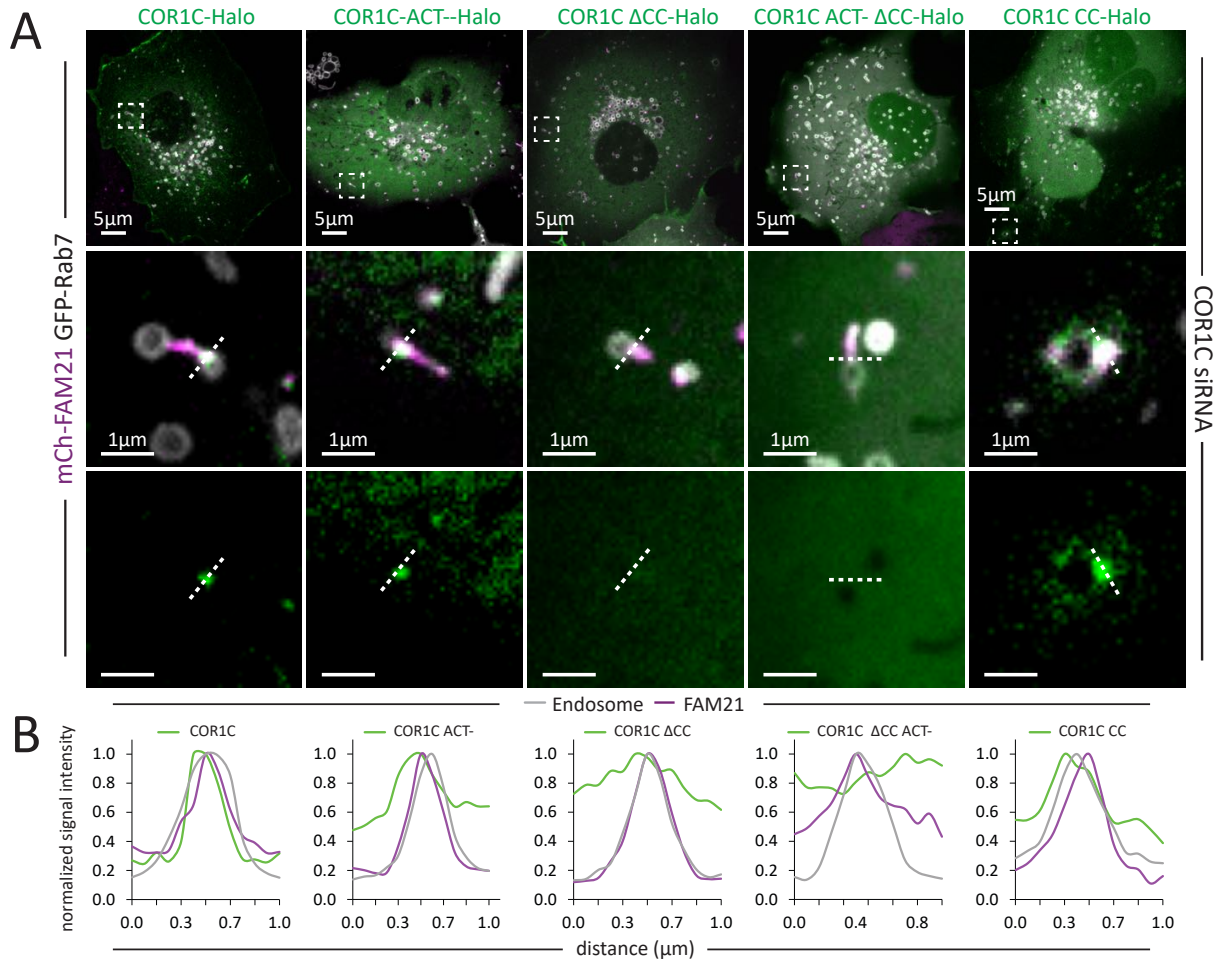

Figure 4.4: (A) Representative images of COS-7 cells co-transfected with COR1C siRNA (for depletion), GFP-Rab7 (LE, gray), mCh-FAM21 (WASH complex, magenta) and either siRES COR1C-Halo, siRES COR1C ACT–Halo, siRES COR1C ΔCC-Halo, siRES COR1C ACT-ΔCC-Halo, or siRES COR1C CC-Halo (green) to measure the relative levels of recruitment to FAM21 marked buds for different COR1C mutants. Magnified insets (5 x 5 μm) of representative endosomes with FAM21 marked buds shown on right. Dashed line indicates where line-scan analysis in (B) was done. Scale bars for whole cell = 5 μm; insets = 1 μm. (B) Line scan analysis of dashed lines shown in (A) are positioned to cross perpendicular to bud neck. Matching COR1C peaks indicate enrichment at the FAM21 labeled bud. Note that constructs lacking the CC do not form clear peaks.

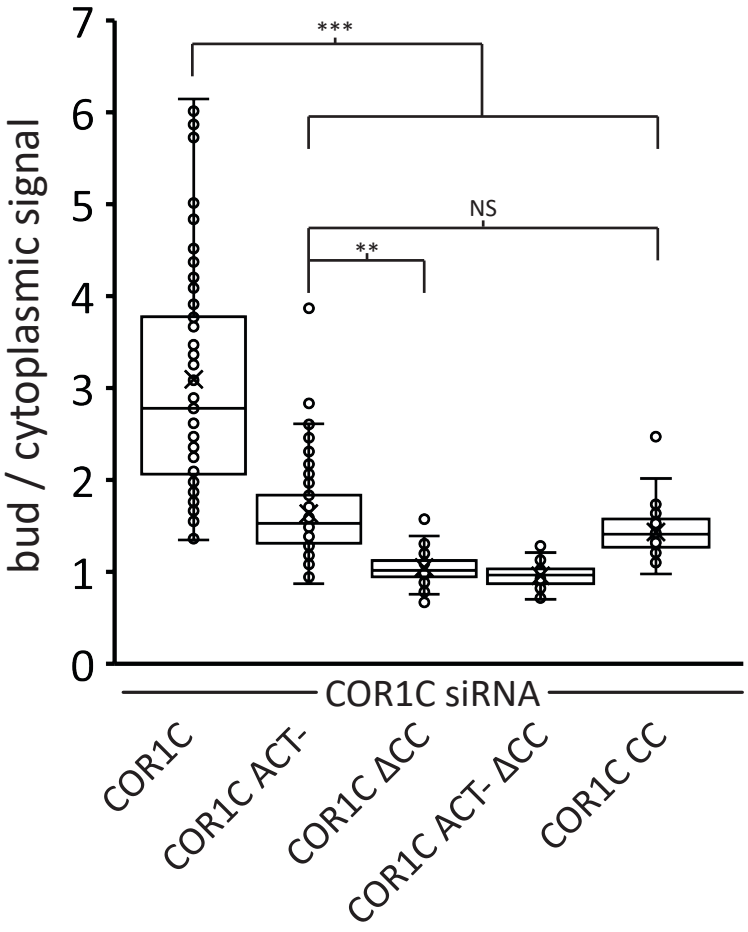

Figure 4.5: Graph of data from experiment 4.4. Halo signal enrichment at FAM21 buds relative to background is scored for the following samples: siRES COR1C-Halo: n = 79 endosomes in 9 cells; siRES COR1C ACT–Halo: n = 87 endosomes in 9 cells; siRES COR1C ΔCC-Halo: n = 80 endosomes in 9 cells; siRES COR1C ACT- ΔCC-Halo: n = 75 endosomes in 10 cells; and siRES COR1C CC-Halo: n = 67 endosomes in 11 cells, performed in triplicate. Note that values of one indicate no enrichment over cytoplasmic background as in CC deletion. X indicates mean and line indicates median. Statistical analyses were performed with one-way ANOVA, p value from Tukey's test: ns = not significant, *$p < 0.05$, **$p < 0.01$, ***$p < 0.001$.

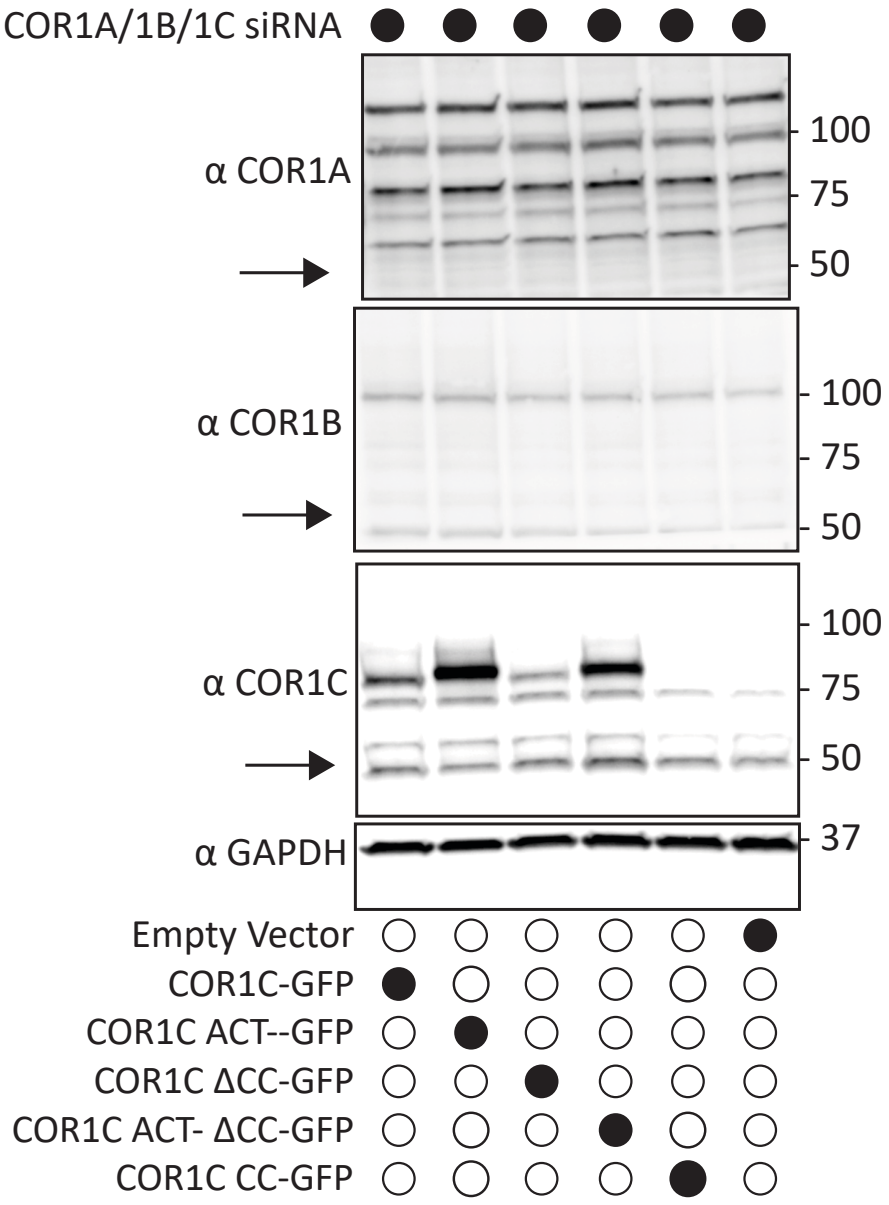

Figure 4.6: Representative immunoblots for Type I coronin depletion (COR1A, COR1B, and COR1C) and rescue as in Fig. 4.2, 4.4. Data shows that Type I coronins can be depleted efficiently and that the siRES COR1C constructs express well and at comparable levels for rescue (analysis was performed in triplicate).

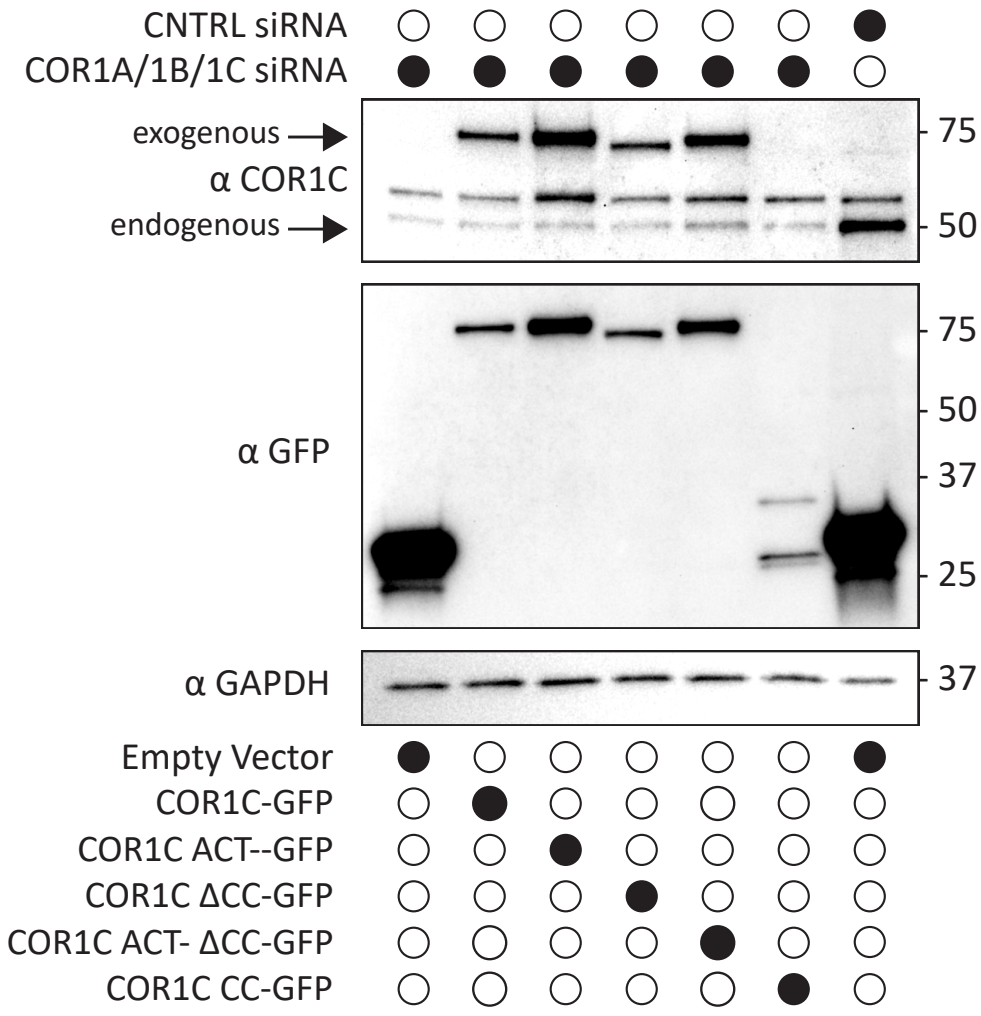

Figure 4.7: Immunoblots for Type I coronin depletion and rescue as in Fig. 4.2, 4.4 showing relative expression of rescue constructs and endogenous COR1C. Representative immunoblots probed with antibody to COR1C, GFP, and GAPDH.

COR1A/1B/1C siRNA		α COR1C: Endg. COR1C norm. CNTRL KD	α COR1C: Exgn. COR1C / Endg. CNTRL KD	α GFP: Exgn. COR1C norm. WT COR1C GFP	Estimated Exgn. / Endg.
CNTRL siRNA +	E-Vector	1			
—	E-Vector	0.151			
—	COR1C WT	0.169	0.339	1	
—	COR1C ACT-	0.160	0.610	2.85	
—	COR1C ΔCC	0.205	0.324	0.960	
—	COR1C ACT-ΔCC	0.204	0.579	2.16	
—	COR1C CC	0.178		2.98	0.864

Table 4.1: Table shows average normalized ratios from three replicates (blots). Values were calculated as indicated in column headers. Briefly, the first column demonstrates clear knock down. The second column demonstrates that expression is comparable between exogenously expressed mutants and is also comparable with endogenous. The third column demonstrates that the relative exogenous rescue expression is comparable to WT rescue. The final column is an estimate of CC expression relative to endogenous COR1C based on the average ratio of anti GFP to anti COR1C signal suggesting that the CC is also not expressed above endogenous. This was necessary because the CC is not detectable via the anti COR1C antibody and so could not be probed for in the same blot.

into AcGFP/mCherry-C1 with XhoI/HindIII sites. Halo-Rab7 was generated by first PCR amplifying the Halo tag and cloning into AcGFP-C1 via AgeI/SacI sites to generate AcHalo-C1. Primers were JS75 and JS76 (Table S1). Rab7 was PCR amplified from mCh-Rab7 and cloned into AcHalo-C1 via HindIII/KpnI sites. Primers used were JS73 and JS74 (Table S1). COR1C-GFP was gift from Dr. Manojkumar Puthenveedu and Dr. Mark von Zastrow (Puthenveedu et al., 2010). mEmerald-ARP3-N-12 was a gift from Michael Davidson (Addgene plasmid 53995). SiRes COR1C-Halo was generated mutating COR1C-GFP by four rounds of site directed mutagenesis to remove siRNA binding to generate siRES COR1C-GFP which was subcloned into Halo-N1 via EcoRI/BamHI to generate siRES COR1C-Halo. SiRES COR1C ACT–Halo was generated by four rounds of site directed mutagenesis of COR1C-GFP to generate COR1C ACT-GFP. Primers used JS29-JS32 and JS34-JS37 (Table S1). COR1C ACT–GFP was then mutated by four rounds of site directed mutagenesis to remove siRNA binding to generate siRES COR1C ACT–GFP which was subcloned into Halo-N1 via EcoRI/BamHI to generate siRES COR1C ACT–Halo. Primers used JS41-JS48 (Table S1). SiRES COR1C ΔCC -Halo was generated by PCR amplification of COR1C-GFP to generate COR1C ΔCC-GFP. Primers used JS19 and JS108 (Table S1). COR1C ΔCC-GFP was then mutated by four rounds of site directed mutagenesis to remove siRNA binding to generate siRES COR1C ΔCC-GFP which was subcloned into Halo-N1 via EcoRI/BamHI to generate siRES COR1C ΔCC -Halo. Primers used JS41-JS48 (Table S1). SiRES COR1C ACT-ΔCC-Halo was generated by four rounds of site directed mutagenesis of COR1C ΔCC-GFP to generate COR1C ACT-ΔCC-GFP. Primers used JS29-JS32 and JS34-JS37 (Table S1). COR1C ACT-ΔCC-GFP was then mutated by four rounds of site directed mutagenesis to remove siRNA binding to generate siRES COR1C ACT-ΔCC-GPF which was subcloned into Halo-N1 via EcoRI/BamHI to generate siRES COR1C ACT-ΔCC-Halo. Primers used JS41-JS48 (Table S1). COR1C CC-Halo was generated by PCR amplified from COR1C-GFP and then cloned into Halo-N1 via HindIII/KpnI sites. Primers used JS109 and JS110 (Table S1). mCh-FAM21 was described previously (Rowland et al., 2014). Briefly, it was

subcloned from shFAM21/HA-YFP-FAM21 which came as a gift from Dr. Daniel Billadeau. α-actin-mNG and α-actin-Halo were generated by PCR amplification from actin Chromobody TagGFP (Chromotek, acg) and cloning into mNG-N1 or Halo-N1 via XhoI/KpnI sites

Rabbit COR1C polyclonal antibody (Proteintech, 14749-1-AP) was used at 1:2000 for immunoblotting. Rabbit COR1B polyclonal antibody (Abcam, ab119714) 1:2000 for immunoblotting. Rabbit COR1A polyclonal antibody (Abcam, ab123574) 1:2000 for immunoblotting. Rabbit GAPDH antibody (MilliporeSigma, G9545) was used at 1: 100000 for immunoblotting. Mouse GFP monoclonal antibody (Clontech Labs 3P Living Colors® A.v. Monoclonal Antibody (JL-8), Fisher Scientific, NC9777966) was used at 1:2000 for immunoblotting. Anti-Rabbit IgG (whole molecule)-Peroxidase antibody produced in goat (Sigma, A6154) was used at 1:6000 for immunoblotting. Anti-Mouse IgG (whole molecule)-Peroxidase antibody produced in goat (Sigma, A4416) was used at 1:3000 for immunoblotting.

4.4.2 Transfection

For imaging, COS-7 cells (ATCC tested for mycoplasma before delivery and freezing) were seeded on 35mm glass bottom dishes (Cellvis, D35-20-1.5-N) in DMEM (GIBCO, 12430-054) containing 10% FBS and 50 units/mL Penicillin, 50 μg/mL Streptomycin (Invitrogen, 15070063) for 16 h, then transfected with plasmids using Lipofectamine 3000 following manufacturer's protocol. Briefly, two separate 250 μL mixes were prepared with Opti-MEM (Invitrogen, 31985-088). One mix received plasmids intended for transfection and 2 μL P3000 reagent per μg of plasmid. The second mix received 5 μL Lipofectamine 3000. These mixes were combined after a 5 min room temperature incubation. This is followed by a 20 min room temperature incubation where upon the combined mix was added to the imaging dish dropwise. Prior to transfection mix addition, cells were rinsed once with 1x PBS and then placed in 1.5 ml Opti-MEM. Cells were incubated with transfection mix for 5 h and then rinsed once with 1x PBS and then placed in 2 ml DMEM. Cells were then imaged 16

h later in 1.5 ml FluoroBrite DMEM (GIBCO, Cat. A18967-01) containing 10% FBS, 25 mM HEPES, and 1x GlutaMAX (GIBCO, 35050061). Cells transfected with halo tag had 100nM Janelia Fluor 646 halo ligand, provided by Luke Lavis, added to the imaging media and were incubated with ligand for 30 min prior to imaging

The following concentrations were used for each plasmid: 25 ng/ml mCh-Rab7; 25 ng/ml GFP-Rab7 (imaging and TurboID); 25 ng/ml Halo-Rab7; 25 ng/ml COR1C-Halo; 50 ng/ml siRES COR1C-GFP (CI-M6PR Rescue); 50 ng/ml SiRES COR1C-Halo (Rescue); 50 ng/ml SiRES COR1C ACT–Halo (Rescue); 75 ng/ml SiRES COR1C ΔCC-Halo (Rescue); 75 ng/ml siRES COR1C ΔCC-GFP (CI-M6PR Rescue); 75 ng/ml SiRES COR1C ACT-ΔCC-Halo (Rescue); 50 ng/ml SiRES COR1C CC-Halo (Rescue); 250 ng/ml mCh-FAM21.

4.4.3 Knockdown with siRNA

Cells were seeded in 2ml wells, as described previously, for 16 h. Cells were then transfected with siRNA at concentrations listed below with DharmaFECT 1 transfection reagent in DMEM containing 10% FBS for 6 h. Cells were allowed to recover for 40 h before transfecting with same amount of siRNA and plasmids marking structures of interest as described previously. After transfection cells were split into imaging dish and 2ml for KD confirmation via western.

Cells were transfected with 25nM negative control siRNA (single KD) or 75nM negative control siRNA (Type I coronin KD) (Ambion AM4635) or 25nM siRNA against COR1C (Dharmacon ON-TARGETplus SMARTPool L-017331-00-0010), 25nM siRNA against COR1A (Dharmacon ON-TARGETplus SMARTPool L-012771-00-0010), 25nM siRNA against COR1B (Dharmacon ON-TARGETplus SMARTPool L-010493-01-0010).

4.4.4 Microscopy

Cells were imaged via a spinning disk confocal microscope or confocal line scanning microscope. The spinning disk confocal microscope consists of Nikon eclipse Ti2 inverted

microscope body equipped with; PSF unit, Yokagowa CSU-X1 spinning disk confocal scanner; an Andor iXon 897 electron-multiplying charge-coupled device 512x512 camera; and OBIS 405, 488, 561, 640 nm lasers. Images were acquired with 100× 1.45-NA Plan Apo objective using Micro-Manager software and ImageJ (National Institutes of Health). For Fig. 1 D-I Airyscan LSM 880 was used all other images were acquired on spinning disk detailed above. The line scanning confocal consists of Zeiss Axio Observer inverted fluorescence microscope body equipped with LSM 880, and Airyscan detector. Images were acquired with 63× 1.4-NA Plan Apo objective Zeiss Zen Software.

4.4.5 Statistics

All data described are from at least three biological replicates. All data were graphed as box and whisker plots with median (indicated by line) and mean (indicated by X) shown. When comparing two samples, two-tailed Student's t tests were used. For comparisons across multiple samples significance testing was done by first establishing significant differences exist between conditions by one way ANOVA. If variation between conditions was significantly greater then with in conditions this was followed by post hoc significance testing with Tukey's Test. ns = not significant, *$p < 0.05$, **$p < 0.01$, ***$p < 0.001$. Analyses were all performed using GraphPad Prism 8. Details of significance calculations as well as n values for each quantification are reported in the relevant figure legends.

4.4.6 Extended Actin Structures Quantification

To count the number of extended actin structures on endosomes COS-7 cells in different knockdowns or knockdown rescues treatments were transfected with either GFP-Rab7 mCh-Rab7 (LE) and α-actin-mNG (actin). Cells were imaged for 1 min at 2 sec intervals. The number of actin labeled buds in each cell over the time lapse was counted. The number of those buds which qualified as extended actin buds was also counted. Extended actin buds were defined as buds longer then 250 nm with actin enrichment which covered more than

half the bud for more than 3 consecutive frames. The ratio of actin labeled buds to extended actin buds was calculated per cell.

4.4.7 COR1C Endosome Enrichment Quantification

To measure COR1C enrichment COS-7 cells were transfected with GFP-Rab7, mCh-FAM21, COR1C siRNA, and rescued with either SiRES COR1C-Halo, SiRES COR1C ACT–Halo, SiRES COR1C ΔCC-Halo, SiRES COR1C ACT-ΔCC-Halo, or SiRES COR1C CC-Halo. Cells were imaged for 1 min at 2 second intervals. For every resolvable FAM21 positive endosome bud the FAM21 signal was traced, and raw integrated density measured in the COR1C channel. Local cytoplasmic signal was collected via measuring raw integrated density of a 1-micron diameter circle which was placed in a proximal cytoplasmic area without endosomes. Background signal was collected by measuring raw integrated density of a 1-micron diameter circle outside the cell. Measurements were normalized by area and then background signal was subtracted from the bud and cytoplasmic signals. Enrichment over cytoplasm was calculated by dividing background corrected bud signal by background corrected cytoplasmic signal.

4.5 Acknowledgements

I thank V. Olsen for assistance generating plasmids. I thank E. Sawyer, T. Nguyen, H. Wu, E. Zamponi, and V. Olsen for insight and helpful discussion. J.F. Striepen was supported by a graduate training grant in signaling and cellular regulation (NIH T32 GM008759). This work was also supported by a grant from the NIH to G.K. Voeltz. (GM120998). G.K. Voeltz. is an investigator of the Howard Hughes Medical Institute. I

Chapter 5

COR1C regulates ARP2/3 complex activity at the endosome bud.

5.1 Introduction

I have demonstrated that Type I coronins are essential for confinement of actin structures the base of the endosome bud. With out the Type I coronins actin extends along the length of the bud. This confinement is restored by reintroduction of just COR1C suggesting although the other proteins have some redundant function COR1C is the essential player at endosomal bud actin. Surprisingly, the CC of COR1C proved to be both necessary and sufficient to restore actin confinement.

The yeast Crn1 which shares the dual actin binding domains of COR1C requires its CC to interact with ARP2/3 complex Humphries et al. [2002]. If COR1C also uses its CC to interact with the ARP2/3 complex it suggest that the key for maintaining actin confinement is ARP2/3 complex interaction and regulation. Type I coronins are a regulatory hub for branched actin and influence its dynamics in numerous ways Cai et al. [2005], Rosentreter et al. [2006], Chan et al. [2011]. Understanding the CC importance at endosomal actin was allowed us to narrow down the list of possible regulatory mechanisms involved and focus on ARP2/3 regulation. In this chapter I detail the experiments that were conducted to support the hypothesis that COR1C regulates ARP2/3 complex activity via its CC on endosomal actin structures.

5.2 Results

Having established COR1C's importance in confining actin, I probed by what mechanism does COR1C regulate actin dynamics on the endosome bud prior to fission. The recruitment of COR1B to the ARP2/3 complex inhibits branched actin nucleation at the cell cortex Cai et al. [2008, 2007]. Thus, I hypothesized that COR1C might also disrupt branched actin on the endosome bud by binding and disrupting ARP2/3 activity. To test this, I asked whether the extended actin phenotype scored in Type I coronin depleted cells could be rescued by treatment with a drug that ectopically inhibits and displaces ARP2/3. I co-transfected COS-7 cells with COR1A/1B/1C siRNA, ARP3-mNG (ARP2/3 complex), mCh-Rab7 (LE), and α-actin-Halo. I then imaged cells for one minute at two second intervals to identify endosomes with extended actin structures. Following this, I treated cells with 150µM CK-666, an inhibitor that binds to ARP2/3 complex locking it in an inactive state, and imaged 30-sec post drug treatment Hetrick et al. [2013]. Inhibition of the ARP2/3 complex quickly depleted the actin and ARP3 marker signal on endosome buds (Fig. 5.1). These data demonstrate that limiting ARP2/3 complex activity is sufficient to reduce the extension of actin structures on endosome buds in Type I coronin depleted cells.

Having established the importance of ARP2/3 complex activity for the extended actin phenotype I hypothesized that COR1C CC is essential for COR1C and ARP2/3 complex interaction given that the CC is both necessary and sufficient for localization and actin confinement. To test this hypothesis, I used a proximity labeling system, which makes use of the promiscuous biotin ligase TurboID Branon et al. [2017]. This system is well suited for capturing dynamic interactions between components on the quickly cycling actin structures present on the bud Puthenveedu et al. [2010], Hoyer et al. [2018]. I created a fusion protein between ARP2/3 complex subunit ARP3 and TurboID. I co-transfected HeLa cells with ARP3-V5-TurboID and either COR1C-GFP, COR1C ACT- ΔCC-GFP, or a background endosomal marker control GFP-Rab7 (Fig. 5.2). I treated transfected cells with biotin for

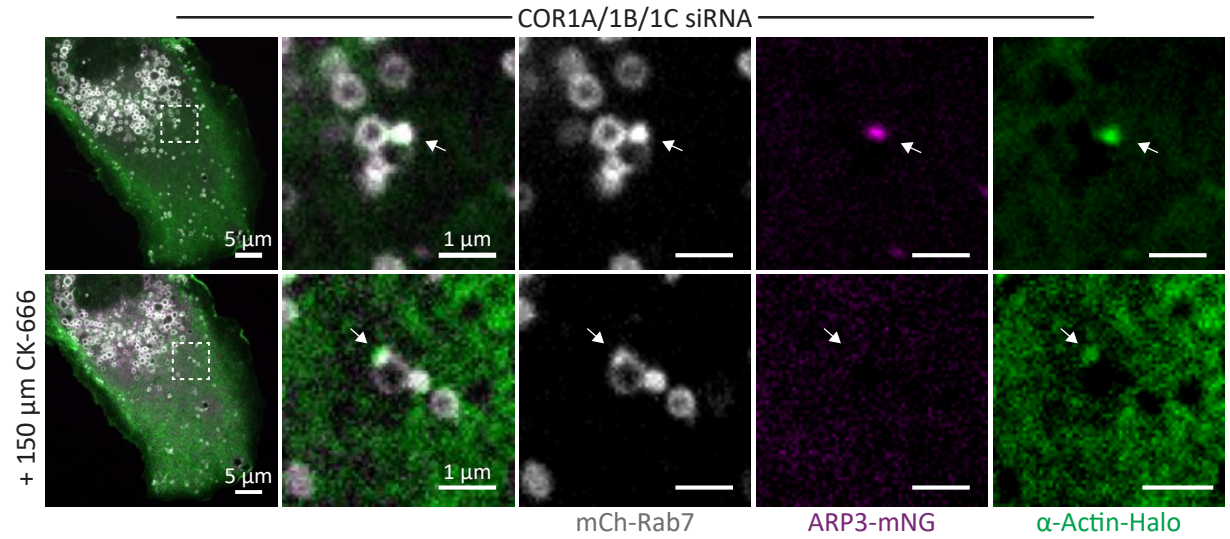

Figure 5.1: Representative images of COS-7 cells co-transfected with COR1A/1B/1C siRNA to deplete all Type I coronins and with mCh-Rab7 (LE, gray), α actin-Halo (green), and ARP3-mNG (magenta). Buds with extended actin (at arrow) were tracked before and after addition of an ARP2/3 complex inhibitor (150 μM CK-666) in merged magnified insets on right (5 x 5 μm). n = 10 cells. Scale bars for whole cell = 5 μm; insets = 1 μm.

three hours, lysed the cells, and used biotin antibody agarose beads to enrich for biotinylated proteins. I eluted proteins from the beads and measured the amount of biotinylated protein in elute and load fractions on anti-GFP immunoblots (Fig. 5.34 C). ARP3-V5-TurboID samples biotinylated COR1C-GFP at 40x the levels of the COR1C ΔCC-GFP mutant or the GFP-Rab7 negative control (Fig. 5.3 and 5.4).

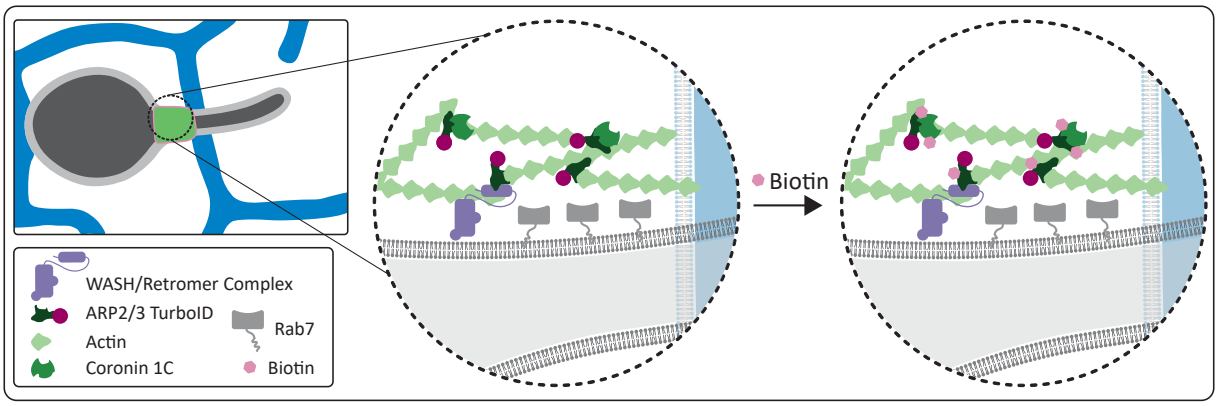

Figure 5.2: HeLa cells were co-transfected with ARP2/3-V5-TurboID and either GFP-Rab7, COR1C-GFP, or COR1C-ACT-ΔCC-GFP; treated with biotin, and then biotinylated proteins were bound and eluted from α-biotin beads.

To demonstrate that the biotinylation activity of ARP3-V5-TurboID was specific and could also biotinylate endogenous proteins I also repeated the experiments as detailed above with a nonspecific construct localized to the cytoplasm, Cyto-V5-TurboID. I co-transfected HeLa cells with either ARP3-V5-TurboID, or Cyto-V5-TurboID and either no additional exogenous bait (to probe for endogenous biotinylation), COR1C-GFP, or COR1C ACT-ΔCC-GFP (Fig. 5.5, 5.6,5.7, 5.8). When I probed elution fractions for COR1C I observed

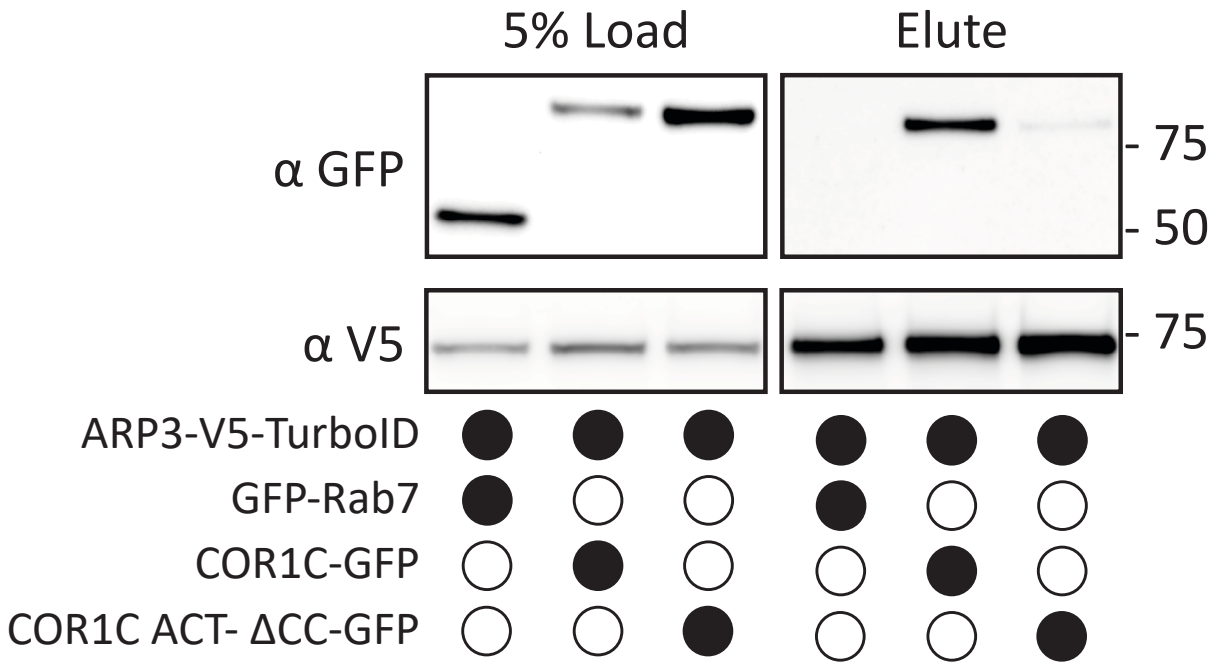

Figure 5.3: Representative V5 and GFP immunoblot from experiment in 5.2 shows high levels of biotinylation for full length COR1C compared to COR1C mutant or Rab7 control

that only ARP3-V5-Turbo-ID was able to biotinylate endogenous COR1C (Fig.5.5, 5.6). The specificity of the biotinylation was further supported when I compared the degree to which COR1C-GFP versus COR1C ACT- ΔCC-GFP were biotinylated by ARP3-V5-TurboID or Cyto-V5-TurboID (Fig S3 C and D). ARP3-V5-TurboID biotinylates COR1C-GFP to a much greater extent than COR1C ACT- ΔCC-GFP (Fig. 5.7,5.8, Fig. 5.2 5.3). This is in contrast with the nonspecific activity of Cyto-V5-TurboID which did not discriminate between COR1C-GFP and COR1C ACT- ΔCC-GFP constructs because both are equally accessible in the cytoplasm. These data suggest that the CC is required for ARP2/3 complex binding.

5.3 Discussion

In this chapter I demonstrate that limiting ARP2/3 complex activity via drug treatment is sufficient to reduce actin extension on the endosome bud. This indicates that the reason for actin extension in Type I coronin depletion is hyperactivity of the ARP2/3 complex. In support of this I show that the COR1C CC, which is necessary and sufficient to restore actin confinement, is a key component for tight proximity to the ARP2/3 complex. Taken together these data support a model where COR1C's CC is required for interaction with and regulation of ARP2/3 complex activity.

Although, the model I propose is well supported by my data it does not rule out alternate/indirect mechanisms of action.To definitively prove this it would be ideal to reconstitute branched actin polymerization by the ARP2/3 complex in the context of various purified COR1C mutants. This would enable more clear cut conclusions about both COR1C CC binding to the ARP2/3 complex and its effect on nucleation activity. This would also enable testing of exactly how nucleation is effected since numerous possibilities are plausible including the CC compromising ARP2/3 complex binding to actin or directly limiting nucleation activity.

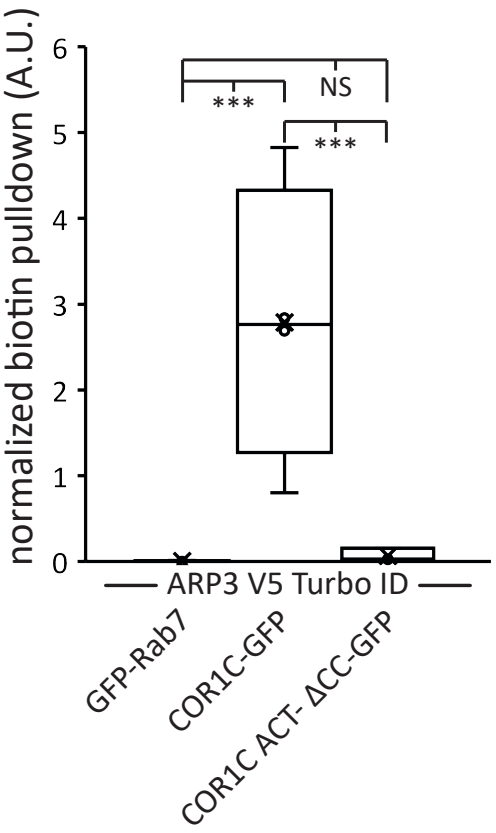

Figure 5.4: Quantification of immunoblot, as shown in 5.3. Pulldown numbers were calculated by normalizing elute signal with the load signal, performed in triplicate. Statistical analyses were performed with one-way ANOVA, p value from Tukey's test: ns = not significant, ***$p < 0.001$.

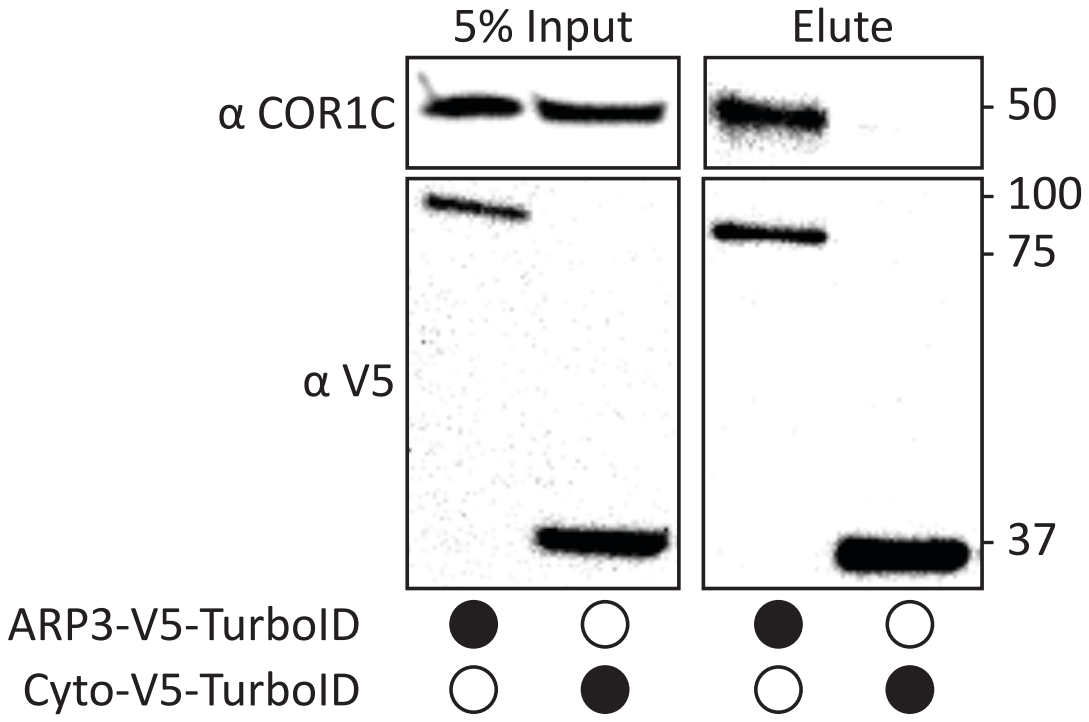

Figure 5.5: Representative immunoblot showing that ARP3 V5 TurboID and a cytoplasmic nonspecific TurboID is able to biotinylate endogenous COR1C. Blots show the same samples run twice to blot for either endogenous COR1C or V5. Performed in triplicate.

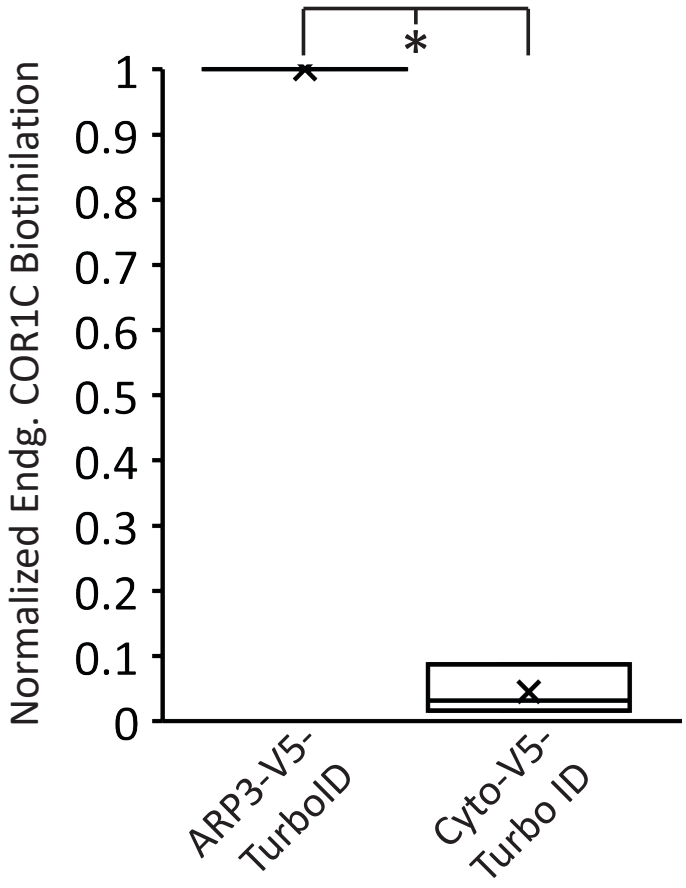

Figure 5.6: Quantification of blots in 5.5 showing the amount of COR1C signal in the elute normalized first to the relevant TurboID V5 signal in the input and then to the max value within each replicate

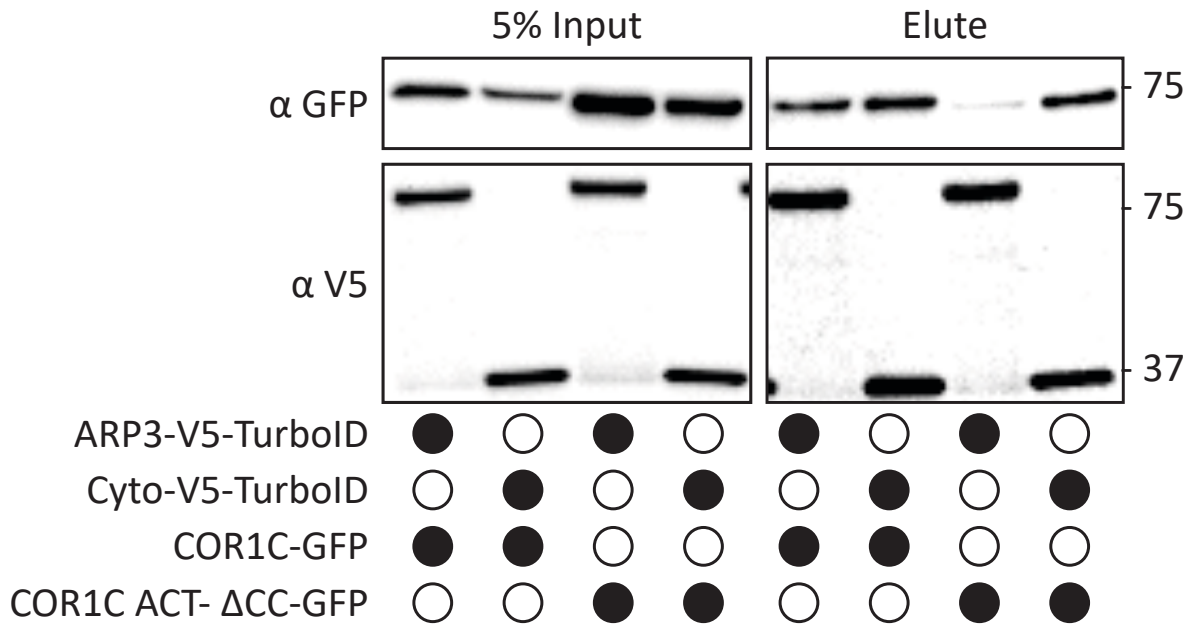

Figure 5.7: Representative immunoblot showing that ARP3 V5 Turbo has uniquely specific biotinylation of COR1C as shown by its ability to biotinylate only COR1C-GFP and not COR1C ACT- ΔCC-GFP. In contrast, the Cyto V5 TurboID biotinylates proteins nonspecifically in the cytoplasm as shown by similar biotinylation profiles for both COR1C-GFP and COR1C ACT- ΔCC-GFP. Performed in triplicate.

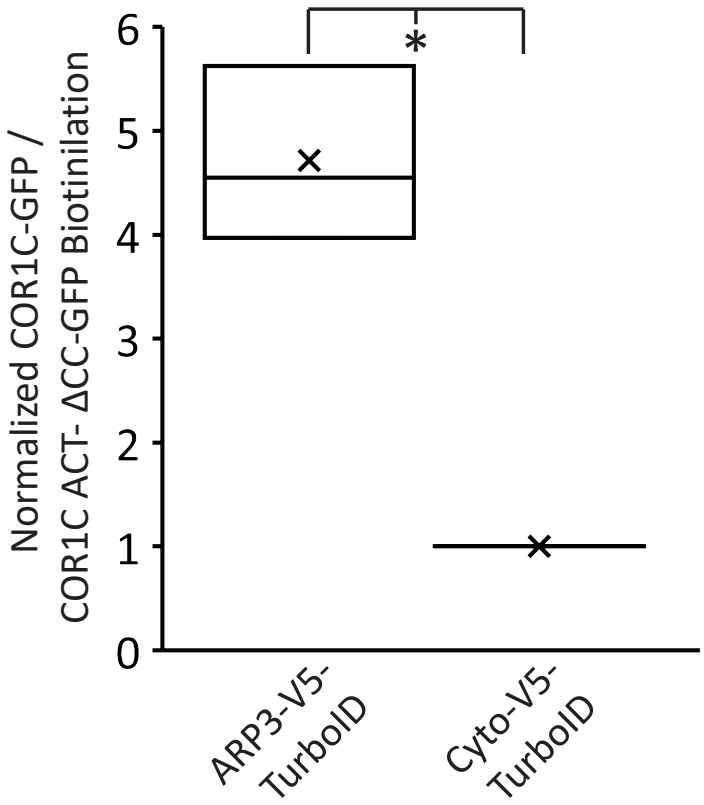

Figure 5.8: Quantification of blots in 5.7, from 3 replicates. Graph shows the ratio of COR1C-GFP to COR1C ACT- ΔCC-GFP signal in the elution. Signals in ratio were normalized to both relevant GFP and V5 input signals and then to the minimum value in each replicate. Statistical analysis was performed via two-tailed Student's t test, *p < 0.05. X indicates mean and line indicates median.

5.4 Methods

5.4.1 Plasmids and Reagents

α-actin-mNG and α-actin-Halo were generated by PCR amplification from actin Chromobody TagGFP (Chromotek, acg) and cloning into mNG-N1 or Halo-N1 via XhoI/KpnI sites. Primers used JS69 and JS70 (Table S1). V5 TurboID-N1 was generated by PCR amplification from V5-TurboID-NES which was a gift from Alice Ting (Addgene plasmid 107169) and cloning into ARP3-mNG via AgeI/NotI sites. Primers used JS106 and JS107 (Table S1).

5.4.2 Transfection

For imaging, COS-7 cells (ATCC tested for mycoplasma before delivery and freezing) were seeded on 35mm glass bottom dishes (Cellvis, D35-20-1.5-N) in DMEM (GIBCO, 12430-054) containing 10% FBS and 50 units/mL Penicillin, 50 μg/mL Streptomycin (Invitrogen, 15070063) for 16 h, then transfected with plasmids using Lipofectamine 3000 following manufacturer's protocol. Briefly, two separate 250 μL mixes were prepared with Opti-MEM (Invitrogen, 31985-088). One mix received plasmids intended for transfection and 2 μL P3000 reagent per μg of plasmid. The second mix received 5 μL Lipofectamine 3000. These mixes were combined after a 5 min room temperature incubation. This is followed by a 20 min room temperature incubation where upon the combined mix was added to the imaging dish dropwise. Prior to transfection mix addition, cells were rinsed once with 1x PBS and then placed in 1.5 ml Opti-MEM. Cells were incubated with transfection mix for 5 h and then rinsed once with 1x PBS and then placed in 2 ml DMEM. Cells were then imaged 16 h later in 1.5 ml FluoroBrite DMEM (GIBCO, Cat. A18967-01) containing 10% FBS, 25 mM HEPES, and 1x GlutaMAX (GIBCO, 35050061). Cells transfected with halo tag had 100nM Janelia Fluor 646 halo ligand, provided by Luke Lavis, added to the imaging media and were incubated with ligand for 30 min prior to imaging.

The following concentrations were used for each plasmid:25 ng/ml GFP-Rab7 (imaging and TurboID).COR1C-GFP (TurboID); 125 ng/ml COR1C ACT-ΔCC-GFP (TurboID);50 ng/ml α-actin-Halo;

5.4.3 Microscopy

Cells were imaged via a spinning disk confocal microscope or confocal line scanning microscope. The spinning disk confocal microscope consists of Nikon eclipse Ti2 inverted microscope body equipped with; PSF unit, Yokagowa CSU-X1 spinning disk confocal scanner; an Andor iXon 897 electron-multiplying charge-coupled device 512x512 camera; and OBIS 405, 488, 561, 640 nm lasers. Images were acquired with 100× 1.45-NA Plan Apo objective using Micro-Manager software and ImageJ (National Institutes of Health). For Fig. 1 D-I Airyscan LSM 880 was used all other images were acquired on spinning disk detailed above. The line scanning confocal consists of Zeiss Axio Observer inverted fluorescence microscope body equipped with LSM 880, and Airyscan detector. Images were acquired with 63× 1.4-NA Plan Apo objective Zeiss Zen Software.

5.4.4 Statistics

All data described are from at least three biological replicates. All data were graphed as box and whisker plots with median (indicated by line) and mean (indicated by X) shown. When comparing two samples, two-tailed Student's t tests were used. For comparisons across multiple samples significance testing was done by first establishing significant differences exist between conditions by one way ANOVA. If variation between conditions was significantly greater then with in conditions this was followed by post hoc significance testing with Tukey's Test. ns = not significant, *$p < 0.05$, **$p < 0.01$, ***$p < 0.001$. Analyses were all performed using GraphPad Prism 8. Details of significance calculations as well as n values for each quantification are reported in the relevant figure legends.

5.4.5 TurboID Proximity Labeling Analysis

Proximity labeling was adapted from (Wu and Voeltz, 2021). HeLa cells (ATCC, CCL-2, tested for mycoplasma before delivery and freezing) were transfected with ARP3-V5-TurboID and either GFP-Rab7, COR1C-GFP, COR1C ACT-ΔCC-GFP. 16 h post transfection, cells were incubated in 500 μM Biotin (Sigma Aldrich, B4501-500MG) for three hours followed by two 1x PBS washes to remove excess biotin. Cells were then trypsinized, pelleted, and the pellet was washed twice with ice cold 1x PBS. Cells were then lysed in 250 μL freshly made lysis buffer + PIC (50 mM Tris pH 7.5, 150mM NaCl, 10% glycerol, 1% NP-40 (for Cyto-V5-TurboID NP40 was replaced with TX-100 due to problems with availability), 1x Calbiochem protease inhibitor cocktail III EDTA free) nutating at 4°C for 1 h. Lysed cells were spun at 16,100 x g for 10 min at 4°C to pellet insoluble cell debris. 5% of the lysis volume was collected as "load" sample. The remaining sample was loaded on to biotin antibody agarose beads (Immunechem, ICP0615) and left nutating overnight at 4 °C. Bead bound samples were washed twice for 5 min on nutator at 4°C with cold high salt wash (50 mM Tris pH 7.5, 1M NaCl, 1mM EDTA, 1% NP40, 0.1% SDS, 0.5% Sodium Deoxycholate (Sawyer2019)) followed by 4x cold lysis buffer without PIC washes at 4C. Proteins were eluted off beads with 2x Laemmli sample buffer (with 355mM 2-mercaptoethanol) and run on 4-12% Criterion TGX gels. Using standard immunoblotting protocols V5 (turboID) and GFP (potential interactors) were blotted for. To quantify pulldown, elute and input signals were background subtracted using local background of the band and then elute signal was divided by input signal.

5.4.6 ARP2/3 Inhibition by CK-666 treatment.

COS-7 cells were prepared for imaging as detailed in the transfection protocol. Cells with extended actin structures were identified and imaged. Cells were treated with 150 μM CK-666 (Millipore Sigma, 182515-25MG) in order to ensure fast uniform ARP2/3 inhibition.

This was critical to ensure confidence in tracking the same endosome bud before and after drug treatment. Cells were imaged 30 sec post CK-666 addition.

5.5 Acknowledgements

I thank V. Olsen for assistance generating plasmids. I thank E. Sawyer, T. Nguyen, H. Wu, E. Zamponi, and V. Olsen for insight and helpful discussion. J.F. Striepen was supported by a graduate training grant in signaling and cellular regulation (NIH T32 GM008759). This work was also supported by a grant from the NIH to G.K. Voeltz. (GM120998). G.K. Voeltz. is an investigator of the Howard Hughes Medical Institute. I

Chapter 6

The COR1C CC is necessary and sufficient to rescue LE fission, cargo sorting, and ER contact in type I coronin depleted cells

6.1 Introduction

I show that Type 1 coronins function redundantly to confine actin to the endosome bud neck and that COR1C's CC was both necessary and sufficient to rescue actin confinement. I also link the COR1C CC to interaction with and regulation of ARP2/3 complex. To contextualize these results I next wanted to investigate the effect of actin extension on endosome fission and cargo recycling since these are the functions of the endosome bud structures. I showed previously that the upstream cargo sorting machinery as well as a model cargo are still enriched at the bud.

This lead us to hypothesize that the last steps of endosome recycling, ER recruitment and fission, were compromised when Type I coronins were depleted. Previous work indicated that COR1C depletion alone compromised ER recruitment and fission but whether this was a rescuable phenotype and whether cargo sorting was also effected was no measured Hoyer et al. [2018]. To test this I needed to establish a fission defect in Type I coronin depleted cells and then demonstrate that this defect was rescued by the same constructs that restored actin confinement. Then I could assess whether cargo sorting to the golgi and ER recruitment to the bud were also compromised when extended actin structures were present on the bud.

6.2 Results

6.2.1 The COR1C CC is necessary and sufficient to rescue LE fission and cargo sorting in type I coronin depleted cells.

I showed that actin extension into the distal bud does not disrupt the assembly of cargo sorting machinery components (Fig. 3.4). I hypothesized that although these components are present, actin must be confined to the bud neck for LE bud fission to occur. To test this hypothesis directly, I co-transfected COS-7 cells with COR1A/1B/1C siRNA to deplete all Type I coronins, GFP-Rab7 (LE), mCh-FAM21 (WASH complex), and either a Halo empty vector (E-vec) control, siRES COR1C-Halo, siRES COR1C ACT–Halo, siRES COR1C ΔCC-Halo, siRES COR1C ACT- ΔCC-Halo, or siRES COR1C CC-Halo. I collected two-minute time lapse movies at two second intervals and each FAM21 positive bud was scored for length, vacuole diameter, and fission (Fig. 6.4, 6.5and Fig. 6.3). There were no significant changes to either bud length or vacuole diameter (Fig. 6.4, 6.5). Rescue with an E-vec showed Type I coronin depletion results in a 3-fold reduction in fission rate (10 %, Fig. 6.1 and 6.3) Hoyer et al. [2018]. Reintroduction of full length COR1C was sufficient to rescue fission rate (39%, Fig. 6.2 and 6.3). The mutants which lack the CC domain did not restore fission rate above the E-vec control resulting in FAM21-labeled buds that were stable for the duration of the time-lapse (Fig. 6.1): COR1C ΔCC, COR1C ACT- ΔCC-Halo (12% and 15% vs. 11% respectively, Fig. 6.3). The COR1C CC proved both necessary and sufficient to rescue the FAM21-positive bud fission rate to comparable levels with WT rescue (Fig. 6.1 and 6.2).

Having established the importance of the COR1C CC for FAM21 marked bud fission I hypothesized that retrograde membrane cargo flow would be limited upon depletion of Type I coronins. To test this I measured recycling of the cation independent mannose six phosphate receptor (CI-M6PR) which relies on the WASH complex for retrograde transport to the Golgi Dong et al. [2016], Duleh and Welch [2010]. I co-transfected COS-7 cells with either COR1A/1B/1C siRNA, FAM21 siRNA (control), or CNTRL siRNA and GFP E-vec

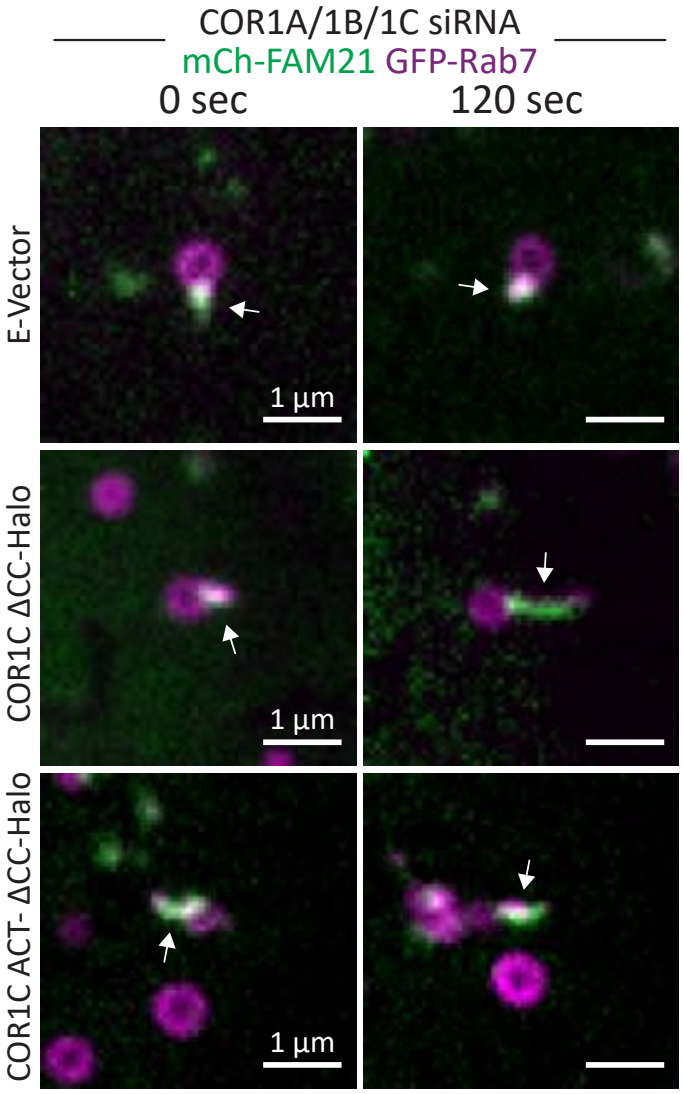

Figure 6.1: Representative images of LE buds stable for duration of acquisition in conditions that did not rescued fission rate (6.3). COS-7 cells were co-transfected with COR1A/1B/1C siRNA to deplete all Type I coronins and with GFP-Rab7 (LE, magenta), mCh-FAM21 (WASH complex, green), and either Halo E-vec, siRES COR1C ΔCC-Halo, siRES COR1C ACT- ΔCC-Halo. Arrows indicate bud of interest. Scale bars for whole cell = 5 μm; insets = 1 μm.

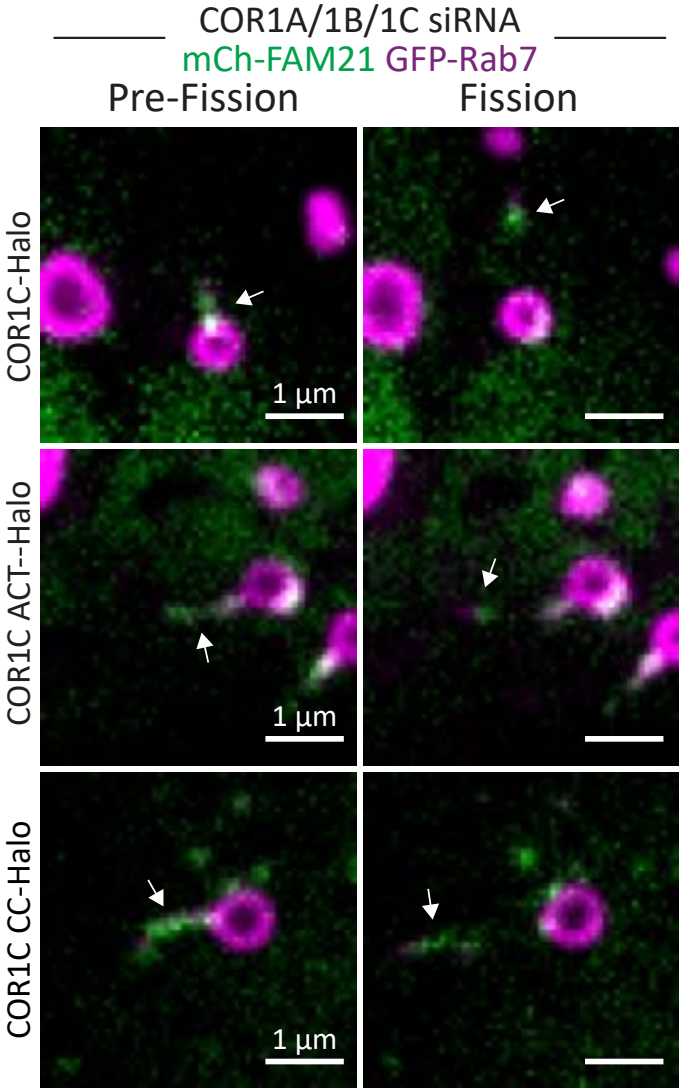

Figure 6.2: Representative images of LE fission events in conditions that rescued fission rate (6.3). COS-7 cells were co-transfected with COR1A/1B/1C siRNA to deplete all Type I coronins and with GFP-Rab7 (LE, magenta), mCh-FAM21 (WASH complex, green), and either siRES COR1C-Halo, siRES COR1C ACT–Halo, or siRES COR1C CC-Halo. Arrows indicate bud of interest. Scale bars for whole cell = 5 μm; insets = 1 μm.

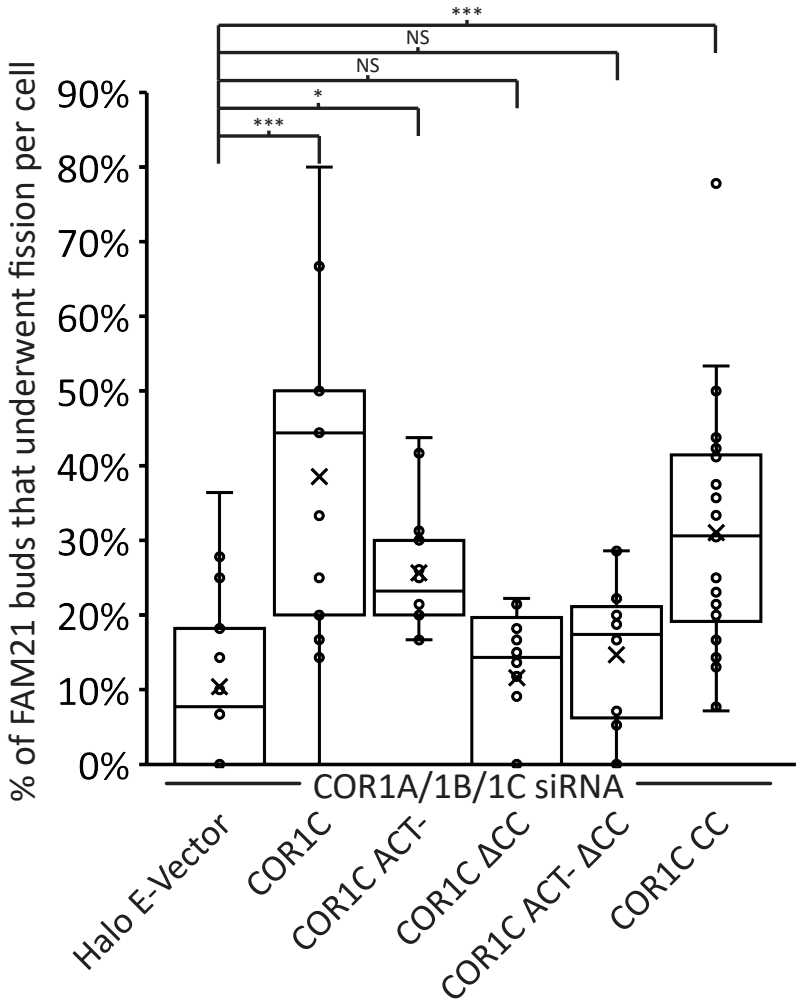

Figure 6.3: Quantification of data in 6.1 and 6.2. Graph shows percentage of FAM21-labeled LE buds that undergo fission per cell during a two-minute time lapse. Note that only constructs containing the CC are able to restore fission. Data for graph from: Halo E-vec: 139 endosomes in n = 15 cells; siRES COR1C: 122 endosomes in n = 15 cells; siRES COR1C ACT-: 213 endosomes in n = 17 cells; siRES COR1C ΔCC: 281endosomes in n = 18 cells; siRES COR1C ACT- ΔCC: 296 endosomes n = 17 cells; and siRES COR1C CC: 331 endosomes in n = 22 cells, performed in triplicate. X indicates mean and line indicates median. Statistical analyses were performed with one-way ANOVA, p value from Tukey's test: ns = not significant, *p < 0.05, ***p < 0.001. Scale bars for whole cell = 5 μm; insets = 1 μm.

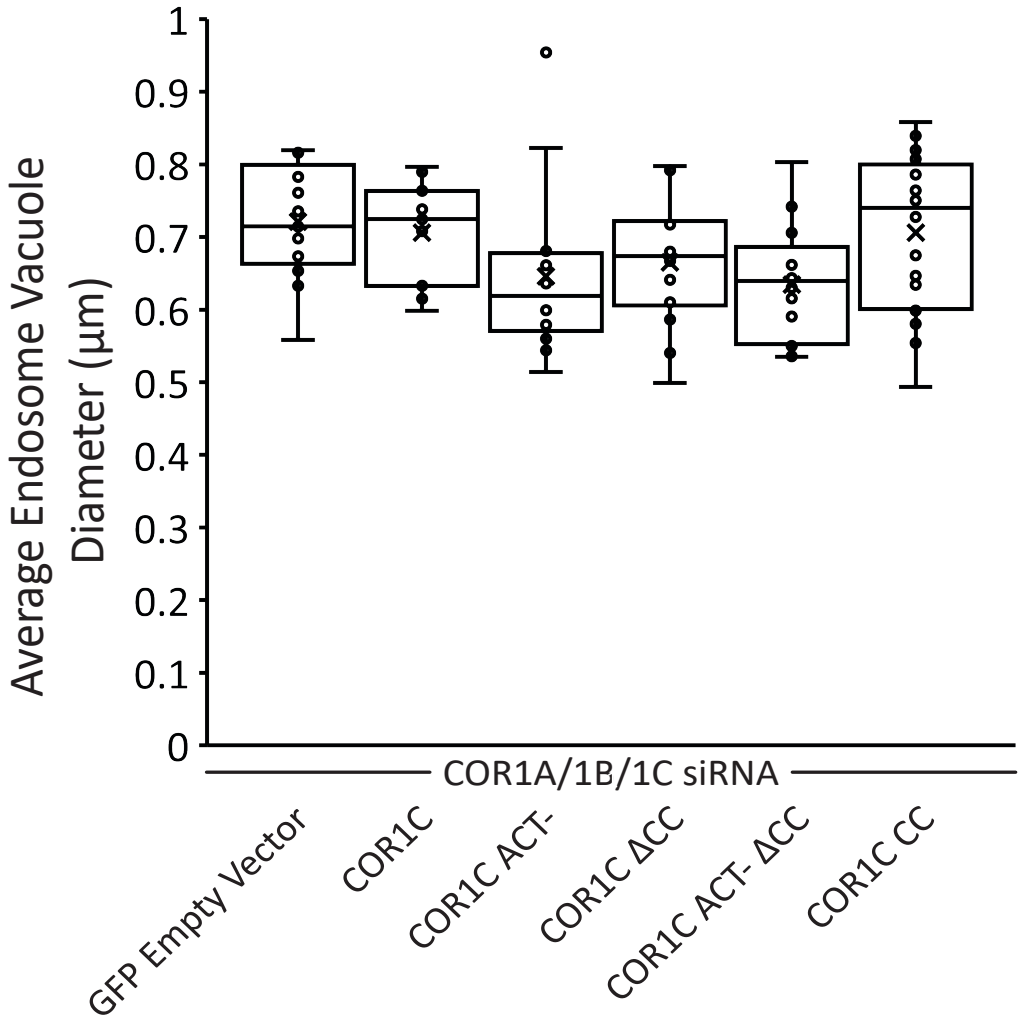

Figure 6.4: For each bud scored for fission in Fig. 6.3 vacuole diameter was also measured. Graph shows average vacuole diameter per cell, averaged per condition. No significant changes were observed in any condition showing that only fission is affected and not other measures of endosome morphology. Data for graph from: Halo E-vec: 139 endosomes in n = 15 cells; COR1C: 122 endosomes in n = 15 cells; COR1C ACT-: 213 endosomes in n = 17 cells; COR1C ΔCC: 281endosomes in n = 18 cells; COR1C ACT- ΔCC: 296 endosomes n = 17 cells; and COR1C CC: 331 endosomes in n = 22 cells. X indicates mean and line indicates median. Statistical analyses were performed with one-way ANOVA.

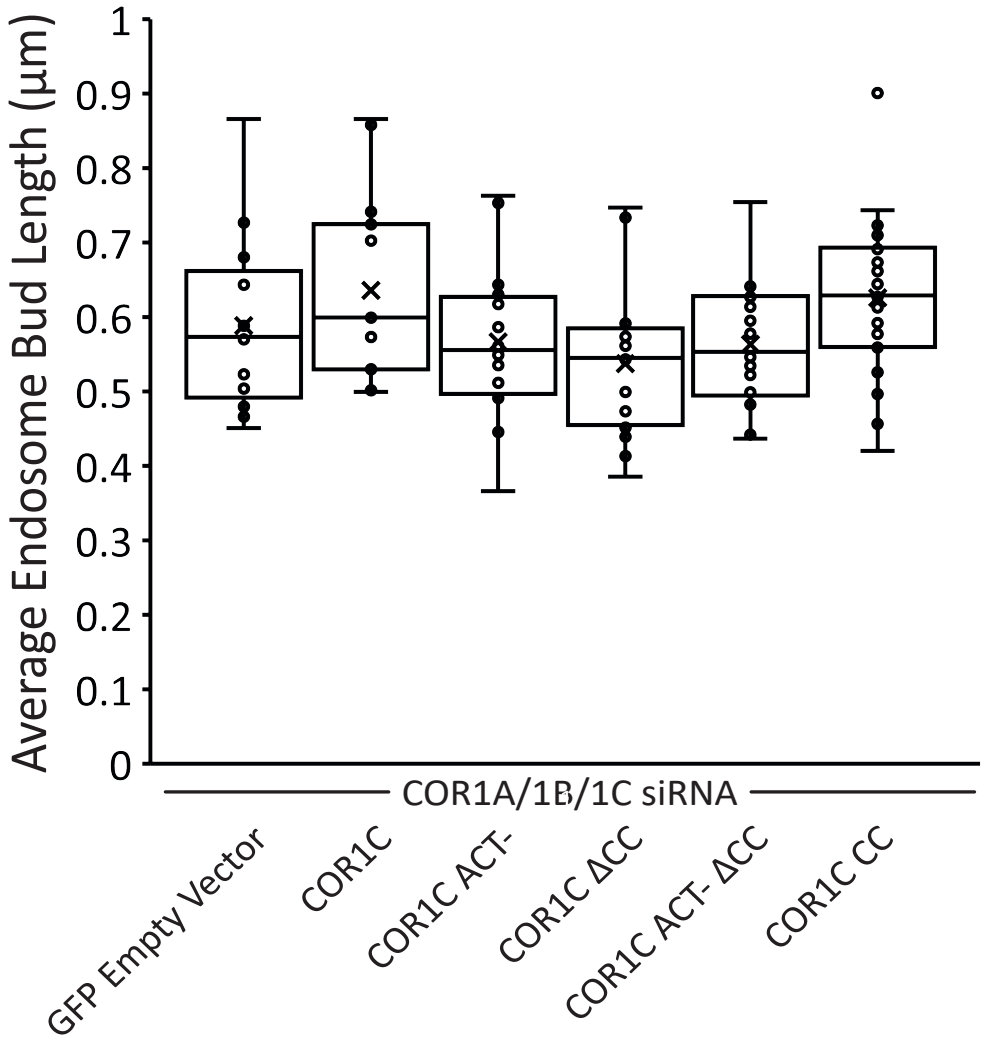

Figure 6.5: As in 6.4, except FAM21 positive bud length was measured instead of vacuole diameter. Again, no significant changes were observed in any condition showing that only fission is affected and not other measures of endosome morphology. Data for graph from: Halo E-vec: 139 endosomes in n = 15 cells; COR1C: 122 endosomes in n = 15 cells; COR1C ACT-: 213 endosomes in n = 17 cells; COR1C ΔCC: 281endosomes in n = 18 cells; COR1C ACT- ΔCC: 296 endosomes n = 17 cells; and COR1C CC: 331 endosomes in n = 22 cells. X indicates mean and line indicates median. Statistical analyses were performed with one-way ANOVA.

(control) (Fig. 6.8). These cells were then treated with CI-M6PR antibody for one hour before they were rinsed to remove unbound antibody and fixed. Using immunofluorescence I probed the intracellular distribution of CI-M6PR signal relative to the Golgi in these fixed cells (Fig. 6.6). I observed that in both the FAM21 and Type I coronin depletions CI-M6PR signal failed to accumulate at the Golgi as in the CNTRL siRNA treated cells, instead remaining trapped in vesicles distributed broadly across the cytoplasm (Fig. 6.6 and 6.7). I hypothesized that as with fission the COR1C CC would be both necessary and sufficient to rescue retrograde sorting of CI-M6PR. To test this, I co-transfected COS-7 cells with COR1A/1B/1C siRNA, and either siRES COR1C-GFP, siRES COR1C ΔCC-GFP, or siRES COR1C CC-GFP. As before, cells were treated with CI-M6PR antibody for an hour, fixed, and stained to measure retrograde recycling efficiency (Fig. 6.6). Reintroduction of either COR1C-GFP and COR1C CC-GFP were sufficient to restore retrograde recycling to a similar degree as CNTRL siRNA treated cells (Fig. 6.7). In contrast, reintroduction of COR1C ΔCC-GFP was unable to rescue retrograde sorting of CI-M6PR (Fig. 6.6 and 6.7). As with fission the COR1C CC proved both necessary and sufficient to restore efficient retrograde recycling of CI-M6PR.

6.2.2 The COR1C CC limits bud actin to facilitate ER contact.

I have shown that Type I coronin depletion results in extended actin on the buds, a reduction in endosome fission rate, and reduced retrograde recycling of the CI-M6PR2. Endosome fission at WASH complex marked buds is regulated by MCSs with ER tubules Rowland et al. [2014], Hoyer et al. [2018], Allison et al. [2013, 2017], Dong et al. [2016]. Thus, I hypothesized that Type I coronin depletion and actin extension might impede the formation of ER-endosome MCSs between ER tubules and the endosome bud. To test this, I imaged the ER and endosomes in live cells depleted of all Type I coronins. I co-transfected COS-7 cells with COR1A/1B/1C siRNA, BFP-Sec61B (ER marker), GFP-Rab7 (LEs), mCh-FAM21 (WASH complex), and either a Halo E-vec (control) or siRNA-resistant COR1C-Halo (Fig.

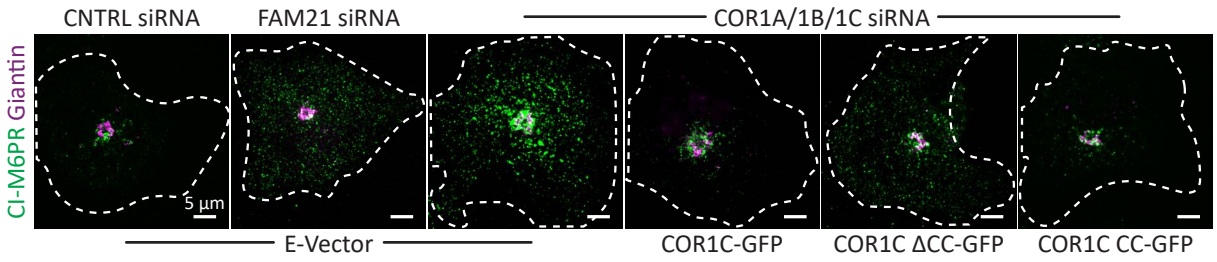

Figure 6.6: Representative images of the M6PR trafficking assay. The relative fluorescence intensity of internalized anti-CI-MPR antibody immuno-staining reveals trafficking of internalized anti-CI-MPR to TGN in Cos7 cells co-transfected with either CNTRL siRNA, COR1A/1B/1C siRNA to deplete all Type I coronins, or FAM21 siRNA, and either GFP E-vec, siRES COR1C-GFP, or siRES COR1C ΔCC-GFP (not shown). Cells were stained to mark CI-M6PR (green) and Giantin (Golgi, magenta). Dispersed vesicular CI-M6PR signal is indicative of failure to recycle whereas concentrated CI-M6PR signal at the Golgi indicates normal retrograde sorting. Scale bars for whole cell = 5 μm

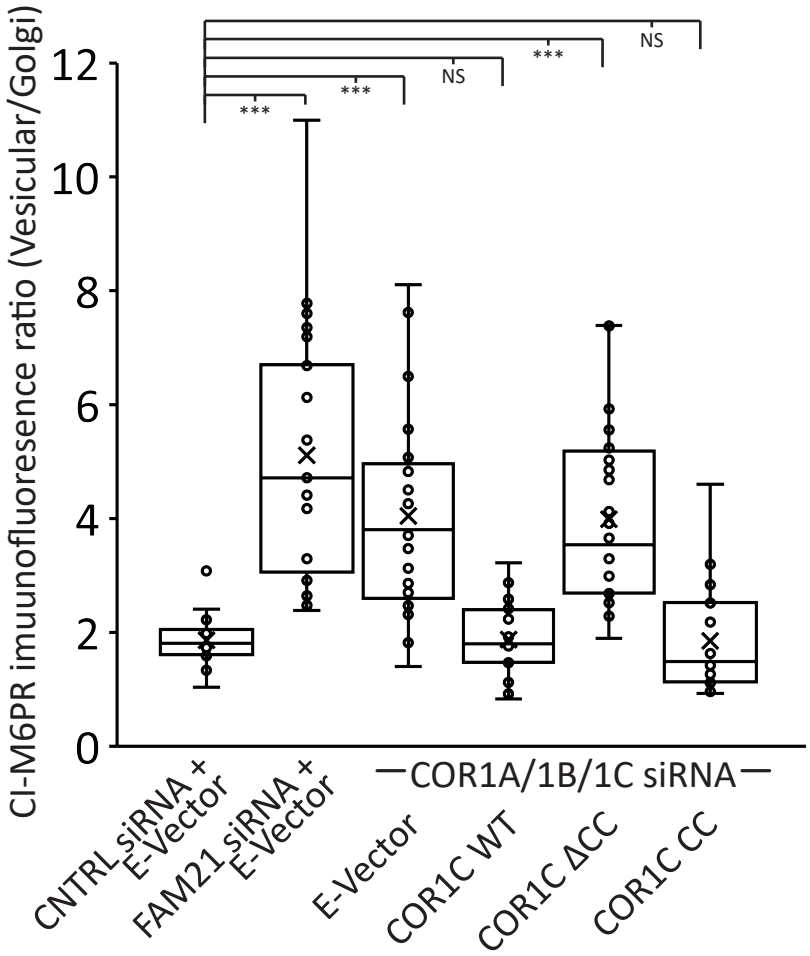

Figure 6.7: Quantification of data in 6.6. Graph shows the background corrected ratio of CI-M6PR signal localized at the Golgi relative to the vesicular signal in the cytoplasm such that larger values indicate less efficient retrograde recycling. Data for graph from: CNTRL siRNA: n = 24 cells; FAM21 siRNA: n = 23 cells; COR1A/1B/1C siRNA + E-vec: n = 25; COR1A/1B/1C siRNA + siRES COR1C: n = 24 cells; COR1A/1B/1C siRNA + siRES COR1C ΔCC: n = 24 cells; COR1A/1B/1C siRNA + siRES COR1C CC: n = 26 cells, performed in triplicate. Statistical analyses were performed with one-way ANOVA, p value from Tukey's test: ns = not significant, *$p < 0.05$, ***$p < 0.001$.

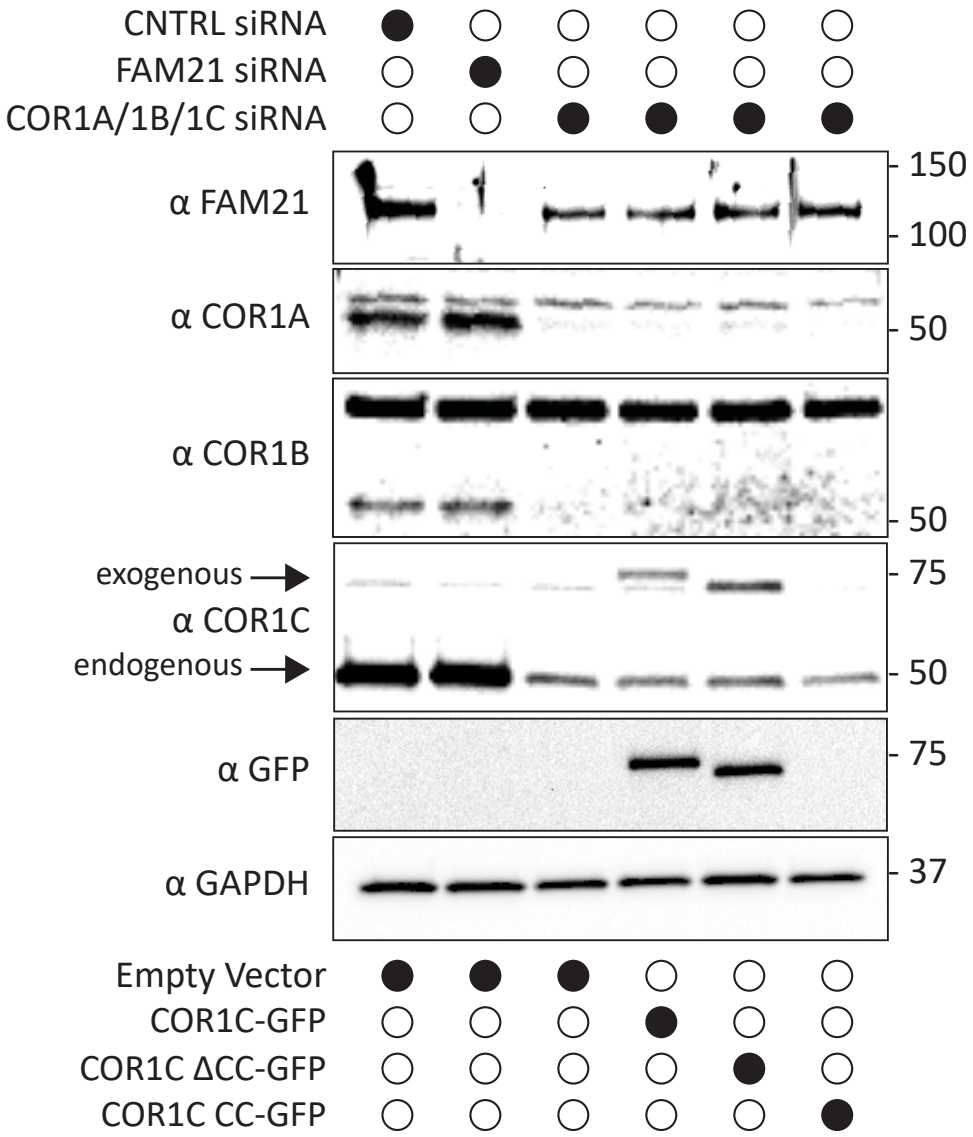

Figure 6.8: Immunoblots probed with antibodies indicated show efficient depletion of COR1A/1B/1C or FAM21 for experiments performed in Fig. 6.6 and 6.7. Blots were also probed for GFP to show exogenous rescue expression and GAPDH as loading control.

6.9). I imaged cells for two minutes at a two second interval. I scored the percent of frames (during the two-minute time lapse) that the ER tubules tracked with the FAM21 positive endosome buds. This allowed us to calculate a percent contact per endosome bud which was averaged per cell (Fig. 6.10). The data revealed a clear impairment of ER contact with the FAM21 marked endosome buds in the E-vec control (40%) when compared with the WT rescue (86%) (Fig. 6.10). This supports the idea that the extended actin structures on endosome buds hinder proper contact site formation. Interestingly, the vacuole ER MCS remained largely unchanged as can be seen in the line scans along the vacuole and bud where the first ER peak corresponds to the vacuole MCS (Fig. 6.9). This suggests that Type I coronin depletion does not generally inhibit ER-endosome MCS formation, but specifically compromises the bud MCS.

Since the COR1C CC domain is necessary and sufficient to rescue actin clearance from the distal bud and LE fission, I investigated if it could also rescue ER contact with FAM21-labelled buds. As before, I co-transfected COS-7 cells with COR1A/1B/1C siRNA to deplete all three Type I coronins, BFP-Sec61B (ER), GFP-Rab7 (LE), mCh-FAM21 (WASH complex), and reintroduced either siRNA-resistant: siRES COR1C ACT–Halo, siRES COR1C ΔCC-Halo, siRES COR1C ACT- ΔCC-Halo, or siRES COR1C CC-Halo. I scored ER contact with FAM21 positive endosome buds in two-minute time-lapse movies as before (Fig. 6.9). The COR1C CC proved to be both necessary and sufficient to rescue ER tubule contact with the FAM21-labelled endosome bud. In cells rescued with mutants lacking the CC, ER contact was not restored to levels significantly different from the E-vec control (Fig. 6.10; E-Vector 40%, ΔCC 36%, ACT-ΔCC 43%). Cells rescued with the COR1C ACT- or COR1C CC constructs showed restored ER-LE bud MCSs (81% and 80%, respectively) to the same degree as WT rescue (86%) (Fig. 6.10). Taken together, these results support the model where the COR1C CC domain functions to restrict ARP2/3-mediated actin nucleation on the endosome bud to allow ER MCS formation during ER-associated endosome fission (Fig. 7.1).

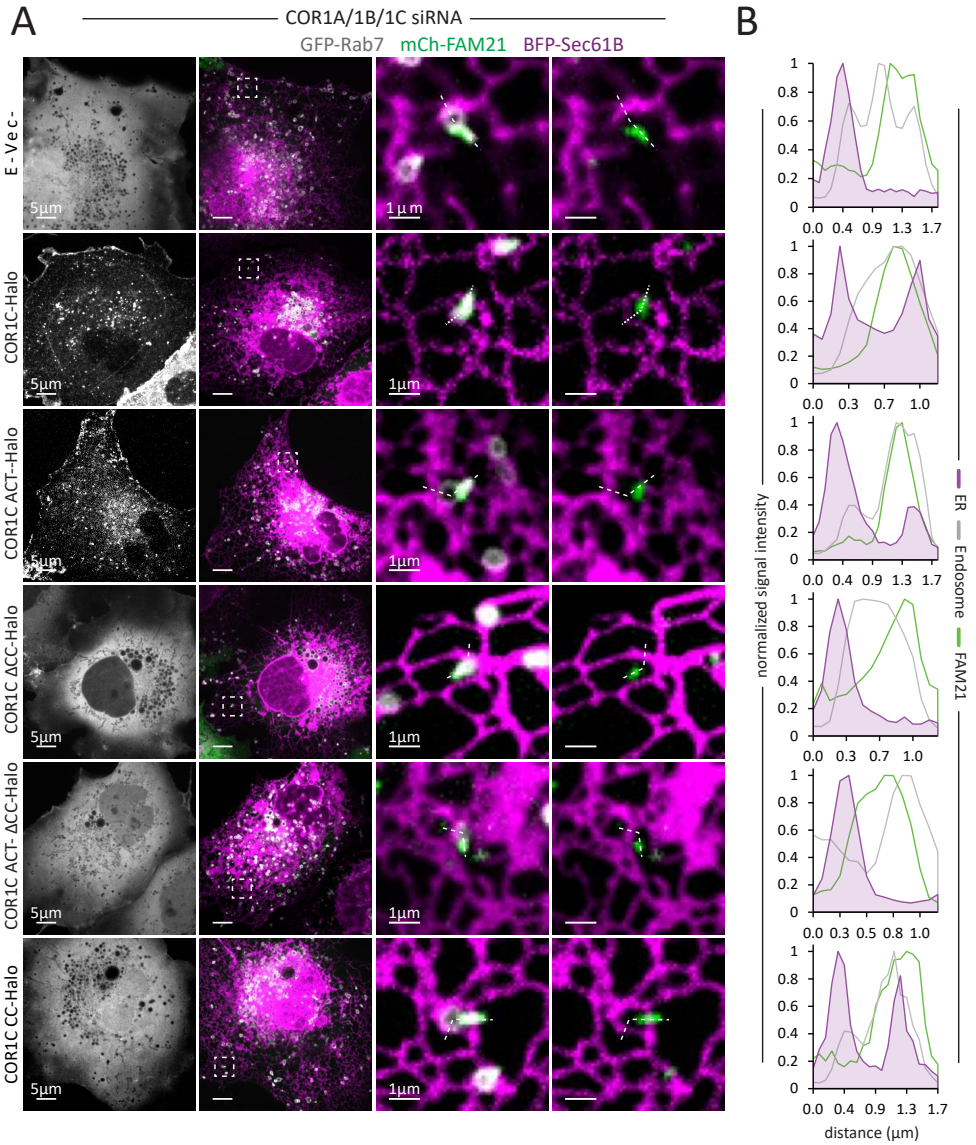

Figure 6.9: (A) Representative images of COS-7 cells co-transfected with COR1A/1B/1C siRNA to deplete all Type I coronins and with GFP-Rab7 (LE, gray), mCh-FAM21 (WASH complex, green), BFP-Sec61 (ER, magenta) and either Halo E-vec, siRES COR1C-Halo, siRES COR1C ACT–Halo, siRES COR1C ΔCC-Halo, siRES COR1C ACT- ΔCC-Halo, or siRES COR1C CC-Halo (gray, left panel). Magnified inset (5 x 5 μm) on right show representative examples of ER contact with endosomes. Note: Vacuolar contact with ER is always preserved, whereas, ER contact with the FAM21 labeled bud is not. Scale bars for whole cell = 5 μm; insets = 1 μm.

(B) Line scan analysis of dashed lines shown in (D are positioned from the rear vacuolar contact across the length of the FAM21 labeled buds. Double ER peaks (shaded purple) are observed when bud contact is rescued. The first peak is always present and corresponds to the vacuolar contact. The second ER peak which aligns with the FAM21 indicates proper ER recruitment to the bud. Note that ER contact with bud is dependent on the presence of the CC domain.

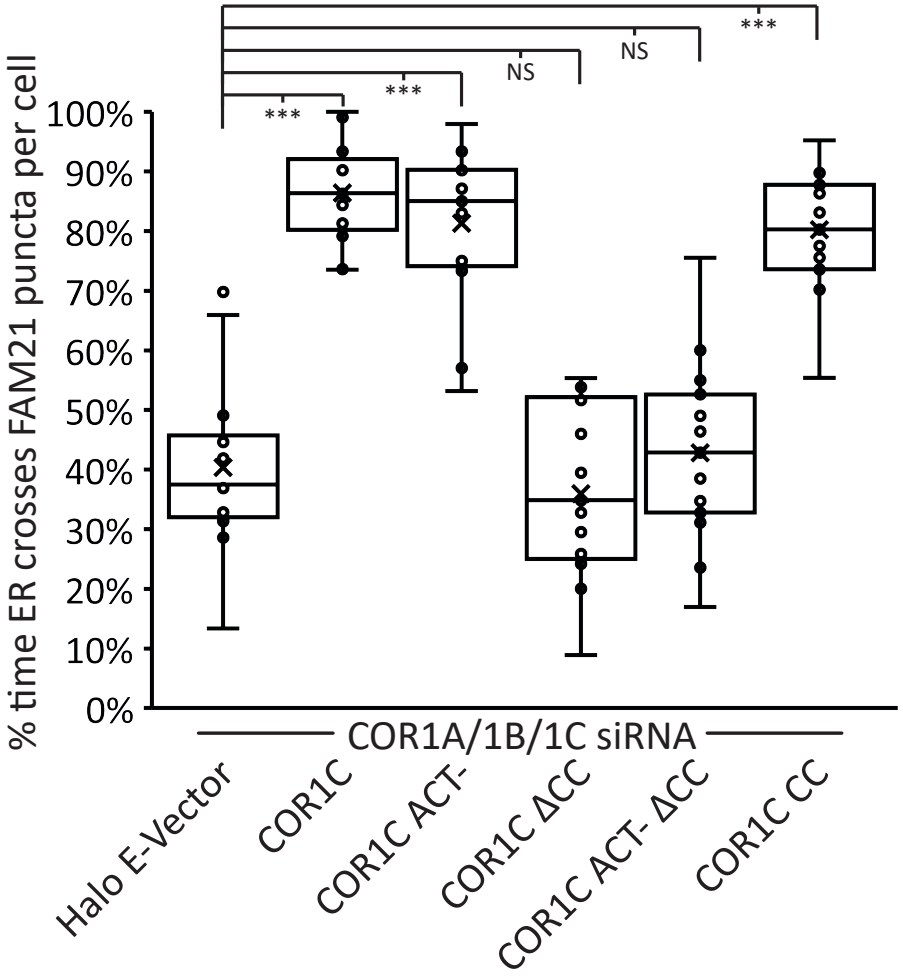

Figure 6.10: Quantification of data in 6.9. All FAM21 positive LE buds in areas with resolvable ER were tracked and ER contact was scored as the percent of time during a 2 min movie that contact is maintained. Data for graph from: Halo E-vec: 109 endosomes in n = 14 cells; COR1C: 134 endosomes in n = 17 cells; COR1C ACT-: 135 endosomes in n = 17 cells; COR1C ΔCC: 123 endosomes n = 17 cells; COR1C ACT- ΔCC: 105 endosomes in n = 15 cells; or COR1C CC: 137 endosomes in n = 19 cells, performed in triplicate. X indicates mean and line indicates median. Statistical analyses were performed with one-way ANOVA, p value from Tukey's test: ns = not significant, *$p < 0.05$, ***$p < 0.001$.

6.3 Discussion

Here I connect the miss-regulation of actin at the endosome bud when Type I coronins are depleted to functional downstream consequences. I show that in this context the ER is no longer efficiently recruited to from a MCS with the endosome bud, causing a decrease in the rate of endosome fission, and subsequent loss of efficient retrograde cargo recycling. I propose that the actin structure defines the part of the endosome bud that is fission competent by dictating where the ER is able to form MCS. This model represents a new paradigm in the interplay between the cytoskeleton and ER MCS as it has not been previously shown that the formation of MCSs can be influenced by actin polymerization.

Work from previous lab members identified COR1C as important for ER recruitment and fission which fits nicely with the results I detail here Hoyer et al. [2018]. Given those previous results it was initially puzzling to us that COR1C depletion alone did not have a measurable impact on actin at the endosome bud and I had to deplete COR1A and 1B to see a clear phenotype. However, these structures are well below the resolution limit of my light microscopes and are incredibly dynamic. It is very possible that fission and ER contact are more sensitive readouts of this structure and that there are changes to the actin structure that I are unable to measure given my current technical constraints. This would be another compelling reason to establish an in vitro system for studying the interplay of these proteins.

6.4 Methods

6.4.1 Plasmids and Reagents

GFP-Rab7 and mCh-Rab7 were gifts from P. Chitwood and were described previously (Rowland et al., 2014). Human Rab7 was PCR amplified from human cDNA and cloned into AcGFP/mCherry-C1 with XhoI/HindIII sites. Halo-Rab7 was generated by first PCR amplifying the Halo tag and cloning into AcGFP-C1 via AgeI/SacI sites to generate AcHalo-C1. Primers were JS75 and JS76 (Table S1). Rab7 was PCR amplified from mCh-Rab7 and

cloned into AcHalo-C1 via HindIII/KpnI sites. Primers used were JS73 and JS74 (Table S1). COR1C-GFP was gift from Dr. Manojkumar Puthenveedu and Dr. Mark von Zastrow (Puthenveedu et al., 2010). SiRes COR1C-Halo was generated mutating COR1C-GFP by four rounds of site directed mutagenesis to remove siRNA binding to generate siRES COR1C-GFP which was subcloned into Halo-N1 via EcoRI/BamHI to generate siRES COR1C-Halo. SiRES COR1C ACT–Halo was generated by four rounds of site directed mutagenesis of COR1C-GFP to generate COR1C ACT-GFP. Primers used JS29-JS32 and JS34-JS37 (Table S1). COR1C ACT–GFP was then mutated by four rounds of site directed mutagenesis to remove siRNA binding to generate siRES COR1C ACT–GFP which was subcloned into Halo-N1 via EcoRI/BamHI to generate siRES COR1C ACT–Halo. Primers used JS41-JS48 (Table S1). SiRES COR1C ΔCC -Halo was generated by PCR amplification of COR1C-GFP to generate COR1C ΔCC-GFP. Primers used JS19 and JS108 (Table S1). COR1C ΔCC-GFP was then mutated by four rounds of site directed mutagenesis to remove siRNA binding to generate siRES COR1C ΔCC-GFP which was subcloned into Halo-N1 via EcoRI/BamHI to generate siRES COR1C ΔCC -Halo. Primers used JS41-JS48 (Table S1). SiRES COR1C ACT-ΔCC-Halo was generated by four rounds of site directed mutagenesis of COR1C ΔCC-GFP to generate COR1C ACT-ΔCC-GFP. Primers used JS29-JS32 and JS34-JS37 (Table S1). COR1C ACT-ΔCC-GFP was then mutated by four rounds of site directed mutagenesis to remove siRNA binding to generate siRES COR1C ACT-ΔCC-GPF which was subcloned into Halo-N1 via EcoRI/BamHI to generate siRES COR1C ACT-ΔCC-Halo. Primers used JS41-JS48 (Table S1). COR1C CC-Halo was generated by PCR amplified from COR1C-GFP and then cloned into Halo-N1 via HindIII/KpnI sites. Primers used JS109 and JS110 (Table S1). mCh-FAM21 was described previously (Rowland et al., 2014). Briefly, it was subcloned from shFAM21/HA-YFP-FAM21 which came as a gift from Dr. Daniel Billadeau.

Rabbit COR1C polyclonal antibody (Proteintech, 14749-1-AP) was used at 1:2000 for immunoblotting. Rabbit COR1B polyclonal antibody (Abcam, ab119714) 1:2000 for immunoblotting. Rabbit COR1A polyclonal antibody (Abcam, ab123574) 1:2000 for im-

Primer Name	Sequence (5' to 3')
JS19	CCGGCTCGAGATGAGGCGAGTGGTACGACAGAG
JS29	GACCAGTGCTATGATGACATCGACGTTTCTCGTGTGACCTGG
JS30	CCAGGTCACACGAGAAACGTCGATGTCATCATAGCACTGGTC
JS31	CCTGATCAGCATCCCCGAGAAAACCACAGACACGG
JS32	CCGTGTCTGTGGTTTTCTCGGGGATGCTGATCAGG
JS34	CTGATCAGCATCCCCGAGGAAACCACAGACACGGCCAGT
JS35	ACTGGCCGTGTCTGTGGTTTCCTCGGGGATGCTGATCAG
JS36	CAAGCCCACTGCAAACGAGGAGTGCGACCTGATCAGC
JS37	GCTGATCAGGTCGCACTCCTCGTTTGCAGTGGGCTTG
JS41	CCTTGTCCTCCCTCTGCATAAAACCGGGCGCATCGACAAATCTTACCCTAC
JS42	GTAGGGTAAGATTTGTCGATGCGCCCGGTTTTATGCAGAGGGAGGACAAGG
JS43	CTATAAAAGACACAATCTGCAACCAGGACGAACGGATCTCCAAGTTAGAACAGCAGATG
JS44	CATCTGCTGTTCTAACTTGGAGATCCGTTCGTCCTGGTTGCAGATTGTGTCTTTTATAG
JS45	CGAGTGGTACGACAGAGTAAATTCCGCCACGTGTTTGGGCAAGCGGTG
JS46	CACCGCTTGCCCAAACACGTGGCGGAATTTACTCTGTCGTACCACTCG
JS47	GCACGGGTACATTCCAGGCAAAAATAGAGACCTGAAAGTCGTCAAGAAGAACATTCTGG
JS48	CCAGAATGTTCTTCTTGACGACTTTCAGGTCTCTATTTTTGCCTGGAATGTACCCGTGC
JS69	CATGACTCGAGATGGCTCAGGTGCAGCTGG
JS70	CATGGGTACCGGAGAACCTCCTCCACCGCTACC
JS73	CATGAAAGCTTCCATGACCTCTAGGAAGAAAGTGTTGCTGAAGG
JS74	TGATCGGTACCTCAGCAACTGCAGCTTTCTGCCG
JS75	CATGACCGGTATGGCAGAAATCGGTACTGGCTTTCC
JS76	CCAGGAGCTCCGCCGGAAATCTCGAGCGTCG
JS106	CATGACACCGGTCGGCAAGCCCATCCCCAACC
JS107	CTGGTCGCGGCCGCTCACTGCAGCTTTTCGGCAGACC
JS108	AATCGGATCCCGAATCTCATCCAACTTGGCTTCATTTTGCAC
JS109	CCGGaagcttATGACTGCAAACAAGAAGTGCGACC
JS110	GCCGGGGTACCGGGGCTGCTATCTTTGCCATCTGCTG

Table 6.1: Table of primers used for plasmid construction.

munoblotting. Mouse GFP monoclonal antibody (Clontech Labs 3P Living Colors® A.v. Monoclonal Antibody (JL-8), Fisher Scientific, NC9777966) was used at 1:2000 for immunoblotting. Rabbit FAM21C polyclonal antibody (Millipre, ABT79, Lot 3560681) was used at 1:1000 for immunoblotting. Rabbit GAPDH antibody (MilliporeSigma, G9545) was used at 1: 100000 for immunoblotting. Mouse IGFR2 (CI-M6PR) monoclonal antibody (Invitrogen, MA1-066) was used at 1:1000 for immunofluorescence. Rabbit Giantin antibody (BioLegend, PRB-114C) was used at 1:500 for immunofluorescence. Anti-Rabbit IgG (whole molecule)-Peroxidase antibody produced in goat (Sigma, A6154) was used at 1:6000 for immunoblotting. Anti-Mouse IgG (whole molecule)-Peroxidase antibody produced in goat (Sigma, A4416) was used at 1:3000 for immunoblotting. Goat anti-Rabbit IgG (H+L) Cross-Adsorbed Secondary Antibody, Alexa Fluor 405 (Thermo Fisher Scientific Cat A-31556) was used at 1:300 for immunofluorescence. Donkey. Donkey Anti-Mouse IgG (H+L) Antibody, Alexa Fluor 594 Conjugated (Thermo Fisher Scientific Cat A-21203) was used at 1:300 for immunofluorescence.

6.4.2 Transfection

For imaging, COS-7 cells (ATCC tested for mycoplasma before delivery and freezing) were seeded on 35mm glass bottom dishes (Cellvis, D35-20-1.5-N) in DMEM (GIBCO, 12430-054) containing 10% FBS and 50 units/mL Penicillin, 50 μg/mL Streptomycin (Invitrogen, 15070063) for 16 h, then transfected with plasmids using Lipofectamine 3000 following manufacturer's protocol. Briefly, two separate 250 μL mixes were prepared with Opti-MEM (Invitrogen, 31985-088). One mix received plasmids intended for transfection and 2 μL P3000 reagent per μg of plasmid. The second mix received 5 μL Lipofectamine 3000. These mixes were combined after a 5 min room temperature incubation. This is followed by a 20 min room temperature incubation where upon the combined mix was added to the imaging dish dropwise. Prior to transfection mix addition, cells were rinsed once with 1x PBS and then placed in 1.5 ml Opti-MEM. Cells were incubated with transfection mix for 5 h and

then rinsed once with 1x PBS and then placed in 2 ml DMEM. Cells were then imaged 16 h later in 1.5 ml FluoroBrite DMEM (GIBCO, Cat. A18967-01) containing 10% FBS, 25 mM HEPES, and 1x GlutaMAX (GIBCO, 35050061). Cells transfected with halo tag had 100nM Janelia Fluor 646 halo ligand, provided by Luke Lavis, added to the imaging media and were incubated with ligand for 30 min prior to imaging.

The following concentrations were used for each plasmid: 25 ng/ml mCh-Rab7; 25 ng/ml GFP-Rab7 (imaging and TurboID); 25 ng/ml Halo-Rab7; 25 ng/ml COR1C-Halo; 50 ng/ml siRES COR1C-GFP (CI-M6PR Rescue); 50 ng/ml SiRES COR1C-Halo (Rescue); 50 ng/ml SiRES COR1C ACT–Halo (Rescue); 75 ng/ml SiRES COR1C ΔCC-Halo (Rescue); 75 ng/ml siRES COR1C ΔCC-GFP (CI-M6PR Rescue); 75 ng/ml SiRES COR1C ACT-ΔCC-Halo (Rescue); 50 ng/ml SiRES COR1C CC-Halo (Rescue); 225 ng/ml BFP Sec61; 250 ng/ml mCh-FAM21.

6.4.3 Knockdown with siRNA

Cells were seeded in 2ml wells, as described previously, for 16 h. Cells were then transfected with siRNA at concentrations listed below with DharmaFECT 1 transfection reagent in DMEM containing 10% FBS for 6 h. Cells were allowed to recover for 40 h before transfecting with same amount of siRNA and plasmids marking structures of interest as described previously. After transfection cells were split into imaging dish and 2ml for KD confirmation via western.

Cells were transfected with 25nM negative control siRNA (single KD) or 75nM negative control siRNA (Type I coronin KD) (Ambion AM4635) or 25nM siRNA against COR1C (Dharmacon ON-TARGETplus SMARTPool L-017331-00-0010), 25nM siRNA against COR1A (Dharmacon ON-TARGETplus SMARTPool L-012771-00-0010), 25nM siRNA against COR1B (Dharmacon ON-TARGETplus SMARTPool L-010493-01-0010) 25nM siRNA against FAM21 (Dharmacon ON-TARGETplus SMARTPool L-029678-01-0005).

6.4.4 Microscopy

Cells were imaged via a spinning disk confocal microscope or confocal line scanning microscope. The spinning disk confocal microscope consists of Nikon eclipse Ti2 inverted microscope body equipped with; PSF unit, Yokagowa CSU-X1 spinning disk confocal scanner; an Andor iXon 897 electron-multiplying charge-coupled device 512x512 camera; and OBIS 405, 488, 561, 640 nm lasers. Images were acquired with 100× 1.45-NA Plan Apo objective using Micro-Manager software and ImageJ (National Institutes of Health). For Fig. 1 D-I Airyscan LSM 880 was used all other images were acquired on spinning disk detailed above. The line scanning confocal consists of Zeiss Axio Observer inverted fluorescence microscope body equipped with LSM 880, and Airyscan detector. Images were acquired with 63× 1.4-NA Plan Apo objective Zeiss Zen Software.

6.4.5 Statistics

All data described are from at least three biological replicates. All data were graphed as box and whisker plots with median (indicated by line) and mean (indicated by X) shown. When comparing two samples, two-tailed Student's t tests were used. For comparisons across multiple samples significance testing was done by first establishing significant differences exist between conditions by one way ANOVA. If variation between conditions was significantly greater then with in conditions this was followed by post hoc significance testing with Tukey's Test. ns = not significant, *$p < 0.05$, **$p < 0.01$, ***$p < 0.001$. Analyses were all performed using GraphPad Prism 8. Details of significance calculations as well as n values for each quantification are reported in the relevant figure legends

6.4.6 Endosome Fission Analysis

Endosome fission at FAM21 positive buds was quantified as in Hoyer et al. [2018]. Briefly, COS-7 cells were transfected with GFP-Rab7, mCh-FAM21, COR1A/1B/1C siRNA,

and rescued with either SiRES COR1C-Halo, SiRES COR1C ACT–Halo, SiRES COR1C ΔCC-Halo, SiRES COR1C ACT-ΔCC-Halo, or SiRES COR1C CC-Halo. Cells were imaged for 2 min at 2 sec intervals. All FAM21 positive endosome buds in resolvable regions of the cell were tracked for the duration of the time-lapse. Only endosomes with a clear distinction between vacuole and bud were measured. For each, the bud length, vacuole diameter, and whether or not fission occurred were recorded. To qualify as a fission event buds had to separate clearly from vacuole and be resolvable in the post-fission frame. The number of FAM21 positive fission events was divided by total number of FAM21 positive buds to give a per cell fission percentage.

6.4.7 CI-M6PR Sorting

Protocol was performed as previously described in Hoyer et al. [2018], Dong et al. [2016] . Briefly, COS-7 cells were prepared for imaging as detailed in the transfection/knock down protocols. Cells were incubated for one hour with anti CI-M6PR antibody 1:1000 in SF DMEM before being fixed with warm 4% Sucrose 4% PFA in 1x PBS. Cells were stained with anti-Giantin antibody 1/500 to mark the Golgi. To measure retrograde recycling a 5μm x 5μm ROI was placed over the anti-Giantin signal and CI-M6PR signal was measured yielding a "sorted Golgi" signal. All signal outside the Golgi ROI and within the cell was measured as "unsorted vesicular" signal. Background was measured outside of the cell via another 5μm x 5μm ROI and subtracted from the Golgi and vesicular signals. A ratio of background corrected vesicular to Golgi signal was then calculated to yield a final sorting score.

6.4.8 ER Contact Quantification

ER contact at FAM21 positive endosome buds was adapted from Hoyer et al. [2018]. Briefly, COS-7 cells were transfected with GFP-Rab7, mCh-FAM21, BFP-Sec61, COR1A/1B/1C siRNA, and rescued with either SiRES COR1C-Halo, SiRES COR1C ACT–Halo, SiRES

COR1C ΔCC-Halo, SiRES COR1C ACT-ΔCC-Halo, or SiRES COR1C CC-Halo. Time lapses were collected at 2 sec intervals for 2 min. I tracked every FAM21 positive endosome bud which was stable (did not collapse or undergo fission) for at least 30 consecutive frames in regions of the ER that were clearly resolvable. For each frame, overlap of the ER with the FAM21 positive endosome bud was assessed. This was used to calculate a percent time each bud was overlapping with ER. Bud percent contact was then averaged per cell to give an ER endosome bud contact score per cell.

6.5 Acknowledgements

I thank V. Olsen for assistance generating plasmids. I thank E. Sawyer, T. Nguyen, H. Wu, E. Zamponi, and V. Olsen for insight and helpful discussion. J.F. Striepen was supported by a graduate training grant in signaling and cellular regulation (NIH T32 GM008759). This work was also supported by a grant from the NIH to G.K. Voeltz. (GM120998). G.K. Voeltz. is an investigator of the Howard Hughes Medical Institute. I

Chapter 7

Summary and Discussion

7.1 Summary

Early studies indicated that branched actin assembly on buds is required for efficient cargo recycling from the endosome and proposed it was required for fission based on actin function during endocytosis Simonetti and Cullen [2019]. Puzzlingly, the presence of actin on an endosome bud was subsequently shown to increase bud stability in a manner seemingly opposed to fission Puthenveedu et al. [2010]. The new model proposed that actin mediated bud stabilization delayed the fission process in order for slow diffusing cargos to be sorted into the bud. Here I examined actin and fission directly and discovered that actin and its regulators organize the position of fission by defining membrane availability for ER MCS formation. I use time-lapse microscopy to show that Arp2/3 nucleated branched actin is restricted to the bud neck in a mechanism that depends on Type I coronins. When Type I coronins are depleted from the cell, the endosomal actin structures extend along the entire length of the bud, this prevents efficient ER-LE bud contact; thus, stalling endosome fission and preventing the efficient recycling of retrograde cargo. Strikingly, I find that the CC domain of COR1C alone is sufficient to rescue all measured phenotypes and functions of Type I coronins at the bud. By probing the functionality of the COR1C's CC, I discovered that the CC is required for ARP2/3 interaction. Further, I showed that by ectopically and acutely inhibiting the ARP2/3 complex I could reverse the effects of Type I coronin depletion on bud actin structure. Together, these data support a model whereby COR1C

CC binds and regulates the activity of ARP2/3 complex at the endosome bud and suggest that confinement of this actin-ARP2/3-COR1C structure to the bud neck is essential for bud fission.

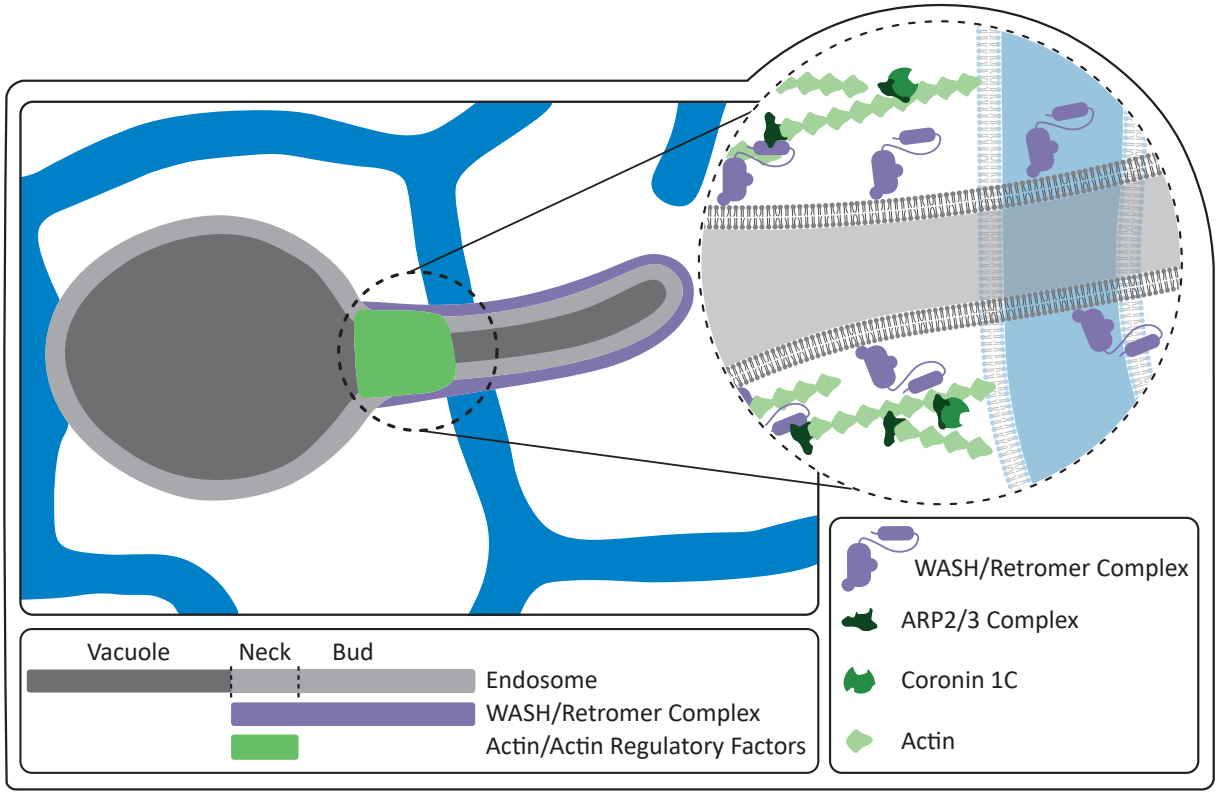

Figure 7.1: The WASH complex recruits and activates ARP2/3 to form a stabilizing actin structure on the endosome bud. COR1C is recruited to these actin structures to bind and counter act ARP2/3 actin nucleation via its CC. This results in an actin structure large enough to stabilize the bud allowing cargo to sort, but small enough to allow ER recruitment and bud fission.

7.2 Discussion

The unique enrichment of COR1C at the endosome bud and its capacity to rescue actin confinement and fission defects in a Type I coronin depletion suggests that COR1C has a specialized function in regulating endosomal actin. Although my data do indicate that COR1A and COR1B can prevent the more dramatic actin polymerization phenotypes, the lab previously showed that COR1C depletion alone is sufficient to reduce endosome fission rate by a mechanism that remained unexplored until now Hoyer et al. [2018]. This, combined with the diversity of mammalian coronins, points to the possibility that other specialized branched actin structures in the cell might also have a designated coronin regulator Chan et al. [2011].

Given that the actin structure is thought to stabilize the endosome bud, I were initially surprised that actin and its associated regulatory factors are not completely cleared from the endosome bud during fission. Rather, they are maintained in a stable but restricted location at the neck of the endosome bud. This suggests that the size of the actin structure is key to the slow receptor sorting process Puthenveedu et al. [2010]. The actin structure must be present to stabilize the bud and slow fission, but it must also be confined so that the buds remain fission competent. Actin, ARP3, and COR1C rarely leave with a departing bud remaining on the vacuolar half of the fission event. This is unlike the WASH complex (FAM21), which labels the entire bud and always marks the departing bud. If the membrane occupied by the actin structure were fission competent I would expect to see actin signal departing with the bud at a much higher rate. This partitioning suggests that the actin structure defines where fission can occur; specifically, at a distal position on the bud that is not occupied by actin.

The stability of the actin/ARP2/3/COR1C domain is also intriguing because it indicates that endosomes maintain a sorting domain that can perform multiple rounds of cargo sorting, bud formation, and fission. This domain's stability and partitioning paral-

lels observations made about components of ER exit sites (ERES), specifically, that COPII collars remain stably associated with the ER rather than leaving with the departing Golgi bound vesicle Westrate et al. [2020], Mccaughey et al. [2019], Carter et al. [2020]. This presents an interesting paradigm where trafficking domains are maintained stably on origin membranes and cargos are concentrated at these points rather than the reverse. It will be interesting to explore if multiple rounds of bud formation can occur from a single stable actin/ARP2/3/COR1C collar domain.

ER regulation of endosomal lipid composition is well established and is linked with a variety of downstream changes on the endosome Wilhelm et al. [2017], Alpy et al. [2013], Rocha et al. [2009], Eden et al. [2010], Dong et al. [2016]. Interestingly, lipid composition has been directly linked with regulation of actin polymerization on cellular membranes including endosomes Hong et al. [2015], Di Paolo and De Camilli [2006]. This is most directly illustrated by work showing that an ER-endosome MCS forms by interactions between Vesicle-Associated Membrane Protein-Associated Protein A and B (VAPA/B) and an endosomal cargo sorting component, sorting nexin 2 (SNX2). This MCS facilitates changes in phosphoinositide composition on the endosome membrane resulting in decreased WASH activity and thus less actin proliferation Dong et al. [2016]. This might fit well with my data showing the clear difference in WASH complex and ARP3 enrichment along the bud. Perhaps, the ER once recruited to a forming bud actively alters distal bud lipid composition to prevent WASH activation and F-actin nucleation there. These data also suggest intriguing feedback loops where ER contact both regulates and is regulated by endosomal actin.

7.3 Future Directions

My data indicate COR1C has an antagonistic regulatory interaction with ARP2/3 once the branched actin structure has been formed. As I discussed earlier, it is possible that other factors are also limiting ARP2/3 recruitment and activation. I show that WASH complex subunit FAM21 localizes along the entire length of the bud, but ARP3 is confined to the

bud neck. This contrast hints that some other factors limit where ARP2/3 can bind and be activated by WASH complex. This factor could work in concert with COR1C, limiting where branched structures can be initiated, while COR1C limits the extent of polymerization of already seeded actin structures. Such a protein would also be an excellent candidate as an endosome localized ER tether since my data strongly indicate that the ER is recruited to non actin coated membrane to drive the fission process.

Given that ER MCS with endosomes are demonstrated to regulate almost all fundamental characteristics and functions of endosomes it seems probable that endosome fusion could also be happening at MCS Wu et al. [2018], Wu and Voeltz [2021], Rocha et al. [2009], Raiborg et al. [2015a], Wilhelm et al. [2017], Allison et al. [2017], Dong et al. [2016]. It would be well worth exploring whether, as with mitochondria, the ER provides a platform for endosome fusion Abrisch et al. [2020]. Some preliminary work suggests that components of the HOPS tethering complex, which provide specificity and proximity for the function of SNARE proteins, co-localize well with the ER supporting the idea that ER is present at endosome fusion events 7.2. Additionally, I have designed some photo-convertible tools which allow us to be certain when two endosomes have fused by allowing us to see lipid mixing 7.3. Showing that endosome fusion relies on ER MCS would link perhaps the only primary endosomal function not yet connected to MCS to ER regulation. Additionally, disease mutations associated with proteins which drive endosomal fusion such as with hereditary spastic paraplegia and other neurological disorders make understanding all aspects of fusion controls is essential Toupenet Marchesi et al. [2021].

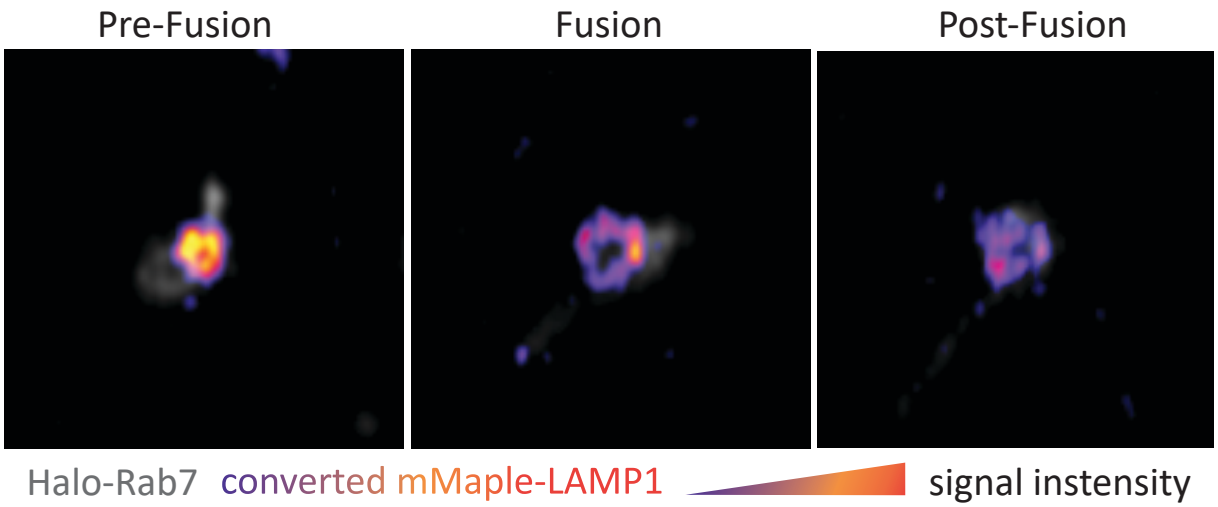

Figure 7.2: Example of late endosome fusion detected via photo-convertible tag. COS-7 cells were co-transfected with with Halo-Rab7 (LE, gray), and mMaple-LAMP1 (LE, FIRE lookup). Note that one endosome has no converted signal and that upon fusion the signal strength weakens as it is spread across more membrane.

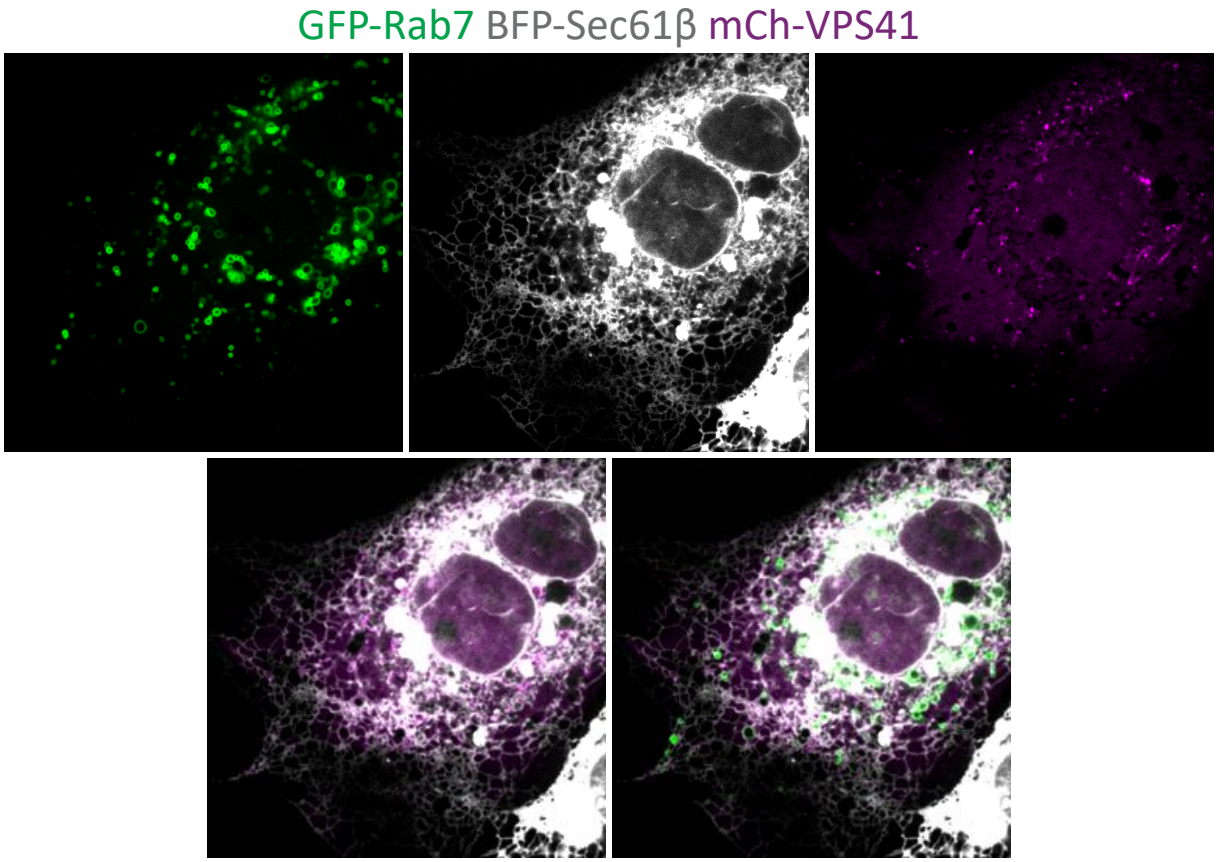

Figure 7.3: Representative example of HOPS complex subunit VPS41 overlap with ER. High degree of overlap suggests the ER might be recruited to points of potential fusion marked by LE tethering complex HOPS. COS-7 cells were co-transfected with with GFP-Rab7 (LE, green), mCh-VPS41 (HOPS complex, magenta), and BFP-Sec61 (ER, Gray)

Bibliography

Robert G. Abrisch, Samantha C. Gumbin, Brett Taylor Wisniewski, Laura L. Lackner, and Gia K. Voeltz. Fission and fusion machineries converge at ER contact sites to regulate mitochondrial morphology. Journal of Cell Biology, 219(4), 2020. ISSN 15408140. doi: 10.1083/JCB.201911122.

Rachel Allison, Jennifer H. Lumb, Coralie Fassier, James W. Connell, Daniel Ten Martin, Matthew N J Seaman, Jamilé Hazan, and Evan Reid. An ESCRT-spastin interaction promotes fission of recycling tubules from the endosome. Journal of Cell Biology, 202(3): 527–543, 2013. ISSN 00219525. doi: 10.1083/jcb.201211045.

Rachel Allison, James R Edgar, Guy Pearson, Tania Rizo, Timothy Newton, Sven Günther, Fiamma Berner, Jennifer Hague, James W Connell, Jürgen Winkler, et al. Defects in er–endosome contacts impact lysosome function in hereditary spastic paraplegia. Journal of Cell Biology, 216(5):1337–1355, 2017.

Fabien Alpy, Adrien Rousseau, Yannick Schwab, François Legueux, Isabelle Stoll, Corinne Wendling, Coralie Spiegelhalter, Pascal Kessler, Carole Mathelin, Marie-Christine Rio, Timothy P Levine, and Catherine Tomasetto. STARD3 or STARD3NL and VAP form a novel molecular tether between late endosomes and the ER. Journal of Cell Science, 126: 5500–5512, 2013. doi: 10.1242/jcs.139295. URL http://jcs.biologists.org/content/joces/126/23/5500.full.pdf.

Henning J.kleine Balderhaar and Christian Ungermann. CORVET and HOPS tethering complexes - coordinators of endosome and lysosome fusion. Journal of Cell Science, 126 (6):1307–1316, 2013. ISSN 00219533. doi: 10.1242/jcs.107805.

Sreetama Basu and Raphael Lamprecht. The role of actin cytoskeleton in dendritic spines in the maintenance of long-term memory. Frontiers in Molecular Neuroscience, 11(May): 1–9, 2018. ISSN 16625099. doi: 10.3389/fnmol.2018.00143.

Tess C Branon, Justin A Bosch, Ariana D Sanchez, Namrata D Udeshi, Tanya Svinkina, Steven A Carr, Jessica L Feldman, Norbert Perrimon, and Alice Y Ting. Directed evolution of TurboID for efficient proximity labeling in living cells and organisms. Doi.Org, page 196980, 2017. doi: 10.1101/196980. URL https://www.biorxiv.org/content/early/2017/10/02/196980?rss=1.

Liang Cai, Nicholas Holoweckyj, Michael D Schaller, James E Bear, North Carolina, Chapel Hill, Chapel Hill, and North Carolina. Phosphorylation of Coronin 1B by Protein Kinase C Regulates Interaction with Arp2 / 3 and Cell Motility *. Journal of Biological Chemistry, 280(36):31913–31923, 2005. ISSN 0021-9258. doi: 10.1074/jbc.M504146200. URL http://dx.doi.org/10.1074/jbc.M504146200.

Liang Cai, Thomas W Marshall, Andrea C Uetrecht, Dorothy A Schafer, and James E Bear. Coronin 1B Coordinates Arp2 / 3 Complex and Cofilin Activities at the Leading Edge. Cell, 1:915–929, 2007. doi: 10.1016/j.cell.2007.01.031.

Liang Cai, Alexander M Makhov, Dorothy A Schafer, and James E Bear. Coronin 1B Antagonizes Cortactin and Remodels Arp2 / 3-Containing Actin Branches in Lamellipodia. Cell, pages 828–842, 2008. doi: 10.1016/j.cell.2008.06.054.

Stephen D Carter, Cheri M Hampton, Robert Langlois, Roberto Melero, Zachary J Farino, Michael J Calderon, Wen Li, Callen T Wallace, Ngoc Han Tran, Robert A Grassucci, Stephanie E Siegmund, Joshua Pemberton, Travis J Morgenstern, Despoina Aslanoglou, Maïté Courel, Robin J Freyberg, Jonathan A Javitch, Sandra A Murray, Meir Aridor, Kenneth N Fish, Peter Walter, Tamas Balla, Deborah Fass, Sharon G Wolf, Simon C Watkins, José María Carazo, Grant J Jensen, Joachim Frank, and Zachary Freyberg. Ribosome-associated vesicles : A dynamic subcompartment of the endoplasmic reticulum in secretory cells. Science Advances, 2020.

Keefe T Chan, Sarah J Creed, and James E Bear. Unraveling the enigma : progress towards understanding the coronin family of actin regulators. Trends in Cell Biology, 21(8):481–488, 2011. ISSN 0962-8924. doi: 10.1016/j.tcb.2011.04.004. URL http://dx.doi.org/10.1016/j.tcb.2011.04.004.

Keefe T. Chan, David W. Roadcap, Nicholas Holoweckyj, and James E. Bear. Coronin 1C harbours a second actin-binding site that confers co-operative binding to F-actin. Biochemical Journal, 444(1):89–96, 2012. ISSN 0264-6021. doi: 10.1042/BJ20120209. URL http://biochemj.org/lookup/doi/10.1042/BJ20120209.

Jenna R. Christensen, Agnieszka A. Kendrick, Joey B. Truong, Adriana Aguilar-Maldonado, Vinit Adani, Monika Dzieciatkowska, and Samara L. Reck-Peterson. Cytoplasmic dynein-1 cargo diversity is mediated by the combinatorial assembly of FTS-Hook-FHIP complexes. eLife, 10:1–36, 2021. ISSN 2050084X. doi: 10.7554/eLife.74538.

Tom Cremer, Marlieke L.M. Jongsma, Fredrik Trulsson, Alfred C.O. Vertegaal, Jacques Neefjes, and Ilana Berlin. The ER-embedded UBE2J1/RNF26 ubiquitylation complex exerts spatiotemporal control over the endolysosomal pathway. Cell Reports, 34(3):108659, 2021. ISSN 22111247. doi: 10.1016/j.celrep.2020.108659. URL https://doi.org/10.1016/j.celrep.2020.108659.

Peter J. Cullen and Hendrik C. Korswagen. Sorting nexins provide diversity for retromer-dependent trafficking events. Nature Cell Biology, 14(1):29–37, 2012. ISSN 14657392. doi: 10.1038/ncb2374. URL http://dx.doi.org/10.1038/ncb2374.

Peter J Cullen and Florian Steinberg. To degrade or not to degrade: mechanisms and significance of endocytic recycling. Nature Reviews Molecular Cell Biology, 2018. ISSN 1471-0072. doi: 10.1038/s41580-018-0053-7. URL www.nature.com/nrm.

Emmanuel Derivery, Carla Sousa, Jérémie J. Gautier, Bérangère Lombard, Damarys Loew, and Alexis Gautreau. The Arp2/3 Activator WASH Controls the Fission of Endosomes through a Large Multiprotein Complex. Developmental Cell, 17(5):712–723, 2009. ISSN 15345807. doi: 10.1016/j.devcel.2009.09.010.

Gilbert Di Paolo and Pietro De Camilli. Phosphoinositides in cell regulation and membrane dynamics. Nature, 443(7112):651–657, 2006. ISSN 14764687. doi: 10.1038/nature05185.

Rui Dong, Yasunori Saheki, Sharan Swarup, Louise Lucast, J. Wade Harper, and Pietro De Camilli. Endosome-ER Contacts Control Actin Nucleation and Retromer Function through VAP-Dependent Regulation of PI4P. Cell, 166(2):408–423, 2016. ISSN 10974172. doi: 10.1016/j.cell.2016.06.037. URL http://dx.doi.org/10.1016/j.cell.2016.06.037.

Steve N. Duleh and Matthew D. Welch. WASH and the Arp2/3 complex regulate endosome shape and trafficking. Cytoskeleton, 67(3):193–206, 2010. ISSN 19493592. doi: 10.1002/cm.20437.

Emily R. Eden, Ian J. White, Anna Tsapara, and Clare E. Futter. Membrane contacts between endosomes and ER provide sites for PTP1B–epidermal growth factor receptor interaction. Nature Cell Biology, 12(3):267–272, 2010. ISSN 1465-7392. doi: 10.1038/ncb2026. URL http://www.nature.com/doifinder/10.1038/ncb2026.

Emily R. Eden, Elena Sanchez-Heras, Anna Tsapara, Andrzej Sobota, Tim P. Levine, and Clare E. Futter. Annexin A1 Tethers Membrane Contact Sites that Mediate ER to Endosome Cholesterol Transport. Developmental Cell, 37(5):473–483, 2016. ISSN 18781551. doi: 10.1016/j.devcel.2016.05.005. URL http://dx.doi.org/10.1016/j.devcel.2016.05.005.

Artem I. Fokin, Violaine David, Ksenia Oguievetskaia, Emmanuel Derivery, Caroline E. Stone, Luyan Cao, Nathalie Rocques, Nicolas Molinie, Véronique Henriot, Magali Aumont-Nicaise, Maria Victoria Hinckelmann, Frédéric Saudou, Christophe Le Clainche, Andrew P. Carter, Guillaume Romet-Lemonne, and Alexis M. Gautreau. The Arp1/11 minifilament of dynactin primes the endosomal Arp2/3 complex. Science Advances, 7(3):1–12, 2021. ISSN 23752548. doi: 10.1126/sciadv.abd5956.

J. R. Friedman, J. R. DiBenedetto, M. West, A. A. Rowland, and G. K. Voeltz. Endoplasmic reticulum-endosome contact increases as endosomes traffic and mature. Molecular Biology of the Cell, 24(7):1030–1040, 2013. ISSN 1059-1524. doi: 10.1091/mbc.E12-10-0733. URL http://www.molbiolcell.org/cgi/doi/10.1091/mbc.E12-10-0733.

Matthew Gallon and Peter J. Cullen. Retromer and sorting nexins in endosomal sorting. Biochemical Society Transactions, 43(1):33–47, 2015. ISSN 0300-5127.

doi: 10.1042/BST20140290. URL http://biochemsoctrans.org/lookup/doi/10.1042/BST20140290.

Yuan Gao, Juan Xiong, Qing Zhu Chu, and Wei Ke Ji. PDZD8-mediated lipid transfer at contacts between the ER and late endosomes/lysosomes is required for neurite outgrowth. Journal of Cell Science, 135(5), 2021. ISSN 14779137. doi: 10.1242/jcs.255026.

Francesca Giordano, Yasunori Saheki, Olof Idevall-hagren, Sara Francesca Colombo, Michelle Pirruccello, Ira Milosevic, Elena O Gracheva, Sviatoslav N Bagriantsev, and Nica Borgese. ER-PM Interactions Mediated by the Extended Synaptotagmins. CELL, 153(7):1494–1509, 2013. ISSN 0092-8674. doi: 10.1016/j.cell.2013.05.026. URL http://dx.doi.org/10.1016/j.cell.2013.05.026.

Timothy S Gomez and Daniel D Billadeau. A FAM21-Containing WASH Complex Regulates Retromer-Dependent Sorting. Developmental Cell, 17(5):699–711, 2009. ISSN 1534-5807. doi: 10.1016/j.devcel.2009.09.009. URL http://dx.doi.org/10.1016/j.devcel.2009.09.009.

Xiaoli Guo, Ginny G. Farías, Rafael Mattera, and Juan S. Bonifacino. Rab5 and its effector FHF contribute to neuronal polarity through dynein-dependent retrieval of somatodendritic proteins from the axon. Proceedings of the National Academy of Sciences of the United States of America, 113(36):E5318–E5327, 2016. ISSN 10916490. doi: 10.1073/pnas.1601844113.

Chadwick M. Hales, Jean Pierre Vaerman, and James R. Goldenring. Rab11 family interacting protein 2 associates with myosin Vb and regulates plasma membrane recycling. Journal of Biological Chemistry, 277(52):50415–50421, 2002. ISSN 00219258. doi: 10.1074/jbc.M209270200. URL http://dx.doi.org/10.1074/jbc.M209270200.

Mingming Hao and Frederick R. Maxfield. Characterization of rapid membrane internalization and recycling. Journal of Biological Chemistry, 275(20):15279–15286, 2000. ISSN 00219258. doi: 10.1074/jbc.275.20.15279. URL http://dx.doi.org/10.1074/jbc.275.20.15279.

Michael E Harbour, Sophia Y Breusegem, and Matthew N J Seaman. Recruitment of the endosomal WASH complex is mediated by the extended 'tail' of Fam21 binding to the retromer protein Vps35. Biochem. J, 442:209–220, 2012. doi: 10.1042/BJ20111761. URL http://www.biochemj.org/content/ppbiochemj/442/1/209.full.pdf.

Byron Hetrick, Min Suk Han, Luke A Helgeson, and Brad J Nolen. Small Molecules CK-666 and CK-869 Inhibit by Blocking an Activating Conformational Change. Chemistry Biology, 20(5):701–712, 2013. ISSN 1074-5521. doi: 10.1016/j.chembiol.2013.03.019. URL http://dx.doi.org/10.1016/j.chembiol.2013.03.019.

Nan Hyung Hong, Aidong Qi, and Alissa M. Weaver. PI(3,5)P2 controls endosomal branched actin dynamics by regulating cortactin-Actin interactions. Journal of Cell Biology, 210 (5):753–769, 2015. ISSN 15408140. doi: 10.1083/jcb.201412127.

Melissa J. Hoyer, Patrick J. Chitwood, Christopher C. Ebmeier, Jonathan F. Striepen, Robert Z. Qi, William M. Old, and Gia K. Voeltz. A Novel Class of ER Membrane Proteins Regulates ER-Associated Endosome Fission. Cell, 175(1):254–265.e14, 2018. ISSN 10974172. doi: 10.1016/j.cell.2018.08.030. URL https://doi.org/10.1016/j.cell.2018.08.030.

Christine L Humphries, Heath I Balcer, Jessica L D Agostino, Barbara Winsor, David G Drubin, Georjana Barnes, Brenda J Andrews, and Bruce L Goode. Direct regulation of Arp2 / 3 complex activity and function by the actin binding protein coronin. Journal of Cell Biology, 159(6):993–1004, 2002. doi: 10.1083/jcb.200206113.

Edward L Huttlin, Raphael J Bruckner, Jose Navarrete-perea, Laura Pontano Vaites, J Wade Harper, Steven P Gygi, Edward L Huttlin, Raphael J Bruckner, Jose Navarrete-perea, Joe R Cannon, Kurt Baltier, and Fana Gebreab. Dual proteome-scale networks reveal cell-specific remodeling of the human interactome ll Resource Dual proteome-scale networks reveal cell-specific remodeling of the human interactome. Cell, 184(11):3022–3040.e28, 2021. ISSN 0092-8674. doi: 10.1016/j.cell.2021.04.011. URL https://doi.org/10.1016/j.cell.2021.04.011.

Marie Johansson, Nuno Rocha, Wilbert Zwart, Ingrid Jordens, Lennert Janssen, Coenraad Kuijl, Vesa M. Olkkonen, and Jacques Neefjes. Activation of endosomal dynein motors by stepwise assembly of Rab7-RILP-p150Glued, ORP1L, and the receptor βIII spectrin. Journal of Cell Biology, 176(4):459–471, 2007. ISSN 00219525. doi: 10.1083/jcb.200606077.

Marlieke L L.M. Jongsma, Ilana Berlin, Ruud H H.M. Wijdeven, Lennert Janssen, George M M.C. Janssen, Malgorzata A A. Garstka, Hans Janssen, Mark Mensink, Peter A A. van Veelen, Robbert M M. Spaapen, and Jacques Neefjes. An ER-Associated Pathway Defines Endosomal Architecture for Controlled Cargo Transport. Cell, 166(1):152–166, 2016. ISSN 10974172. doi: 10.1016/j.cell.2016.05.078. URL http://dx.doi.org/10.1016/j.cell.2016.05.078.

Arunas Kvainickas, Ana Jimenez-Orgaz, Heike Nägele, Zehan Hu, Jörn Dengjel, and Florian Steinberg. Cargo-selective SNX-BAR proteins mediate retromer trimer independent retrograde transport. Journal of Cell Biology, 216(11):3677–3693, 2017a. ISSN 15408140. doi: 10.1083/jcb.201702137.

Arunas Kvainickas, Ana Jimenez Orgaz, Heike Nägele, Britta Diedrich, Kate J. Heesom, Jörn Dengjel, Peter J. Cullen, and Florian Steinberg. Retromer- and WASH-dependent sorting of nutrient transporters requires a multivalent interaction network with ANKRD50. Journal of Cell Science, 130(2):382–395, 2017b. ISSN 0021-9533. doi: 10.1242/jcs.196758. URL http://jcs.biologists.org/lookup/doi/10.1242/jcs.196758.

Lars Langemeyer, Florian Fröhlich, and Christian Ungermann. Rab GTPase Function in Endosome and Lysosome Biogenesis. Trends in Cell Biology, 28(11):957–970, 2018. ISSN 18793088. doi: 10.1016/j.tcb.2018.06.007. URL https://doi.org/10.1016/j.tcb.2018.06.007.

L. A. Lapierre, R. Kumar, C. M. Hales, J. Navarre, S. G. Bhartur, J. O. Burnette, Jr Provance, J. A. Mercer, M. Bähler, and J. R. Goldenring. Myosin Vb is associated with plasma membrane recycling systems. Molecular Biology of the Cell, 12(6):1843–1857, 2001. ISSN 10591524. doi: 10.1091/mbc.12.6.1843.

Joshua A. Lees, Mirko Messa, Elizabeth Wen Sun, Heather Wheeler, Federico Torta, Markus R. Wenk, Pietro De Camilli, and Karin M. Reinisch. Lipid transport by TMEM24 at ER-plasma membrane contacts regulates pulsatile insulin secretion. Science, 355(6326), 2017. ISSN 10959203. doi: 10.1126/science.aah6171.

Xiang Dong Li, Katsuhide Mabuchi, Reiko Ikebe, and Mitsuo Ikebe. Ca2+-induced activation of ATPase activity of myosin Va is accompanied with a large conformational change. Biochemical and Biophysical Research Communications, 315(3):538–545, 2004. ISSN 0006291X. doi: 10.1016/j.bbrc.2004.01.084.

Xiaosi Lin, Ting Yang, Shicong Wang, Zhen Wang, Ye Yun, Lixiang Sun, Yunhe Zhou, Xiaohui Xu, Chihiro Akazawa, Wanjin Hong, and Tuanlao Wang. RILP interacts with HOPS complex via VPS41 subunit to regulate endocytic trafficking. Scientific Reports, 4: 1–12, 2014. ISSN 20452322. doi: 10.1038/srep07282.

Satyajit Mayor and Darius V Köster. Cortical actin and the plasma membrane : inextricably intertwined. Current Opinion in Cell Biology, 2016. doi: 10.1016/j.ceb.2016.02.021.

Janine Mccaughey, Nicola L Stevenson, Stephen Cross, and David J Stephens. ER-to-Golgi trafficking of procollagen in the absence of large carriers. Journal of Cell Biology, 218(3): 929–948, 2019.

Ann L. McEvoy, Hiofan Hoi, Mark Bates, Evgenia Platonova, Paula J. Cranfill, Michelle A. Baird, Michael W. Davidson, Helge Ewers, Jan Liphardt, and Robert E. Campbell. mMaple: A Photoconvertible Fluorescent Protein for Use in Multiple Imaging Modalities. PLoS ONE, 7(12), 2012. ISSN 19326203. doi: 10.1371/journal.pone.0051314.

Kerrie E. McNally, Rebecca Faulkner, Florian Steinberg, Matthew Gallon, Rajesh Ghai, David Pim, Paul Langton, Neil Pearson, Chris M. Danson, Heike Nägele, Lindsey L. Morris, Amika Singla, Brittany L. Overlee, Kate J. Heesom, Richard Sessions, Lawrence Banks, Brett M. Collins, Imre Berger, Daniel D. Billadeau, Ezra Burstein, and Peter J. Cullen. Retriever is a multiprotein complex for retromer-independent endosomal cargo recycling. Nature Cell Biology, 19(10), 2017. ISSN 1465-7392. doi: 10.1038/ncb3610. URL http://www.nature.com/doifinder/10.1038/ncb3610.

Jacques Neefjes, Marlieke M.L. Jongsma, and Ilana Berlin. Stop or Go? Endosome Positioning in the Establishment of Compartment Architecture, Dynamics, and Function. Trends in Cell Biology, 27(8):580–594, 2017. ISSN 18793088. doi: 10.1016/j.tcb.2017.03.002. URL http://dx.doi.org/10.1016/j.tcb.2017.03.002.

Lelio Orci, Mariella Ravazzola, Marion Le Coadic, Wei Wei Shen, Nicolas Demaurex, and Pierre Cosson. STIM1-induced precortical and cortical subdomains of the endoplasmic

reticulum. Proceedings of the National Academy of Sciences of the United States of America, 106(46):19358–19362, 2009. ISSN 00278424. doi: 10.1073/pnas.0911280106.

Nina Marie Pedersen, Eva Maria Wenzel, Ling Wang, Sandra Antoine, Philippe Chavrier, Harald Stenmark, and Camilla Raiborg. Protrudin-mediated ER – endosome contact sites promote MT1-MMP exocytosis and cell invasion. Journal of Cell Biology, 219(8), 2020.

Manojkumar A Puthenveedu, Benjamin Lauffer, Paul Temkin, Rachel Vistein, Peter Carlton, Kurt Thorn, Jack Taunton, Orion D Weiner, Robert G Parton, and Mark von Zastrow. Sequence-dependent sorting of recycling proteins by actin-stabilized endosomal microdomains. Cell, 143(5):761–73, nov 2010. ISSN 1097-4172. doi: 10.1016/j.cell.2010.10.003.

C. Raiborg, E. M. Wenzel, and H. Stenmark. ER-endosome contact sites: molecular compositions and functions. The EMBO Journal, 34(14):1848–1858, 2015a. ISSN 0261-4189. doi: 10.15252/embj.201591481. URL http://emboj.embopress.org/cgi/doi/10.15252/embj.201591481.

Camilla Raiborg, Eva M. Wenzel, Nina M. Pedersen, Hallvard Olsvik, Kay O. Schink, Sebastian W. Schultz, Marina Vietri, Veronica Nisi, Cecilia Bucci, Andreas Brech, Terje Johansen, and Harald Stenmark. Repeated ER–endosome contacts promote endosome translocation and neurite outgrowth. Nature, 520(7546):234–238, 2015b. ISSN 0028-0836. doi: 10.1038/nature14359. URL http://www.nature.com/doifinder/10.1038/nature14359.

Markus A. Riederer, Thierry Soldati, Allan D. Shapiro, Joseph Lin, and Suzanne R. Pfeffer. Lysosome biogenesis requires rab9 function and receptor recycling from endosomes to the trans-Golgi network. Journal of Cell Biology, 125(3):573–582, 1994. ISSN 00219525. doi: 10.1083/jcb.125.3.573.

Nuno Rocha, Coenraad Kuijl, Rik Van Der Kant, Lennert Janssen, Diane Houben, Hans Janssen, Wilbert Zwart, and Jacques Neefjes. Cholesterol sensor ORP1L contacts the ER protein VAP to control Rab7-RILP-p150Glued and late endosome positioning. Journal of Cell Biology, 185(7):1209–1225, 2009. ISSN 00219525. doi: 10.1083/jcb.200811005.

André Rosentreter, Andreas Hofmann, Charles-peter Xavier, Maria Stumpf, Angelika A Noegel, and Christoph S Clemen. Coronin 3 involvement in F-actin-dependent processes at the cell cortex. Experimental Cell Research, 13, 2006. doi: 10.1016/j.yexcr.2006.12.015.

Klemens Rottner, Jan Ha, and Kenneth G Campellone. WASH , WHAMM and JMY : regulation of Arp2 / 3 complex and beyond. Trends in Cell Biology, 20(11), 2010. doi: 10.1016/j.tcb.2010.08.014.

Ashley A. Rowland, Patrick J. Chitwood, Melissa J. Phillips, and Gia K. Voeltz. ER contact sites define the position and timing of endosome fission. Cell, 159(5):1027–1041, 2014. ISSN 10974172. doi: 10.1016/j.cell.2014.10.023. URL http://dx.doi.org/10.1016/j.cell.2014.10.023.

Ignacio V. Sandoval and Oddmund Bakke. Targeting of membrane proteins to endosomes and lysosomes. Trends in Cell Biology, 4(8):292–297, 1994. ISSN 09628924. doi: 10.1016/0962-8924(94)90220-8.

Trina A. Schroer. Dynactin. Annual Review of Cell and Developmental Biology, 20:759–779, 2004. ISSN 10810706. doi: 10.1146/annurev.cellbio.20.012103.094623.

Matthew N.J. Seaman, J. Michael McCaffery, and Scott D. Emr. A membrane coat complex essential for endosome-to-Golgi retrograde transport in yeast. Journal of Cell Biology, 142 (3):665–681, 1998. ISSN 00219525. doi: 10.1083/jcb.142.3.665.

Michiko Shirane and Keiichi I. Nakayama. Protrudin induces neurite formation by directional membrane trafficking. Science, 314(5800):818–821, 2006. ISSN 00368075. doi: 10.1126/science.1134027.

Boris Simonetti and Peter J Cullen. Actin-dependent endosomal receptor recycling. Current Opinion in Cell Biology, 56:22–33, 2019. ISSN 0955-0674. doi: 10.1016/j.ceb.2018.08.006. URL https://doi.org/10.1016/j.ceb.2018.08.006.

Boris Simonetti, Chris M Danson, Kate J Heesom, and Peter J Cullen. Sequence-dependent cargo recognition by SNX-BARs mediates retromer-independent transport of CI-MPR. The Journal of cell biology, page jcb.201703015, 2017. ISSN 1540-8140. doi: 10.1083/jcb.201703015. URL http://www.ncbi.nlm.nih.gov/pubmed/28935633.

Virupakshi Soppina, Arpan Kumar Rai, Avin Jayesh Ramaiya, Pradeep Barak, and Roop Mallik. Tug-of-war between dissimilar teams of microtubule motors regulates transport and fission of endosomes. Proceedings of the National Academy of Sciences of the United States of America, 106(46):19381–19386, 2009. ISSN 00278424. doi: 10.1073/pnas.0906524106.

Ziqiang Spoerl, Maria Stumpf, Angelika A Noegel, Andreas Hasse, and D Ko. Oligomerization , F-actin Interaction , and Membrane Association of the Ubiquitous Mammalian Coronin 3 Are Mediated by Its Carboxyl Terminus *. Journal of Biological Chemistry, 277(50):48858–48867, 2002. ISSN 0021-9258. doi: 10.1074/jbc.M205136200. URL http://dx.doi.org/10.1074/jbc.M205136200.

Liriopé Toupenet Marchesi, Marion Leblanc, and Giovanni Stevanin. Current knowledge of endolysosomal and autophagy defects in hereditary spastic paraplegia. Cells, 10(7):1678, 2021.

Jan van der Beek, Caspar Jonker, Reini van der Welle, Nalan Liv, and Judith Klumperman. CORVET, CHEVI and HOPS – Multisubunit tethers of the endo-lysosomal system in health and disease. Journal of Cell Science, 132(10), 2019. ISSN 14779137. doi: 10.1242/jcs.189134.

Rik Van Der Kant, Caspar T.H. Jonker, Ruud H. Wijdeven, Jeroen Bakker, Lennert Janssen, Judith Klumperman, and Jacques Neefjes. Characterization of the mammalian CORVET and HOPS complexes and their modular restructuring for endosome specificity. Journal

of Biological Chemistry, 290(51):30280–30290, 2015. ISSN 1083351X. doi: 10.1074/jbc.M115.688440. URL http://dx.doi.org/10.1074/jbc.M115.688440.

Zhiping Wang, Jeffrey G. Edwards, Nathan Riley, D. William Provance, Ryan Karcher, Xiang dong Li, Ian G. Davison, Mitsuo Ikebe, John A. Mercer, Julie A. Kauer, and Michael D. Ehlers. Myosin Vb Mobilizes Recycling Endosomes and AMPA Receptors for Postsynaptic Plasticity. Cell, 135(3):535–548, 2008. ISSN 00928674. doi: 10.1016/j.cell.2008.09.057.

Thomas Wassmer, Naomi Attar, Martin Harterink, Jan R.T. van Weering, Colin J. Traer, Jacqueline Oakley, Bruno Goud, David J. Stephens, Paul Verkade, Hendrik C. Korswagen, and Peter J. Cullen. The Retromer Coat Complex Coordinates Endosomal Sorting and Dynein-Mediated Transport, with Carrier Recognition by the trans-Golgi Network. Developmental Cell, 17(1):110–122, 2009. ISSN 15345807. doi: 10.1016/j.devcel.2009.04.016. URL http://dx.doi.org/10.1016/j.devcel.2009.04.016.

Laura M Westrate, Melissa J Hoyer, Michael J Nash, and Gia K Voeltz. Vesicular and uncoated Rab1-dependent cargo carriers facilitate ER to Golgi transport. Journal of Cell Science, 2020. doi: 10.1242/jcs.239814.

Léa P Wilhelm, Corinne Wendling, Benoît Védie, Toshihide Kobayashi, Marie-pierre Chenard, Catherine Tomasetto, Guillaume Drin, and Fabien Alpy. STARD 3 mediates endoplasmic reticulum-to- endosome cholesterol transport at membrane contact sites. The EMBO Journal, 36(10), 2017. doi: 10.15252/embj.201695917.

Haoxi Wu and Gia K Voeltz. Reticulon-3 Promotes Endosome Maturation at ER Membrane Contact Sites. Developmental Cell, 56(1):52–66.e7, 2021. ISSN 1534-5807. doi: 10.1016/j.devcel.2020.12.014. URL https://doi.org/10.1016/j.devcel.2020.12.014.

Haoxi Wu, Pedro Carvalho, and Gia K Voeltz. Here, there, and everywhere: The importance of ER membrane contact sites. Review Summary Cell Biology, 466(August), 2018. ISSN 0036-8075. doi: 10.1126/science.aan5835. URL http://science.sciencemag.org/.

Allison L. Zajac, Yale E. Goldman, Erika L.F. Holzbaur, and E. Michael Ostap. Local cytoskeletal and organelle interactions impact molecular-motor-driven early endosomal trafficking. Current Biology, 23(13):1173–1180, 2013. ISSN 09609822. doi: 10.1016/j.cub.2013.05.015. URL http://dx.doi.org/10.1016/j.cub.2013.05.015.